Chem Soc Rev

REVIEW ARTICLE

View Article Online
View Journal | View Issue

Cite this: *Chem. Soc. Rev.*, 2021, **50**, 3842

Printed aerogels: chemistry, processing, and applications

Junzong Feng,[ab] Bao-Lian Su,[cd] Hesheng Xia,[e] Shanyu Zhao,[f] Chao Gao,[g] Lukai Wang,[b] Osarenkhoe Ogbeide,[a] Jian Feng[b] and Tawfique Hasan*[a]

As an extraordinarily lightweight and porous functional nanomaterial family, aerogels have attracted considerable interest in academia and industry in recent decades. Despite the application scopes, the modest mechanical durability of aerogels makes their processing and operation challenging, in particular, for situations demanding intricate physical structures. "Bottom-up" additive manufacturing technology has the potential to address this drawback. Indeed, since the first report of 3D printed aerogels in 2015, a new interdisciplinary research area combining aerogel and printing technology has emerged to push the boundaries of structure and performance, further broadening their application scope. This review summarizes the state-of-the-art of printed aerogels and presents a comprehensive view of their developments in the past 5 years, and highlights the key near- and mid-term challenges.

Received 28th September 2020

DOI: 10.1039/c9cs00757a

rsc.li/chem-soc-rev

[a] *Cambridge Graphene Centre, University of Cambridge, Cambridge CB3 0FA, UK. E-mail: th270@cam.ac.uk*
[b] *Science and Technology on Advanced Ceramic Fibers and Composites Laboratory, National University of Defense Technology, Changsha 410073, Hunan, P. R. China*
[c] *State Key Laboratory of Advanced Technology for Materials Synthesis and Processing & School of materials science and engineering, Wuhan University of Technology, Loushi Road 122, Wuhan 430070, P. R. China*
[d] *Laboratory of Inorganic Materials Chemistry, Department of Chemistry, University of Namur, 61 rue de Bruxelles, B-5000 Namur, Belgium*
[e] *State Key Laboratory of Polymer Materials Engineering, Polymer Research Institute of Sichuan University, Chengdu 610065, P. R. China*
[f] *Laboratory for Building Energy Materials and Components, Swiss Federal Laboratories for Materials Science and Technology, Empa, CH-8600, Dübendorf, Switzerland*
[g] *MOE Key Laboratory of Macromolecular Synthesis and Functionalization, Department of Polymer Science and Engineering, Zhejiang University, 38 Zheda Road, 310027, Hangzhou, P. R. China*

Junzong Feng

Dr Junzong Feng is an associate professor in the College of Aerospace Science and Engineering in the National University of Defense Technology (NUDT), China. He obtained his PhD in Materials Science and Engineering from NUDT in 2012, then joined the Aerogel Research group led by Professor Jian Feng. He spent a year (2020) as a visiting scholar at the University of Cambridge to work on printed aerogels. Dr Feng's research interests include the design, preparation, and characterization of nanoporous aerogels, specifically carbon, oxide, and organic aerogels, and their applications as superthermal insulators and catalyst supports.

Bao-Lian Su

Prof Bao-Lian Su is a member of the European Academy of Sciences and a member of the Royal Academy of Belgium and a Clare Hall life member, University of Cambridge. He holds a "Chaire Francqui au titre Belge". He is a full professor and the Director of the Laboratory of Inorganic Materials Chemistry (CMI), University of Namur, Belgium. Prof Su is also a "Strategical Scientist" at the Wuhan University of Technology. His current research fields include synthesis, property study and molecular engineering of organized, bio-inspired hierarchically porous materials and living materials, and the encapsulation of living organisms for catalysis, artificial photosynthesis, nanotechnology, biotechnology, cell therapy and biomedical applications.

1. Introduction

Aerogels typify low-density bulk materials with nanostructured solid skeletons and open pores. Their skeletal and pore structure can be regulated at the nanoscale to achieve a number of extraordinary physical properties, including ultra-low density and thermal conductivity, ultra-high specific surface area and ultra-strong adsorption capacity. These properties make aerogels an ideal material family for a wide range of potential applications, including energy storage,[1] catalyst supports,[2] sensors,[3] chemical adsorption,[4] thermal insulation,[5] biomedical,[6] and shock absorption,[7] thereby promoting the development of industries such as environmental protection,[4] construction,[8] chemical,[9] aerospace,[10] transportation,[1] artificial intelligence,[11] and medicine.[6] Because of the controllability of the nanostructures, excellent physical properties, and potential application scopes, aerogels have attracted increasing interest from both the academic and industrial communities in the past two decades.

Additive manufacturing, based on a variety of printing technologies, is considered as one of the pillars of the third industrial revolution.[12,13] It is a "bottom-up" manufacturing process, as opposed to the traditional "top-down" subtractive strategy.[14] Based on the artificial intelligence-aided design of patterns or three-dimensional (3D) models, it uses software and numerical control systems to stack metals, polymers, inorganics, and even medical-grade biomaterials, layer by layer, to create solid objects through a variety of technologies including inkjet, extrusion, sintering, melting, photonic curing, and spraying.[15] It

Hesheng Xia

Prof Hesheng Xia received his PhD degree from Sichuan University, China in 2001. In 2003–2005, he worked as a research associate at Loughborough University, UK. He became a full professor at Sichuan University in 2005. He is an international representative of Polymer Processing Society (PPS), and also an affiliated professor at the Institute for Polymers, Composites and Biomaterials (IPCB-CNR), Italy. His main research interests include polymer micro/nano-composites, polymer materials for 3D printing, dynamic polymer and mechanochemistry. To date, he has published over 210 peer-reviewed publications, 103 patents, and 3 book chapters.

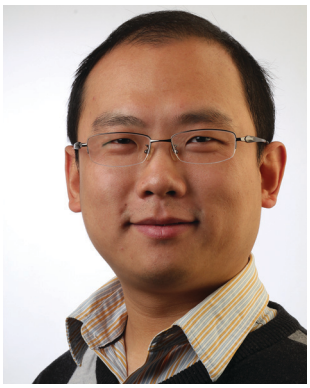

Shanyu Zhao

Dr Shanyu Zhao is a senior scientist at the Building Energy Materials and Components Laboratory at the Swiss Federal Laboratory for Materials Science and Technology (Empa). He received his PhD in materials science from Dalian University of Technology (2011) and spent a year as a visiting researcher in the Chemistry Department at Brown University (2009). He has worked on scientific research and product development with a strong focus on technical project management in the areas of functional porous and energy materials. His research interests range from sol–gel chemistry and additive manufacturing to biopolymers, aerogels, and nanocomposites.

Jian Feng

Prof Jian Feng received his PhD from Northwestern Polytechnical University, China in 1998. He then joined the National University of Defense Technology and founded the Aerogel Research group. He is one of the executive members of the Chinese Society for Composite Materials and the Sol–Gel Committee of the Chinese Ceramic Society. He spent a year as a senior visiting scholar (2012) in the University of British Columbia, Canada. Prof Feng's group works on a variety of research topics on nanoporous aerogels, including developing new kinds of aerogels and designing their nanostructures for enhanced thermal stability, controlled thermal transfer, mechanical reinforcement, and shaping, as well as their industrialized production.

Tawfique Hasan

Dr Tawfique Hasan received his PhD from Cambridge University in 2009. He is now a Reader in Nanomaterials Engineering at the Cambridge Graphene Centre, Cambridge University Engineering Department and leads the NanoEngineering research group. Together with his graduate students and colleagues, Dr Hasan initiated the field of 2D crystal printable inks and ultrafast lasers, and pioneered the integration of inkjet printed 2D materials with silicon platform for (opto)electronics and gas sensors. One of his recent interests is in hardware–software fusion, both for large-scale manufacturable 2D crystal-based printed devices for sensing and 1D nanostructures for ultraminiaturized optoelectronics.

is not limited by mould manufacturing or processing technology, which simplifies process cycles and reduces material consumption. The technology also allows high manufacturing accuracy to create complex and fine patterns or structures. These greatly streamline the concept-to-design-to-manufacturing process, shortening the production cycle. As a powerful complement to traditional subtractive manufacturing methods, additive manufacturing therefore offers new possibilities in solving traditional manufacturing challenges.[16,17]

The first research combining printing technology and aerogel to obtain 3D printed aerogel scaffolds was reported in 2015.[18] Since then, the field of printed aerogels has flourished and now represents an interdisciplinary research area intersecting aerogel and additive manufacturing technologies. There are two simple reasons behind this rapid development. First, the aerogel preparation method is always a liquid-to-solid sol–gel process. It can be easily adapted to ink formulation suitable for printing technologies based on liquid jetting or slurry extrusion. Second, application-specific shaping of aerogels is highly challenging as their low density and strength curb traditional post-machining options. The ''bottom-up'' printing technology family readily offers an alternative solution to create intricate shapes without complicated post-processing. In addition, current generation formulation and printing technologies can be tailored to design and manufacture macroporous structures. Indeed, printed aerogel scaffolds with designed macropores have been demonstrated to achieve better mass transfer performance than non-printed aerogels,[19–21] which is critical to applications such as energy storage and tissue engineering.[19–23]

Based on the current landscape of aerogels using additive manufacturing technologies, the goal of this review is to provide a comprehensive overview of this rapidly growing research area, discussing the state-of-the-art science, technology and applications. In this review, we first briefly introduce aerogels and functional printing technology to the readers. Next, in line with the current understanding and standard practices in the field, we discuss the ink formulation and pertinent aerogel chemistry, printing considerations and processes, and various drying and post-treatment strategies. We then focus on the aerogel properties and their relevance to a wide range of application scopes. Finally, we provide a summary of research perspectives, critical hurdles and research opportunities. We hope that this review will help researchers in academia and industry to comprehensively understand the recent technical advancements and challenges in the field, and inspire new ideas and research directions.

2. Aerogels

The word 'aerogel' originates from 'gel', a 3D solid network with liquid filled pores, prepared by a sol–gel method. When the liquid in the pores of the gel is replaced by gas or air, the resulting light-weight nano-framework structure is called an aerogel.[24] 'Aerogel' represents a broad description of the structure, and does not include restrictions on material compositions and preparation processes. The International Union of Pure and Applied Chemistry (IUPAC) defines a gel as a ''non-fluid colloidal network or polymer network that is expanded throughout its whole volume by a fluid'' and an aerogel as a ''gel comprised of a microporous solid in which the dispersed phase is a gas. Microporous silica, microporous glass, and zeolites are common examples of aerogels''.[25] But this definition is really too broad and may sometimes cause confusion because it is inappropriately defined as microporous (<2 nm), and without specific numerical restrictions to the porosity (the volume fraction of voids over a total volume). In their Review, Pierre A. C. *et al.* suggested that aerogels are dried gels with a very high relative pore volume ($>90\%$).[26] Ziegler C. *et al.* suggested that an aerogel is a solid with meso- (2–50 nm) and macropores (>50 nm) with diameters up to a few hundred nanometres and a porosity of more than 95% in which the dispersed phase is a gas.[27] At present, the industrial community generally considers aerogels as ''an open-celled, mesoporous, solid foam that is composed of a network of interconnected nanostructures and exhibits a porosity of no less than 50%''.[28] However, with the rapid development of porous structures based on nanomaterials, there is also a recent trend of describing low-density bulk materials composed of uniformly dispersed one-dimensional (1D) nanofibres or two-dimensional (2D) nanosheets (such as graphene nanosheets or metal nanowires) as aerogels.[29] These 1D and 2D material aerogels display highly porous networks with pore sizes in the range of a few hundred nanometres to a few micrometres, which is much larger than mesoporous structures. It can be seen that the above definitions focus on pore sizes (micro-, meso-, macro-pore) and porosities (*e.g.*, 50, 90, 95%) but ignore the definition from the solid skeleton structure. Moreover, there is no uniform standard applied to these definitions, which may lead to overly strict or broad scope.

Therefore, to clarify the scope of this review, we feel that it is necessary to briefly discuss the definition of aerogels, from both a structural and porosity standpoint. We recommend that materials that meet both the following statements can be called aerogels: (i) solids are uniformly dispersed in the whole structure and are connected through nanostructures (nanoparticles, nanofibres, or nanosheets with at least one dimension being <100 nanometres). (ii) The pores formed between the solids are open, filled with gas, and the porosity is no less than 50%. This definition covers all the examples discussed in this review.

With this above definition in mind, in this section, we introduce typical aerogel types, their various physical properties, and their traditional preparation processes and shaping methods.

2.1 Types of aerogels and their properties

A wide range of materials can be used to fabricate aerogels. Examples of typical aerogels and their functional applications are shown in Fig. 1. Aerogels can be classified based on their chemical composition into oxides, carbon, polymers, biomass, metals, non-oxide ceramics, semiconductors, *etc.* Oxide aerogels such as silica (SiO_2),[30,31] alumina (Al_2O_3),[32] zirconia (ZrO_2),[33] and titania (TiO_2),[34] are usually prepared by a sol–gel method using metal alkoxides, nitrates, or chlorides as raw precursors.[35] Since

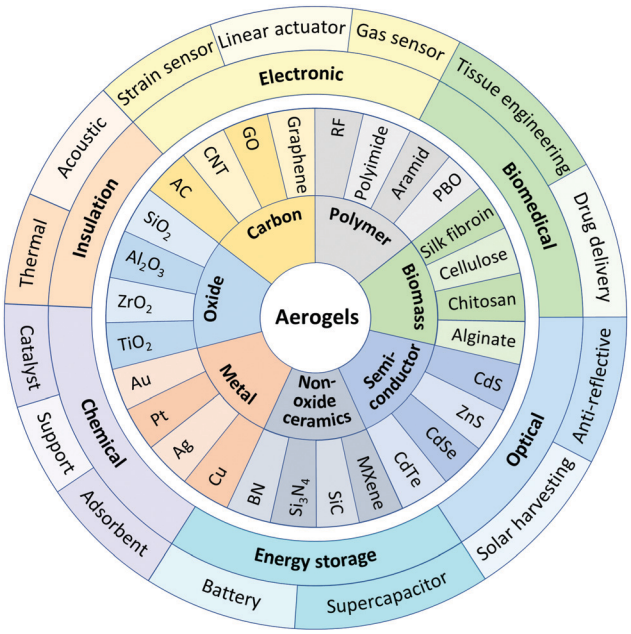

Fig. 1 Typical types and functional applications of aerogels.

oxides typically have high melting points and are not oxidized in ambient environments, their aerogels usually have good thermal stability. Carbon-based aerogels mainly include amorphous carbon (AC),[36] as well as various carbon nanostructures such as carbon nanotubes (CNTs),[37–39] graphene,[40] and graphene oxide (GO).[41] AC aerogels are generally formed by carbonization of organic polymer aerogels, while CNTs, graphene, and GO aerogels are often prepared *via* colloidal methods using these nanomaterials as the skeleton building blocks. In general, carbon-based aerogels are electrically conductive and highly resistant to acid or alkali corrosion. Organic polymer aerogels such as resorcinol-formaldehyde (RF),[42,43] polyimide,[44] aramid,[45] and polybenzoxazine (PBO),[46] are usually obtained *via* polymerization of monomers. Some organic polymer aerogels such as polyimide and aramid exhibit good flexibility. Polymer aerogels, however, generally have poor thermal stability. Exploiting this, certain polymer aerogels such as RF are used as precursors for carbon aerogels *via* pyrolysis in inert atmospheres. Biomass aerogels such as silk fibroin,[47] nanocellulose,[48] chitosan,[49] and alginate[50] are usually synthesized from biomass extracted from creatures and natural materials such as silkworm cocoons, wood and sea shells as raw materials and through cross-linking reactions. Biomass aerogels generally have very good biodegradability and biocompatibility. Metal aerogels such as gold (Au),[51] platinum (Pt), silver (Ag), and copper (Cu) are usually made from their metal nitrates or chlorides *via* sol–gel chemical gelation with sodium borohydride as the reducing agent.[52,53] These aerogels typically exhibit high catalytic activity and durability. Some of the metal aerogels with nanowire-structures exhibit good electrical conductivity and mechanical flexibility.[54,55] Non-oxide ceramic aerogels include nitrides (*e.g.*, boron nitride (BN),[5,56] silicon nitride (Si_3N_4),[57]), and carbides (*e.g.*, silicon carbide (SiC)[58]), and MXene[59] (a 2D carbide and nitride family of transition metals (M), where X represents carbon or nitrogen) aerogels also belong to this group. Non-oxide ceramic aerogels are always prepared by an aerogel template method *via* a gas-solid phase reaction at high temperature,[5,57,58] or by a colloidal dispersion method using the corresponding nanomaterials directly as the building blocks.[59] Thanks to the excellent thermal stability of non-oxide ceramics, these aerogels can usually be used at higher temperatures than oxide aerogels. Semiconductor aerogels such as cadmium sulfide (CdS),[60] zinc sulfide (ZnS),[61] cadmium selenide (CdSe),[62,63] and cadmium telluride (CdTe),[64] are usually fabricated by a colloidal dispersion method, followed by gelation *via* destabilization or freeze casting. These aerogels retain the semiconducting and luminescent nature of the original materials, while their highly porous structure is beneficial for improving photocatalysis, photovoltaic and sensing performances. Depending on the composition and microstructure, different types of aerogels may exhibit different properties, specifically suited to target applications.

2.2 Traditional preparation processes of aerogels

Based on the reaction environment where the nano-skeleton is created, the preparation methods of aerogels can be categorised into three major types. The first is a solid phase route that can be used to prepare perovskite oxide aerogels by solid-state gelation using carbon as the support.[65] This method was first proposed in 2019. The second is the gas phase route with only a few reported examples, such as CNT aerogels by CVD[66–68] or atomic layer deposition,[69] and BN aerogels by template-assisted CVD.[5,70] The third is the traditional and the most popular liquid phase route; Fig. 2. This involves creation and aging of sol-gels in solutions, followed by specific drying methods such as supercritical, freeze, or ambient drying. We note that for the case of nanoparticle-, nanofibre- or nanosheet-based aerogels, the primary sol step may not always be necessary.[27,71] The most important and essential processes in the preparation of aerogels are the formation of a gel and its subsequent drying.

2.2.1 Gel preparation process. The formation of the gels can be divided into two types, one being the classic 'sol–gel method' starting from molecular precursors,[26] and the other being the 'colloidal dispersion method' starting from pre-formed nano-scale materials such as nanoparticles, nanotubes, nanowires, and nanosheets.[71]

The sol–gel method is generally used to prepare inorganic oxide,[72–74] organic,[6,75–77] and chalcogenide[78,79] aerogels, and always uses organic alkoxides,[73] metal chlorides,[74,80] nitrates,[81] small organic molecules,[75,76] biopolymers,[6] or prepolymerized molecules[82] as the molecular precursor. Depending on the precursors used, the chemical reactions and gelation mechanisms vary.

The sol–gel chemistry of these aerogels has been comprehensively summarized in ref. 26 and 83. A simplified and generalised discussion on this process can be made for the most common SiO_2 aerogels,[84] where silicon alkoxides,[85,86] sodium silicate,[87] or prepolymerized siloxanes[82] are used as molecular precursors. Among them, silicon alkoxides $Si(OR)_4$ such as tetraethylorthosilicate (TEOS, $Si(OCH_2CH_3)_4$) and tetramethylorthosilicate (TMOS, $Si(OCH_3)_4$) are the most widely

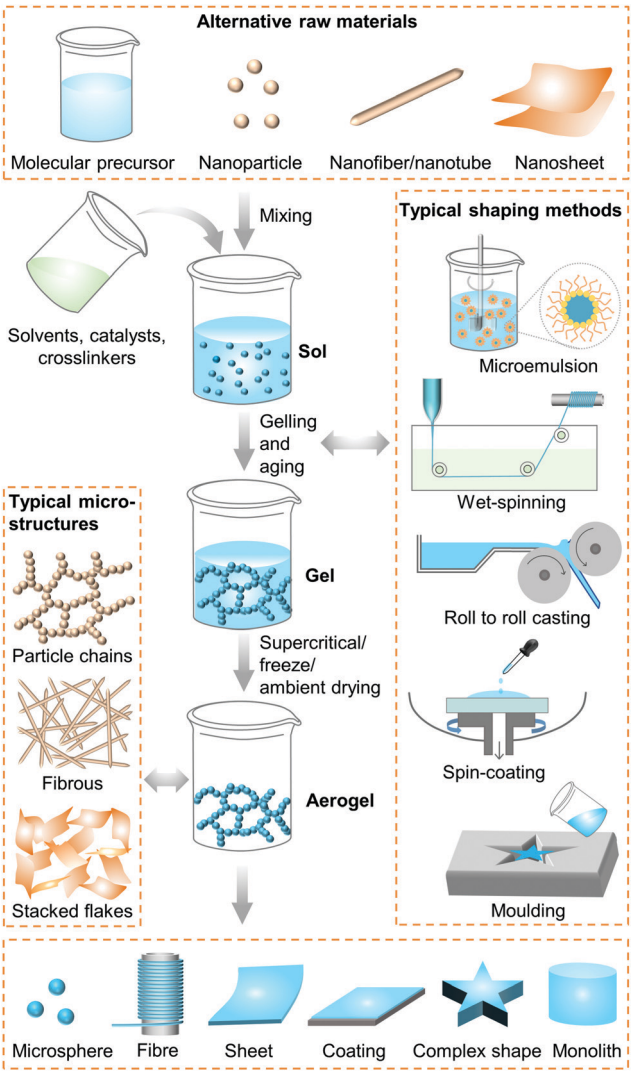

Fig. 2 Traditional liquid phase preparation processes and shaping methods of aerogels.

used.[85,86] This is because the hydrolysis and condensation rates for these materials are slow enough to be independently controlled, allowing for adjustment of the aerogel microstructure to suit different applications.[88] The $Si(OR)_4$ precursors are usually dissolved in solvents containing water and alcohol, and are hydrolyzed by acid (*e.g.*, hydrochloric acid, nitric acid) or base (*e.g.*, ammonium hydroxide, ammonium chloride) catalysts to form the molecular structure of Si–OH. The hydroxyl groups are then dehydrated and condensed to form a bridged Si–O–Si structure. This reaction process gradually forms nanoparticles in the solvent, with typical sizes in the range of a few nanometres to tens of nanometres. In this state, the suspension with nanoparticles dispersed in solution is called a sol. As the reaction progresses, the nanoparticles cross-link with each other to form a 3D networked structure with solvent in the pores, and the sol loses its fluidity and becomes a gel, like a viscoelastic solid. This transition from sol to gel is commonly called gelation. The sol–gel process is essentially a nucleation and growth process.[84]

The colloidal dispersion method skips the molecular step and directly uses nano-scale materials as the aerogel building blocks.[27,71] A wide variety of starting materials have been investigated, including 0D oxide,[89] semiconductor chalcogenide,[61] and metal nanoparticles,[62,90,91] 1- and quasi-1-D metal nanowires,[92] CNTs,[37] and cellulose nanofibres,[93] as well as 2D graphene sheets,[94] and MXene.[59] The dispersions of these nanomaterials can be broadly considered as colloids, either through steric or charge-stabilisation. Their specific gelation strategies have been summarized in detail in ref. 71. The 3D network structure from these materials is formed by physical or chemical cross-linking. The colloidal dispersion method is not limited to sol–gel chemical reactions, greatly expanding the types of aerogels that can be produced. During the preparation of the gel, the gelation time and density, particle size, pore size and other performance parameters of the final aerogels can also be controlled by adjusting a range of process parameters, such as the concentration of the starting nanomaterial, the type and concentration of catalysts, as well as processing temperature, making it a highly adaptable fabrication approach.[84]

2.2.2 Drying process. For the drying of the wet gel, it is necessary to reduce the surface tension which otherwise may shrink or damage the gel structure. There are three main drying methods: supercritical drying, freeze drying, and ambient drying, with corresponding phase change processes being liquid-supercritical fluid–gas, liquid–solid–gas, and liquid–gas, respectively.

Aerogels were first invented through supercritical drying in the 1930s.[24] Since then, supercritical drying has remained the most popular drying method for aerogels. Indeed the majority of today's industrial production of aerogel thermal insulations still uses CO_2 supercritical drying.[95] After the 1990s, to reduce the cost and increase safety, extensive research investigations have been carried out to introduce ambient drying after solvent exchange, network strengthening, and surface modification.[96–98] The biggest disadvantage of ambient drying is the large linear shrinkage of the aerogels, which can reach up to 15–25%.[96] It may even be higher for the case of ultrahigh-porosity gels due to the weak strength of the gel skeleton.

The earliest freeze drying for aerogels appeared in 1989.[99] However, when it was first introduced to dry oxide aerogels from alkoxide precursors, formation of cracks usually led to aerogel powders because of the volume expansion during the liquid-ice phase change.[74] The use of freeze drying therefore remained very limited. However, since the advent of aerogels made from 2D materials such as graphene,[100] freeze-drying has become the most commonly used drying method over the last 10 years.[101] This is especially the case for aerogels with ultralow densities below 5 mg cm^{-3},[52,54,102–109] since the flexibility of these 2D material skeletons can endure the expansion of liquid-ice phase change.

2.2.3 Traditional shaping methods. Thus far aerogels with different shapes such as microspheres, continuous fibres, sheets, coatings, and complex parts, have been prepared by a variety of traditional shaping methods. Aerogel microspheres can typically be prepared by electrospraying[110] or emulsion

processes.[111] Under mechanical stirring, the sol is mixed with another liquid which is insoluble with the solvent in the sol. This forms a microemulsion liquid, resulting in simultaneous gelation to form gel particles. Continuous aerogel fibres can be fabricated by traditional wet-spinning technologies for flexible aerogels such as graphene.[112–114] For preparing an aerogel coating, *i.e.*, thin-film on a substrate, a sol can be deposited onto a substrate such as a silicon wafer by spin-coating.[115–117] Self-supported polymer aerogel sheets can also be prepared by moulding methods[44] or roll-to-roll casting.[118] For the latter, the prepared sol and a base film can be passed through double rolls to compress the sol into a thin sheet on to the base film. After rapid gelation, the base film can be peeled off and the self-supporting gel sheet can subsequently be used for supercritical drying.[118] For the preparation of aerogel parts with complex shapes, traditional moulding methods can be used by pouring the sol into the cavity of the mould. After subsequent gelation, the mould can be opened to take out the gel, followed by supercritical drying.[119] However, in this process, the achievable aerogel shape complexity is very limited due to mould design requirements. Indeed, using these traditional methods, if not impossible, it is highly challenging to create intricate aerogel structures with complex macropores. And this is where 'printability' of aerogels can make a huge impact.

3. Functional printing

Among the existing manufacturing pathways, functional printing represents a group of technologies that can turn powders, liquids, or slurries into patterns or 3D shapes, even with complex geometries. Indeed, functional printing has brought about great innovations in the field of material processing technologies. In particular, workpieces or devices can be printed based on 3D printing, and can be constructed on demand, even with design modifications promptly and inexpensively.

3.1 Printing technologies for additive manufacturing

Printing is an additive manufacturing process that exemplifies cost-effective production technologies suitable for either industrial scale-up or prototyping. This has propelled functional printing to the forefront of the materials manufacturing revolution. Compared to the traditional material removal-cutting and assembly processing mode, printing is a "bottom-up" manufacturing method by material accumulation, from scratch. It is significantly more adaptable and potentially less expensive compared to the traditional moulding method, and offers the production of structurally complex parts that were not previously possible.

The traditional functional printing technologies are borrowed from graphics printing, and include inkjet, screen, and roll-to-roll gravure and flexographic printing.[120,121] Among these, inkjet printing is a non-contact, mask-less, fast, and low-cost method with excellent design flexibility, and is the most popular choice for laboratory-scale or high-resolution additive manufacturing for functional devices.[122,123] The drawbacks of inkjet printing are the throughput, strict ink formulation requirements and also, the concentration of functional materials in the resultant inks. These can be addressed by a wide range of modern 3D printing technologies, such as binder jetting, directed energy deposition, material extrusion and jetting, powder bed fusion, sheet lamination, and vat photopolymerisation.[17,124–127] Although the resolution of 3D printing is often lower when compared to inkjet printing, the latter has seen rapid development over the past few years. Indeed, highly versatile printing strategies have already been demonstrated for metals,[128–135] polymers,[136–143] ceramics,[144–148] inorganics,[149,150] semiconductors,[151] and biomaterials,[152,153] as they can be directly or indirectly printed to form application-specific patterns or 3D shapes.

3.2 Products and applications enabled by functional printing

Fig. 3 shows a set of examples that can be fabricated by functional printing technologies. Combining with computer-aided design, they can be used to manufacture complex patterns,[131,132] electrodes,[149] hierarchical scaffolds,[140,144] intricate load-bearing parts for heavy construction equipment like excavators,[129] concrete walls,[150] human implants,[130,152] tissue frameworks,[153] and even soft robots in a single print without assembly.[139] Such versatility directly leads to products that can be applied in diverse areas such

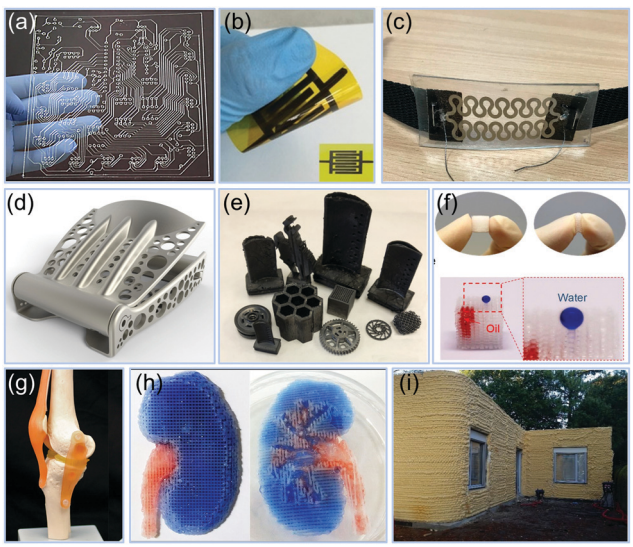

Fig. 3 Examples of objects fabricated by functional printing technology. (a) Extrusion printed electronics interconnect pattern. Reproduced from ref. 135. Published by Springer Nature. (b) Screen printed microsupercapacitor. Reproduced with permission from ref. 154. Copyright 2019 WILEY-VCH. (c) Inkjet printed respiration rate sensor. Adapted from ref. 132. Published by MDPI. (d) Ti-6Al-4V seat buckle produced using direct metal laser sintering technology. Reproduced with permission from ref. 156. Copyright 2015 Elsevier Inc. (e) Polymer-derived ceramic parts fabricated *via* 3D printing. Reproduced with permission from ref. 148. Copyright 2018 WILEY-VCH. (f) Polydimethylsiloxane (PDMS) sponge for 3D water/oil separation by 3D printed template. Reproduced with permission from ref. 140. Copyright 2018 Elsevier B.V. (g) 3D printed menisci in a knee model. Adapted with permission from ref. 152. Copyright 2017 American Chemical Society. (h) 3D printed kidney structure composed of heterogeneous tissue parts. Reproduced from ref. 155. Published by Springer Nature. (i) 3D printed foam and concrete for construction. Adapted with permission from ref. 150. Copyright 2019 Elsevier B.V.

as sensors,[138,151] energy storage,[149,154] surgery,[130,152] tissue engineering,[153,155] electronics,[135] mechanical parts,[139,156] environmental remediation,[140] automobiles and aerospace,[133] and even in building construction.[150,157] In the majority of cases, the printed products do not require any subsequent processing before use. Therefore, the design to manufacturing, and to subsequent application time is greatly reduced.

The required conditions for printing aerogels are relatively mild and usually do not involve very high temperatures. Therefore, the most commonly used printing technologies for aerogels are inkjet and screen printing for patterned thin-films, and photopolymerization, extrusion-based printing, and 3D printed templates for 3D scaffolds or complex shapes. In addition, inkjet printing can also be used to fabricate aerogel microspheres.

3.3 Benefits of printing compared to other aerogel shaping methods

Regardless of the fabrication techniques, aerogels are usually fragile due to their low solid content and nano-skeleton architecture. Compared to traditional aerogel shaping methods, the "bottom-up" additive manufacturing of functional printing methods for aerogels has some unique advantages. Table 1 lists a comparison between the reported aerogel printing techniques and the traditional aerogel shaping methods to create microspheres, fibres, supported and self-supported thin-films, complex geometries, and 3D scaffolds.

Aerogel microspheres or microparticles can traditionally be prepared using several schemes, including emulsion-gelation,[111,158] Stöber,[159,160] spraying or electrospraying,[110,161,162] and supercritical fluid[163,164] methods. The diameters of the microspheres in these strategies are primarily controlled by either chemical reaction, applied voltage, or stirring and air flow rate. However, in practice, the batch-to-batch reproducibility in this approach is very challenging. There are various ways to limit these variations in the synthesis conditions. For example, if rotary stirring is used to synthesize aerogel particles, the size of the droplets deposited into the emulsion can be controlled through the precision nozzle of the inkjet printing, allowing synthesis of highly monodisperse microspheres.

On the other hand, traditional freeze- or wet-spinning technologies can be exploited to fabricate aerogel fibres.[165] These methods can usually be used for flexible aerogels only, such as those made with graphene,[112–114] GO,[166] cellulose,[167–170] and polyimide.[165] Filaments can be fabricated using a 3D extrusion method, which is somewhat similar to the traditional spinning techniques. However, the added advantage here is that the filaments can be directly printed onto the substrate to form a device,[171] without worrying about the mechanical robustness of the aerogel, or its transfer and integration on to the target substrate.

Substrate supported thin-films of aerogels can be prepared by the traditional spin coating,[115–117] dip coating,[172,173] and spray[174,175] methods. However, these methods can hardly be used to create patterns without masks or stencils. Inkjet or screen printing can offer significant advantages here. First, they would allow creation of aerogels with specific patterns. Second, the thickness of the resultant coating could be better adjusted through ink formulation and/or printing parameters.

Self-supported aerogel thin-films can be conventionally prepared using roll-to-roll casting methods.[118] The obtained aerogel film can then be additionally processed into the desired patterns, for example, by cutting. On the other hand, 3D printing offers the distinct advantage of direct patterning of self-supported thin-films, without the loss of any material.

Complex aerogel parts can be traditionally fabricated by pouring the sol into a mould,[119] which, after gelation, is supercritically dried. The bulk aerogel may additionally require mechanical cutting or milling. This process, involving multiple steps, can only create structures with limited complexity. In contrast, 3D printing does not require a mould and can create significantly more complex structures. Additionally, due to the use of a computer aided approach, it is straightforward to modify the design of the aerogel shapes, significantly simplifying prototyping or production of specialised parts.

Similarly, 3D aerogel scaffolds cannot be realized through traditional shaping methods without using templates. On the other hand, from digital scaffold designs, 3D printing methods such as stereolithography (SLA),[22] extrusion,[176] or sacrificial 3D printed mould[177] can be used to create 3D aerogel scaffolds with fine structures. As before, the adaptability in the design and adjustment of the channels, pore types, and porosity offers an added advantage. These can in turn be used to adjust the physicochemical properties of the scaffolds such as adsorption, mass transfer, and electrical conductivity for specific applications.

Fragile aerogels are very challenging to shape using traditional moulding and processing methods, especially in the

Table 1 Advantages of printing compared with other shaping methods for aerogels

Shape of aerogel	Traditional shaping method	Printing method	Advantages *via* printing
Microsphere	Emulsion-gelation, Stöber, spraying, supercritical fluid	Inkjet printing with spinning	Simple control in diameter and good repeatability
Fibre	Spinning	Extrusion 3D printing	No requirements on fibre's flexibility, can directly form a device
Supported thin-film	Spin-, dip-coating, spray	Inkjet, screen printing	Easy access to patterns
Self-supported thin-film	Casting	3D printing	Easy access to patterns
Complex part	Moulding	3D printing	Without mould
3D scaffold	—	Extrusion 3D printing or sacrificed 3D printed mould	Complex structure easily available, good controllability of macrostructure size

micron scale. In the majority of cases, the functional printing methods can enable designing and shaping of aerogels on tens to hundreds of micron scale, addressing a critical shortcoming of the traditional sol–gel and mechanical processing methods. The controllability of the nanostructures through aerogel chemistry, and the macrostructural construction offered by various printing methods enables adaptability and precise control over aerogel designs from nanometre to centimetre scale. This significantly shortens, simplifies and improves the processes from basic chemicals or nanomaterials to useful device components, while reducing the production cost. In the next section, we discuss the processing and chemistry of printed aerogels in terms of ink preparation, drying, and post-treatment.

4. Printing technology for aerogels

Printed aerogels were first reported in 2015,[18] realized by extrusion-based 3D printing of GO-based inks. Since then, printing of a wide variety of aerogels, including of graphene,[178] SiO_2,[179] RF polymer,[180] carbon,[19] cellulose,[181] metal,[54] semiconductor,[182] and g-C_3N_4[183] have been reported. The technologies that have thus far been used to print aerogels include inkjet for microspheres,[184] inkjet and screen for substrate-bound thin-films,[182,185] and photopolymerization (light-based printing),[22] extrusion[186] and sacrificial template[177] for 3D form factors. Simplified printing mechanisms of these technologies for aerogels are summarized in Fig. 4.

The fabrication processes of the printed aerogels involve several steps: mixing of raw materials into highly consistent fluids with appropriate rheology/physical characteristics (*i.e.*, formulation of functional ink), extrusion/printing, drying, and additional post curing processes such as pyrolysis or etching. Among them, the last two steps can be borrowed from conventional aerogel preparation processes, and therefore, are not particularly challenging to implement. Conversely, the first two steps, ink formulation and printing, face a range of technical difficulties and challenges. This is primarily due to the requirements of the specific printing technologies used, which can affect printing quality and feature resolution.

Based on the processes involved in printing of aerogels, the relevant technical characteristics and classifications are summarized in Fig. 5. In the following, we introduce them and related research progress in accordance with the sequence in Fig. 5.

4.1 Ink preparation processes and chemistry for printed aerogels

The word "ink" usually refers to a liquid or paste with suitable viscosity and rheological properties, specifically for inkjet, screen, certain types of 3D extrusion, or photopolymerization printers. Depending on the printing technique, a functional ink is usually composed of the active material, additives (*e.g.*, binders and surfactants), and solvents. The matching of ink rheological properties specific to printing methods determines their printability.[187] These rheological properties as well as the microstructure and

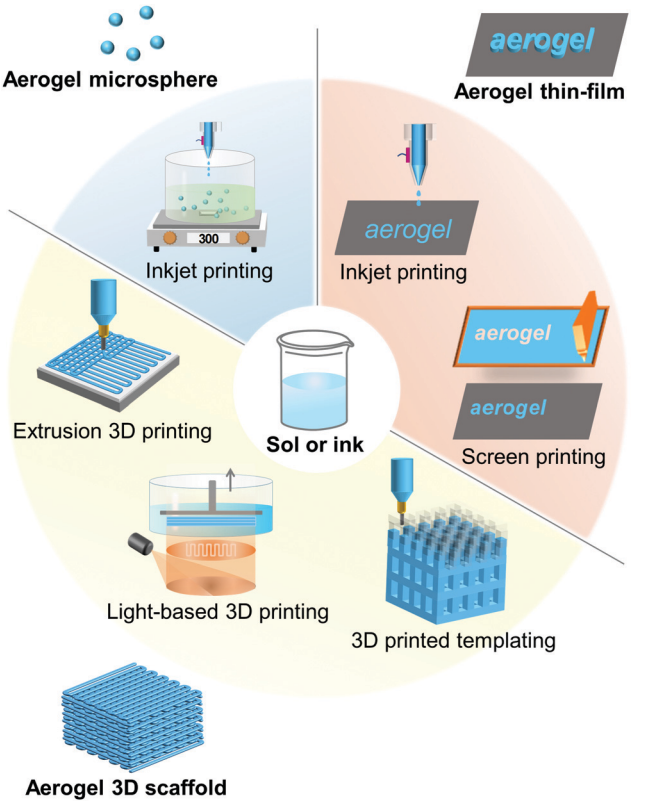

Fig. 4 Commonly employed printing technologies for aerogels: inkjet printing for microspheres, inkjet and screen printing for patterned thin-films and extrusion, light-based printing, or 3D printed templates for 3D aerogel structures.

final characteristics of the printed aerogels can be controlled by the process parameters in the ink preparation process, such as the ink composition, raw material morphology, and formulation. Based on different gelation principles in inks, we divide the discussion in this section into molecule-derived and nanomaterial-derived pathways. The chemical reaction processes follow the traditional sol–gel method which we will not repeat here. For this, we refer interested readers to ref. 188. In this review, we will mainly focus on the chemical reaction limitations caused by the printing requirements, as well as raw materials and reactions that may be specifically tailored for printing.

4.1.1 Ink's rheological property requirements for printing. Printing is the flow and transfer process of a liquid ink. When the liquid is forced to flow, an internal friction force that hinders the relative movement between the liquid molecules is generated due to the cohesive forces between them. The term viscosity is the measure of this internal friction force, *i.e.*, the ability of a liquid to resist shear deformation. The viscosity is usually characterized by the ratio of shear stress to shear rate. It is related to the ink concentration, substance type, and temperature.[189]

Shear stresses in fluids may show a linear or nonlinear relationship with the increase in shear rates, that is, the viscosity may remain constant or vary with increasing shear rate. Based on this, fluids can be divided into Newtonian and

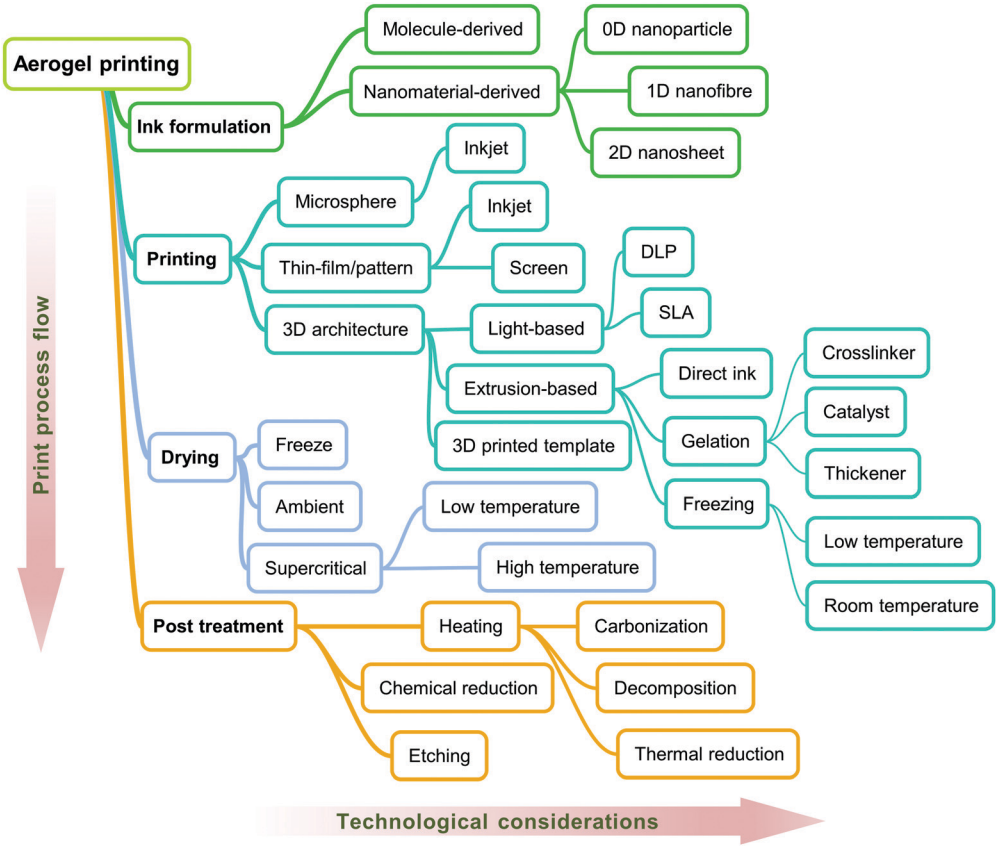

Fig. 5 Relevant technical considerations for aerogel printing.

non-Newtonian types.[190] Fig. 6a shows the variation of shear stress with shear rate for various fluids.[191] As shown, the shear stress of a Newtonian fluid increases linearly with increasing shear rate (thus the viscosity remains constant, Fig. 6b).[191] Newtonian fluids can therefore flow under a small external force. Liquids close to this ideal state, such as water, solvents, and mineral oil, are generally considered to be Newtonian fluids for practical calculations at standard conditions.

The viscosity of non-Newtonian fluids is variable, and based on their decrease or increase with increasing shear rate, they can be classified into shear-thinning (pseudoplastic) and shear-thickening (dilatant) fluids (Fig. 6b).[190] Shear-thinning behaviour of fluids is very important for the printing process. It ensures smooth flow of ink under a driving force during printing. Additionally, these fluids can maintain a certain level of self-support to retain the printed shape or pattern after the driving force is withdrawn. Polymer solutions, melts, and greases are generally shear-thinning fluids. In contrast to the shear-thinning fluids, the viscosity of the shear-thickening fluid increases with increasing shear rate. When at rest, it can gradually restore the state where it 'flows' easily. Aqueous solutions of potassium silicate and gum arabic are typical examples of shear-thickening fluids.

In addition to viscosity, viscoelasticity also plays an important role in the printability of inks.[192] The storage modulus (G') and loss modulus (G'') characterize the ink's elasticity and viscous properties, respectively. The storage modulus, also known as elastic modulus, refers to the amount of elastic (reversible) energy stored by deformation and reflects the elasticity of a material. The loss modulus, also known as the viscous modulus, refers to the amount of energy lost due to viscous deformation (irreversible). The ratio of the plateau values of the storage modulus to the loss modulus (G'/G'') reflects the viscoelasticity of the material. When the storage modulus is much greater than the loss modulus ($G' \gg G''$), the material mainly undergoes elastic deformation, indicating that the substance is closer to a solid state. On the other hand, when $G' \ll G''$, the material mainly undergoes viscous deformation, indicating that the substance is closer to a liquid state. When the storage and loss modulus are comparable, the material is in a semi-solid state. A gel is a typical semi-solid substance. The stress where the storage modulus begins to decrease with increasing shear stress, is called yield stress; Fig. 6c. This indicates the applied stress required to make the substance flow with irreversible plastic deformation.[193] The point at $G' = G''$ is the transition point from solid-like to liquid-like state. For high viscosity printing such as screen and extrusion-based techniques, there needs to be a balance between G′ and G''.[192] A high-enough magnitude of G′ and G'' (the value at the plateau region in Fig. 6c),[194] and a suitable yield stress[193,195] are important for effective printability of the ink in these cases.

In inkjet printing, viscosity and surface tension greatly affects the formation of ink droplets. The ejection behaviour

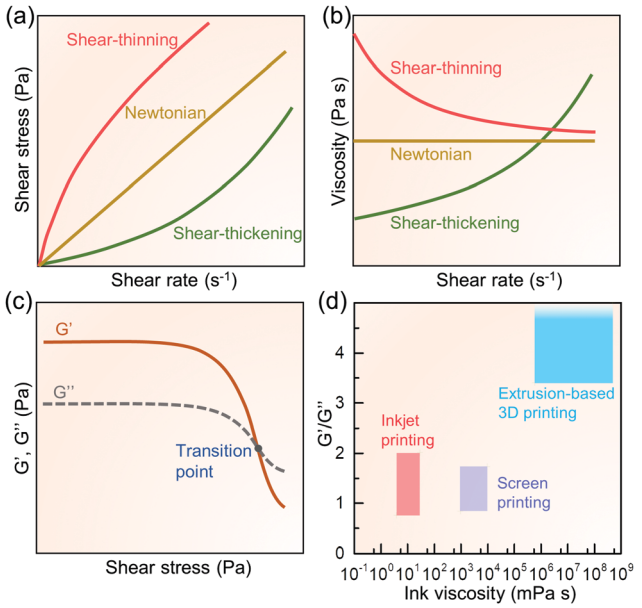

Fig. 6 Newtonian and non-Newtonian fluids with (a) shear stress and (b) viscosity as a function of shear rate. (c) Typical storage (G') and loss (G'') modulus of shear-thinning non-Newtonian fluid as a function of shear stress. (d) Expected ink viscosity and G'/G'' ranges suitable for different printing methods, data collected from ref. 120, 192, 201 and 203.

of such droplets from printing nozzle can be characterized by Z, which is the inverse of the dimensionless Ohnesorge (Oh) number:[196]

$$Z = \frac{1}{\mathrm{Oh}} = \frac{\sqrt{\gamma \rho a}}{\eta} \quad (1)$$

Among them, η, γ, and ρ are the viscosity, surface tension, and density of the ink, respectively, and a is the diameter of the nozzle. Through numerical simulation, it has been proposed that $1 < Z < 10$ is considered suitable for inkjet printing for stable drop formation.[197] However, although this proposed range facilitates reliable jetting, it is not very strict. For example, it has been shown through experiments that $1 < Z < 14$ is sufficient to satisfy drop-on-demand (where individual droplets are ejected through the nozzles for each electrical actuating signal) inkjet printing.[198–200] When $Z < 1$, the fluid is too viscous. This may cause the tail of the droplets to be elongated and drawn, or even failure of droplet formation. When $Z > 14$, the viscosity is so small that the droplets are easily broken, forming satellite droplets (secondary droplets), or sputtering after coming in contact with the substrate, reducing the print reliability and resolution. Compared to screen printing, the inks used for inkjet printing have a much lower viscosity, generally in the range of 4 to 30 mPa s,[120,201] which is similar to that of water at 20 °C (1.0016 mPa s).[202] The G'/G'' for inkjet printing is typically in the range of 0.74 to 2 to allow for reliable printing (Fig. 6d).[203]

Screen printing uses a squeegee to scrape the ink from one end toward the other of the screen mesh, forcing the ink to penetrate through the pre-made holes to form a graphic printed on the substrate.[192] A suitably high viscosity with shear thinning behaviour is needed to retain the transferred patterns on the substrate before the inks are 'cured'. Too low viscosity may reduce the clarity of the printed graphics, while inks with too high viscosity with poor shear thinning property are difficult to transfer through the patterned openings in the screen mesh.[204] The viscosity and the G'/G'' of screen printing inks are generally in the range of 1×10^3 to 1×10^4 mPa s[120,201] and 0.8 to 1.7 (Fig. 6d),[192] respectively.

3D printable inks must have high viscosity to ensure that the printed structure is self-supporting, *i.e.*, the extruded filaments do not collapse, or disperse after the applied shear force is withdrawn. In addition, as above, the inks must also have shear-thinning rheological properties. When the ink flows through the extrusion nozzle (usually with a diameter of tens to hundreds of microns) under pressure, the viscosity must be thinned to be low enough to prevent nozzle clogging and ensure continuous filament extrusion. Generally, the viscosities and the G'/G'' of 3D printing inks are in the range of 6×10^5 to 5×10^8 mPa s and >3.4 (Fig. 6d),[187,203] respectively. Besides high viscosity and high G'/G'', high modulus in the plateau region and high yield stress are also required for extrusion-based 3D printing to prevent collapse of the printed object due to gravity and the pressure imposed by the extrusion nozzle.[195]

Light curing-based printing, whether it is a top-down system of SLA or a bottom-up projection system of digital light processing (DLP), requires the light-curing resins to quickly flow back into the gap formed after the workpiece is moved for the construction and light-curing of the subsequent layer. Hence, the requirement for the viscosities of the light curing resins is as low as possible to effectively and quickly backfill.[142]

4.1.2 Molecule-derived gel inks. The molecule-derived gel inks that have been developed thus far have focused on printing SiO_2-based,[179,184,205–208] RF,[19,180] and alginate aerogels.[209] The printing methods compatible with these inks mainly include inkjet,[184,209] light-induced-cross-linking 3D,[205–207] and extrusion 3D printing.[19,179,180] Table 2 shows selected examples of molecule-derived gel inks printed using these methods.

As discussed above, inkjet printing generally requires the ink to have low viscosity for reliable ejection of ink droplets from the nozzle. On the other hand, 3D extrusion-based printing requires the ink to have a relatively high viscosity to ensure that the printed filaments are self-supporting to retain their structure before curing.[191]

The traditional molecule-derived sols always have a low viscosity and can be directly used for inkjet printing without any special modification of the sol formulation. For example, SiO_2 sol, prepared by a traditional two-step acid–base process, has directly been used for inkjet printing to prepare SiO_2 aerogel microspheres.[184] Similarly, alginate gel microspheres have been successfully demonstrated by inkjet printing aqueous solution of alginic acid sodium salt into calcium chloride ($CaCl_2$) aqueous solution. The concentrations that are feasible for inkjet printing are 0.25–0.35 wt%. If it is >0.4 wt%, the viscosity is too high for printing as it results in high Reynolds and Ohnesorge number of the fluid, or even clogged nozzles.[209]

Table 2 Examples of molecule-derived gel inks for printing aerogels

Composition of aerogel	Shape of product	Main raw material	Printing method	Drying method	Application	Ref.
SiO_2	Microsphere	TEOS, isopropyl alcohol	Inkjet	Ambient	—	184
SiO_2	3D complex object	Dynasylan 40, SiO_2 aerogel particle, PPGNH, 1-pentanol	3D extrusion	Supercritical	Thermal insulation	179
SiO_2–silk fibroin	3D grid	Silkworm cocoons, TMOS, trimethoxysilane	3D extrusion	Supercritical	Thermal insulation	207
SiO_2–polymer	Letter pattern	TEOS, TMSM, ethanol–water	Photo-cure	Supercritical	—	205 and 208
SiO_2–polymer	3D complex structure	TEOS, APTMS, 2,4,6-trimethylbenzoyl-diphenyl-phosphineoxide, ethanol–water	3D DLP	Ambient	Optical devices	206
Alginate	Microsphere	Alginic acid sodium salt, salbutamol sulphate, calcium chloride dihydrate	Inkjet	Supercritical	Drug delivery	209
RF	3D microlattice	Resorcinol, formaldehyde, Na_2CO_3, water	3D extrusion	Supercritical	Cell support	180
Carbon	3D scaffold	Resorcinol, formaldehyde, hydroxypropyl methyl cellulose, fumed SiO_2	3D extrusion	Supercritical	Electrode	19

On the other hand, it is challenging to create 3D structures through printing from molecule-derived SiO_2 or RF inks. This is because the inks themselves are not viscous enough to be self-supporting.[180] Two strategies have been proposed to overcome this. The first is to add certain additives to increase the viscosity to retain the shape of the printed structure after 3D extrusion. In one method, SiO_2 aerogel particles and poly(propylene glycol) bis(2-aminopropyl ether) (PPGNH) have been used to increase the viscosity of ethyl silicate-derived SiO_2 sol.[179] In another example, silk fibroin has been introduced into traditional SiO_2 sol to increase the viscosity and create crosslinks between SiO_2 and silk fibroin (Fig. 7a).[207] Hydroxypropyl methyl cellulose and fumed SiO_2 have also been added into traditional RF sols to achieve increased viscosity and the required shear-thinning behaviour.[19]

The second strategy involves the introduction of a photo-curable polymer (usually a chemical containing one or more acrylate groups),[210] which cures under light and induces a rapid gelation. The gel can then be printed using a digital light processing printer.[206] It is also necessary to ensure that the silicon source can be chemically connected with the photocurable polymer such that the final network structure contains a Si–O structure and not just the photo-cured resin. Common photo-curable polymers that have been used for this are trimethoxysilylpropyl methacrylate (TMSM)[205,208] and 3-acryloxypropyl trimethoxysilane (APTMS).[206] An example preparation of the photo-curable ink and the relevant chemical reaction is shown in Fig. 7b. Condensation can occur between Si–OH groups while the free-radical polymerization can take place between acrylate groups under the irradiation of light, resulting in a 3D cross-linked structure to form a gel containing SiO_2.

There have only been a handful of demonstrations of printed aerogels from the traditional molecule-derived gel ink method. A large number of oxide (such as Al_2O_3, ZrO_2) and organic (such as polyimide, melamine) aerogels that can be prepared by traditional sol–gel methods remain unexplored. This is primarily because the sol–gel processes for these aerogels are more challenging to control, for example, due to quick precipitation or gelation of sols, leaving little manoeuvrability for stable enough ink formulation for printing. However, the traditional molecule-derived sol–gel method is still the most effective way to tune the pore sizes in the nanoscale. Therefore, significant research opportunities in combining 3D printing and molecule-derived sol-gels exist.

4.1.3 Nanomaterial-based inks. Nanomaterial-based inks mainly refer to formulations prepared with nanomaterials as the starting material. In this case, the skeleton of the resultant aerogels is defined by the assembly of the nanomaterials themselves, rather than structures grown from the molecules. Based on the shape of the starting nanomaterials, this can be broadly categorized into three key areas: 0D nanoparticles, 1D nanofibres (including nanotubes and nanowires), and 2D nanosheets. The ink preparation process for these inks for printed aerogels is broadly similar to the other ink preparation methods. The difference is that when formulating inks, not only the printability but also the solid concentration and the self-assembly method to control the resultant nanostructure (for example the nanopore size and porosity) must be considered for optimum performance. Below we discuss various aspects of ink formulation of these materials for printed aerogels.

0D Nanoparticle-based inks. Table 3 shows typical examples of 0D nanoparticle-based inks for printed aerogels. These materials are mostly used for inkjet and screen printing. The reported 0D structures include SiO_2 aerogels,[211] milled carbon aerogels,[212,213] magnesium oxide (MgO)-TiO_2 aerogels,[185] and various oxide (zinc oxide (ZnO), cupric oxide, indium oxide, TiO_2, and tin oxide)[214] and semiconducting (CdSe/CdS) nanoparticles.[182]

When aerogels are used for ink formulation, to ensure forming a homogeneous mixture, they are usually dispersed by ultrasonic agitation with the aid of surfactants or polymers in the ink solvent.[185,211,214]

In addition to the above examples, for SLA 3D printing, amorphous SiO_2 nanopowders have also been demonstrated as the SiO_2 source to synthesize porous SiO_2 after thermal treatment at 600 °C.[215]

1D nanofibre-based inks. Table 4 shows selected examples of 1D nanofibre-based inks for printed aerogels. These are primarily based on CNTs,[216] metal,[54,217] and oxide[217] nanowires, nanocellulose,[218–222] and aramid fibres.[223] The key printing methods used are 3D extrusion printing[176,181] or SLA.[22]

Nanocelluloses are a family of nanomaterials derived from wood pulp.[224] To date, cellulose nanofibrils (CNFs)[22,176,216,218,222,225–228] and cellulose nanocrystals (CNCs)[181,220–222,229] have been used to

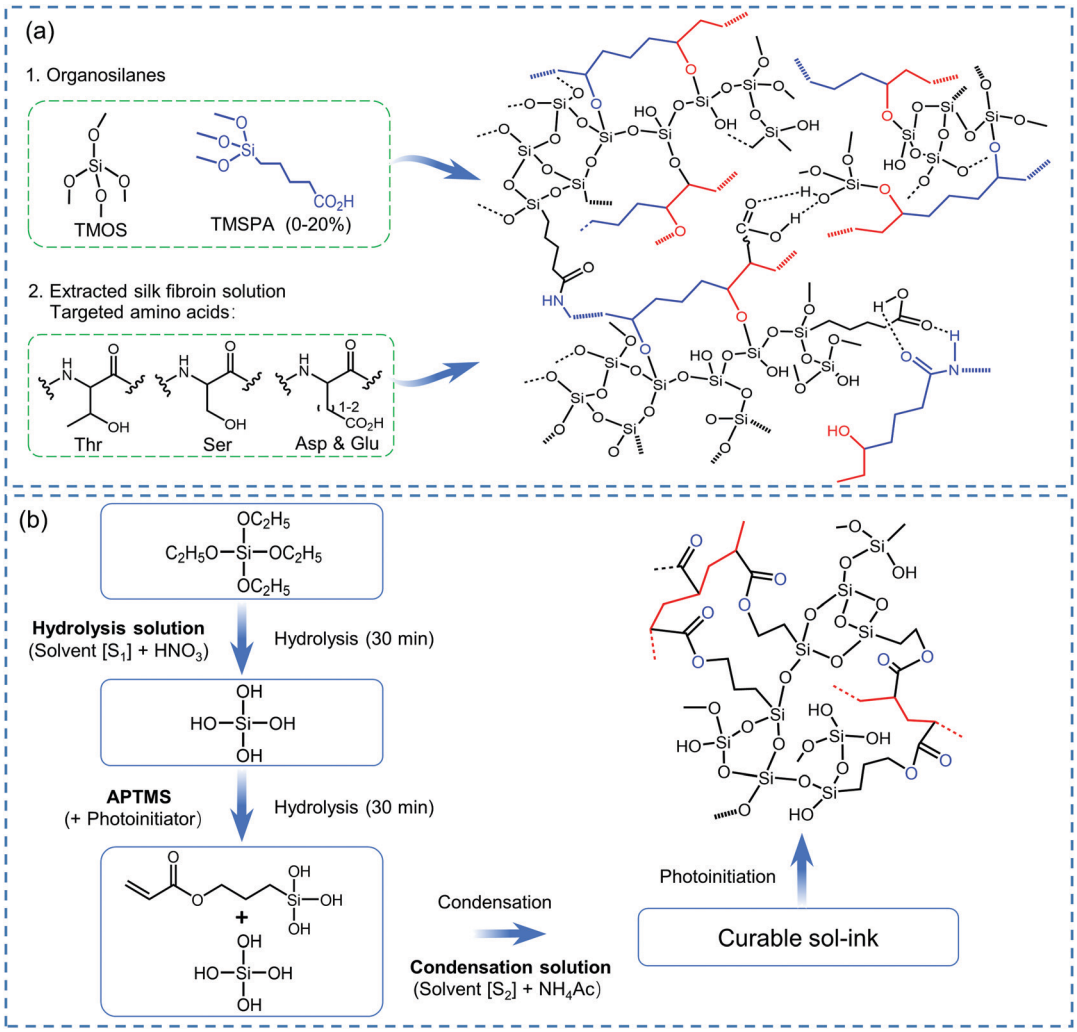

Fig. 7 Schematic diagram of the SiO_2-based ink preparation process and associated chemical reaction. (a) SiO_2–silk fibroin sol for 3D extrusion printing. Adapted with permission from ref. 207. Copyright 2018 American Chemical Society. (b) SiO_2-photocurable polymer sol for 3D digital light printing. Adapted with permission from ref. 206. Copyright 2018 American Chemical Society.

formulate inks for printed aerogels. CNF gels have high viscosity and shear-thinning properties as they are bonded together by strong hydrogen bonds.[218,228] After mixing with water, the gels can be used directly as a 3D printable ink. After printing, placing the CNF gels in a $CaCl_2$ bath can promote cross-linking and increase mechanical strength.[227] CNCs are smaller in length compared to CNFs and as a result, have inferior self-supporting properties. Therefore, cross-linking additives are usually required for CNC inks to improve the printability and stability after printing.[181] A common cross-linking additive for this is polyamide-epichlorohydrin (Kymene).[176,181] Aramid nanofibre-based inks have been developed by using commercial Kevlar fibres as a raw material, dissolving in potassium hydroxide (KOH)-contained dimethyl sulfoxide (DMSO), and then forming a

Table 3 Examples of 0D nanoparticle-based inks for printing aerogels

Composition of product	Shape of product	Main raw material	Printing method	Drying method	Application	Ref.
SiO_2	Pattern	SiO_2 aerogel, DISPERBYK-2012, PVP-k30 binder, 1,5-pentadiol humectant, water	Inkjet	Ambient	Thermal insulation	211
PEDOT:PSS-carbon	Layer	PEDOT:PSS ink, activated carbon aerogel	Inkjet	Ambient	Actuators	212 and 213
MgO–TiO_2	Layer	MgO-TiO_2 aerogel, EVA, p-xylene	Screen	Ambient	Solar cell	185
Metal oxides	Layer	Metal oxide nanoparticles, ethylene glycol, water	Inkjet	Ambient	Electronics	214
CdSe/CdS	Layer	Cadmium oxide, tri-noctylphosphine oxide, tri-noctylphosphine, H_2O_2	Inkjet	Ambient or supercritical	Photo-electrochemical	182

Table 4 Examples of 1D nanofibre-based inks for printing aerogels

Composition of product	Shape of product	Main raw material	Printing method	Drying method	Application	Ref.
CNC	3D complex structure	CNC, Kymene, water	3D extrusion	Freeze	Tissue engineering	181
CNF	3D complex structure	CNF, Kymene, water	3D extrusion	Freeze	Tissue engineering	176
CNF/alginate	3D construct	CNF, alginate, $CaCl_2$, water	3D extrusion	Freeze	Wound dressing	225
CNF/alginate	3D grid	CNF, alginate, $CaCl_2$, water	3D extrusion	Ambient	Energy storage, humidity sensors	226
CNF	3D complex structure	CNF, water, $CaCl_2$ bath	3D extrusion	Freeze	—	227
CNF	3D scaffold	CNF, water	3D extrusion	Freeze	Tissue engineering	230
Carbon-Li, Carbon-$LiFePO_4$	3D anode/cathode	Wood pulp, $LiFePO_4$ powder	3D extrusion	Freeze	Lithium metal battery	218
Cellulose	3D scaffold	Pulp, NMMO	3D extrusion	Freeze	—	219
CNC	3D complex structure	CNC, xyloglucan	3D extrusion	Freeze	Thermal insulators	220
CNC/SA/gelatin	3D scaffold	Cellulose, sodium alginate, gelatin	3D extrusion	Freeze	Tissue regeneration	221
CNC/Au/PAM	3D pattern	CNC, Au, AAm, MBAA, water	3D extrusion	Supercritical	Plasmonic metamaterial	229
CNF	3D scaffold	CNF, water	3D extrusion	Freeze	TENG	228
Aramid	3D grid	Aramid, KOH, DMSO	3D extrusion	Supercritical	Thermoresponsive architecture	223
Ag	3D architecture	Ag nanowire	Inkjet	Freeze	Electronic	54
Ag, MnO_2, ZnO	3D self-support architecture	AgNWs, GO, $Ti_3C_2T_x$, ZONWs, MONWs, CNT	3D extrusion	Freeze	UV sensor, micro-supercapacitor	217
PEGDA/CNF	3D scaffold	PEGDA, eosin Y, CNF	SLA	Freeze	Tissue engineering	22
CNT/GO/CNF	3D all-in-one architecture	CNF, GO, CNT, water	3D extrusion	Freeze	Evaporator	216

dispersion of aramid nanofibres.[45,223] This ink with 2 wt% concentration exhibits enough viscosity and storage modulus for 3D extrusion printing to fabricate aramid aerogels.[223]

Other 1D structures that have been investigated for printing aerogels include CNTs,[216] as well as Ag,[54,217] MnO_2,[217] and ZnO nanowires.[217] The challenge in printing these aerogels is that they usually have fewer chemically active sites compared to those in amorphous nanoparticles, making it often challenging to formulate inks with suitable properties. To address this, a small amount of 2D materials could be used as cross-linking agents to form bridges between nanowires and improve the overall viscosity and printability of the nanowire inks.[217] Such cross-linking ability of GO or MXene with the nanowires has already been confirmed. Indeed, a small amount (0.67 vol%) of GO can greatly improve the printability of Ag, MnO_2, and ZnO nanowire inks.[217]

2D nanosheet-based inks. One of the most exciting developments in the printed aerogels field was the demonstration of 3D printing of 2D GO inks and their annealing to form graphene aerogel scaffolds in 2015.[18] Since then, the published literature reports related to the printing of 2D nanosheet-based aerogels have significantly outnumbered those on 0D- or 1D-nanomaterial-based aerogels. Table 5 shows selected examples of 2D nanosheet-based inks for printed aerogels. The 2D materials that have thus far been used include graphene,[178,231,232] GO,[18,41,109,233–238] and g-C_3N_4 nanosheets,[183] the former two being the most common examples. The printing methods involved are primarily extrusion-based.[171,186,231,233,239,240] In addition, drop-on-demand inkjet,[109,238,241,242] projection micro-SLA (PmSLA) 3D printing,[243,244] and 3D printed templates[245,246] have also been used. The other constituents of the ink formulations for 2D nanosheets are solvents, and additives such as surfactants, crosslinkers, or thickeners, in which, water and organic solvents are primarily used. To increase the viscosity and printability, hydroxypropyl methylcellulose (HPMC),[21,237] fumed SiO_2 powder,[18,20] RF sol,[18] methyl cellulose,[247] ascorbic acid,[107] polyaniline,[248] sodium alginate,[249] *etc.* have been used as cross-linkers, gelators, or thickeners. However, the surfactants or thickeners used in the inks usually need subsequent removal through post-treatment processes such as washing, acid etching or pyrolysis.

It is apparent from Table 5 and the above discussion that the most commonly used 2D material for printed aerogels is graphene. Even though several other 2D materials such as hexagonal BN (*h*-BN),[250] MXene,[59,108] and molybdenum disulphide (MoS_2) have recently been investigated,[29,251,252] there exists a huge opportunity for fundamental research and application development for other 2D material printed aerogels.

4.2 Printing processes

Based on the shape and dimension of the intended macroscopic aerogel objects, printing methods can be grouped into three categories: microsphere, thin-film/pattern, and 3D architecture. This section discusses the ink requirements for these materials, which vary between the printing methods and the technologies used.

4.2.1 Printing aerogel microspheres. Wet spinning is a traditional method that can be used to synthesize aerogel beads using dropwise extrusion, usually by injecting the aqueous precursors through a syringe into a rotating coagulation bath containing the catalyst.[40,253–255] The diameters of these beads are relatively large, and can reach millimetre range. The syringes used in wet spinning can be replaced with an inkjet printer. In general, the nozzle diameter of an inkjet printer can be as small as 10–30 μm, and the volume of a single ink droplet ejected each time is usually 1–20 pL.[191] In this case, combining with the control over ink formulation, it is possible to obtain micron or submicron aerogel microspheres. Indeed, based on molecule-derived inks, inkjet printing has been exploited for the

Table 5 Examples of 2D nanosheet-based inks for printing aerogels

Composition of product	Shape of product	Main raw material	Printing method	Drying method	Application	Ref.
PDMS/graphene	3D sensor	GO, PDMS, PVA, THF	3D extrusion	Freeze	Tactile sensor	240
Graphene	3D microlattice	GO, fumed SiO_2, resorcinol, formaldehyde	3D extrusion	Supercritical	—	18
Graphene	3D microlattice	Graphene, GO, fumed SiO_2, RF	3D extrusion	Supercritical	Supercapacitor	20
Graphene	3D truss architecture	GO, water	Inkjet	Freeze	Strain sensor	109
Graphene	3D monolith	GO, water	3D extrusion	Freeze	—	256
Graphene	Pattern	GO, water	3D extrusion	Freeze	Strain sensor	171
Graphene	3D lattice	GO, EDA, water	Inkjet	Freeze	Sodium metal anode	238
Graphene	3D pattern	Phenol, camphene, graphene, rGO, CNT	3D extrusion	Sublimation	Supercapacitors	178
Graphene/Cu	3D electrode	Cu, graphene, Pluronic F127	3D extrusion	Freeze	Supercapacitors	231
Graphene	Pattern	GO, water	3D extrusion	Freeze	Wearable sensor	235
PPy-graphene	3D microlattice	GO, Pluronic F127, PPy	3D extrusion	Freeze	Supercapacitors	234
Graphene	3D scaffold	GO, water	3D extrusion	Freeze	Pressure sensor	107
Graphene-carbon	Micro-electrode	Carbon sphere, GO	3D template	Freeze	Micro-supercapacitor	246
Graphene	3D scaffold	Graphite	3D extrusion	Freeze	—	257
Graphene-CNT	3D lattice	GO, $CaCl_2$, CNT	3D extrusion	Freeze	Strain sensor	258
Graphene-polymer	3D lattice	GO, $CaCl_2$, polycaprolactone	3D extrusion	Freeze	Fuse, micro-oscillator	236
Graphene	3D electrode	GO, water	3D extrusion	Freeze	Supercapacitor	233
Graphene	3D web	Graphite, water	3D extrusion	Freeze	Tactile sensor	259
MnO_2/graphene	3D scaffold	GO, HPMC	3D extrusion	Freeze	Supercapacitor	21
MnO_2/graphene	3D electrode	GO, $KMnO_4$, HCl	Inkjet	Freeze	Supercapacitor	241
ZnV_2O_6@$Co_3V_2O_8$/graphene	3D microlattice	V_2O_5, $Co(Ac)_2{\cdot}4H_2O$, $Zn(CH_3COO)_2{\cdot}6H_2O$, NH_4VO_3, GO	3D extrusion	Vacuum	Supercapacitor	260
Graphene	3D scaffold	Graphene, EGB, DBP, PVB, ET	3D extrusion	Ambient	Sensor	232
Graphene	3D lattice	GO, EDA	3D template	Freeze	Sensor	243
Graphene	3D honeycomb	GO, water	3D template	Freeze	Stretchable display	245
Graphene-$LiFePO_4$, -$Li_4Ti_5O_{12}$	3D electrode	GO, $LiFePO_4$, $Li_4Ti_5O_{12}$, Al_2O_3	3D extrusion	Freeze	Lithium-ion battery	261
Polyaniline/r-GO	3D electrode	Graphite, polyaniline, NMP	3D extrusion	—	Supercapacitor	248
Graphene	3D lattice	$LiClO_4$, propylene carbonate, GO	3D extrusion	—	Supercapacitor	262
GO	3D microlattice	GO, $CaCl_2$	3D extrusion	Freeze	Supercapacitor	41
GO	3D electrode	Graphite	3D extrusion	Freeze	Microsupercapacitor	263
Graphene	3D complex architecture	Graphite, Ag NPs, CNT, MoS_2	3D extrusion	Freeze	Microsupercapacitor	186
Graphene	3D truss architecture	GO, acrylic photopolymers, BisA-EDMA, PEGDA700	3D PmSLA	Supercritical or freeze	Energy storage	244
Graphene	3D lattice	GO, HPMC, water	3D extrusion	Freeze	Supercapacitor	237
$Ni_{0.33}Co_{0.66}S_2$/graphene	3D architecture	Sodium alginate, GO, $Ni_{0.33}Co_{0.66}(OH)_2{\cdot}xH_2O$	3D extrusion	Freeze	Energy storage	249
MoS_2-Graphene	3D electrode	Ammonium thiomolybdate, GO	Inkjet	Freeze	Sodium-ion battery	242
Graphene-CeZrLa oxide	3D catalytic reactors	CeZrLa, CeZrLa/GO nanocomposites	3D extrusion	Ambient	Nanocatalyst	247
g-C_3N_4-sodium alginate	3D patterned membrane	g-C_3N_4, Pluronic F127, sodium alginate	3D extrusion	Supercritical	Solar wastewater remediation	183
Graphene	3D scaffold	Graphene, DNa, PEG, PEI, water	3D extrusion	Ambient	Energy storage	239
r-GO	3D framework	GO, $Na_3V_2(PO_4)_3$, water	3D extrusion	Freeze	Sodium-ion battery	264

preparation of SiO_2[184] and alginate[209] aerogel microspheres. An example of inkjet printing for aerogel microsphere fabrication is shown in Fig. 8. In this case, the authors used a commercial inkjet printer to print SiO_2 alcosol suspensions into a vegetable oil bath containing a base catalyst.[184] The sol microdroplets then become gels whose diameters can be controlled from 0.1 to 4 μm range. Using a similar method, alginate aerogel microspheres have been produced with a particle-size distribution of 23.8 ± 4.5 μm.[209]

Compared to the previous emulsion-gelation[111,158] or dropwise extrusion[40,253–255] methods, inkjet printing of aerogel microspheres holds two advantages. First, it is a widely applicable and versatile technique, allowing precise control over microsphere dimensions. As long as the viscosity and the surface tension of the ink are kept to a suitably low range, inkjet printing can be used reliably. Although printings of only SiO_2 and alginate aerogels have thus far been reported, we believe that other aerogel types can also be printed using this method in the near future. Second, due to the nature of the inkjet printing nozzle, the controllability of drop volume ensures small and highly repeatable microsphere diameter. This is not possible using the conventional dropwise extrusion approach.

4.2.2 Printing aerogel thin-films or patterns. The inherent structural weakness of aerogels arising from nanostructured connections makes it challenging to pattern them using

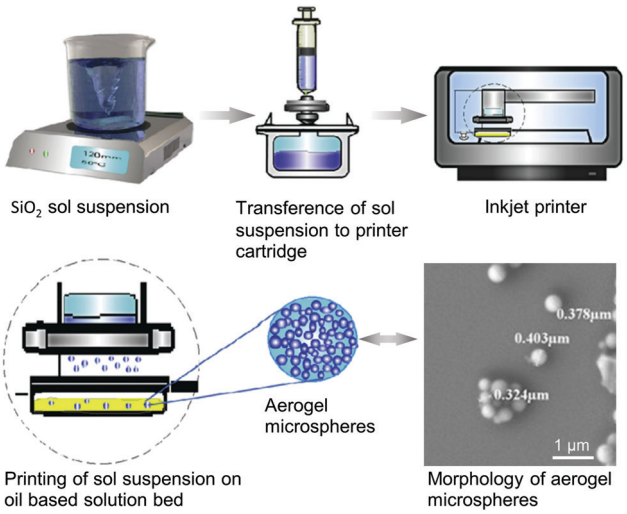

Fig. 8 Inkjet printing process of SiO_2 aerogel microspheres. Adapted with permission from ref. 184. Copyright 2015 Elsevier B.V.

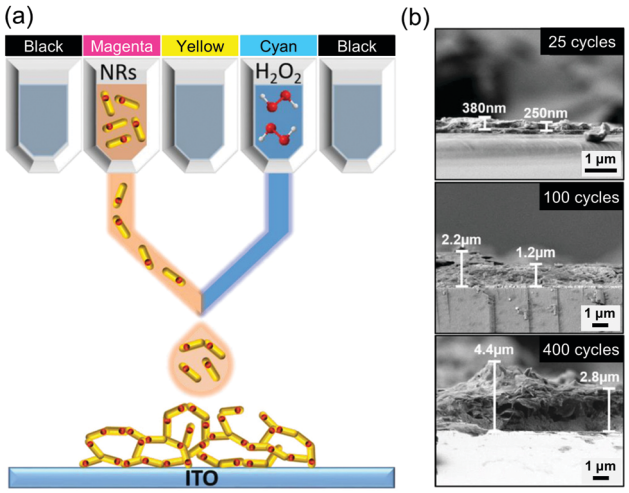

Fig. 9 (a) Schematic of inkjet printing of semiconductor nanoparticle-based aerogels on conducting electrodes. (b) SEM images of the cross-section view of different printing cycles. Adapted with permission from ref. 182. Copyright 2019 WILEY-VCH.

traditional preparation methods. Recent advances in printing aerogel thin-films or patterns using inkjet and screen printing now enable direct deposition of the desired pattern and thickness of aerogels on a wide variety of target substrates.

Inkjet printing. The aerogel microspheres in the above section are very special application examples of the inkjet printing method. The prevalent application of graphics and functional inkjet lies in creating thin-film patterns of pigments or functional materials on a wide variety of substrates, including paper, glass, and silicon wafer.

When inkjet printing sols or inks in a membrane, the gelation process usually occurs in the ambient atmosphere, and is accompanied by a process of volatilization and shrinkage of the sols. Therefore, it is challenging to control the gelation rate of the inks and the structural shape and integrity of the printed aerogels. Thus far, printings of SiO_2,[211] carbon,[213] and semiconductor[182] aerogel films or patterns have been demonstrated from 0D nanoparticle-based inks. For example, using an ink formulation with activated carbon aerogel (ACA) nanoparticles, solvent, and conductive poly(3,4-ethylenedioxythiophene) (PEDOT) binders, layers of porous conductive composites have been directly printed on a membrane using a drop-on-demand inkjet printer.[213] This particular printing process does not involve a chemical reaction. The use of binder allows for uniform patterning, with good control over the thickness per print repetition.

For sols or inks that are gelled by chemical reactions, it is challenging to keep a low enough and stable viscosity to achieve a suitable *Z* value for reliable drop on demand inkjet printing. To address this, a gelation approach *via* inkjet printing has been developed by simultaneously printing a semiconductor CdSe/CdS nanorod ink in one cartridge and a destabilization agent H_2O_2 in another,[182] in a commercial colour inkjet printer; Fig. 9a. When printing, the two inks are mixed with a user-specified ratio, and an oxidation reaction of the surface ligands initiated to assemble the nanoparticle network to form gels. As in ref. 213, the thickness of the printed aerogel patterns can be increased with print repetitions; Fig. 9b. Very importantly, this gelation method can be extended to other aerogels from molecule-derived inks where the mixing of two components is carried out during printing. For example, the traditional two-step process of acid–base catalysed SiO_2 gel can be tailored such that the pre-polymerized acid-catalyzed SiO_2 sol precursor is loaded in one ink cartridge and the base catalyst in another. This approach can also address concerns on suitable ink viscosities and ink storage.

Screen printing. Screen printing can be used to create patterns on a wide variety of substrates on a large scale. The thickness of printed film can be controlled in the range of 10 to 100 μm,[192] making it useful for printing solar cells,[265] fuel cells,[192] and electronic devices.[191] Using screen printable inks of aerogel microparticles mixed with binders offers a particularly versatile route towards aerogel thin-film. For example, to improve the photovoltaic performance, TiO_2 and MgO-doped TiO_2 aerogel encapsulated with ethylene vinyl acetate (EVA) coatings can be screen-printed on silicon solar cells (Fig. 10).[185] In this work, the aerogel particles with concentrations of 0.2–0.8 mg mL^{-1} are well distributed as micron-sized blocks within the 9 μm thick coating. A concentration of 15 wt% of EVA, a common binder for screen printable inks, provides the necessary viscosity and strength of the printed film.

4.2.3 Printing 3D architecture aerogels. Compared with aerogel microspheres and 2D patterns, most examples of printed aerogels involve aerogels with 3D architectures. Indeed, it has been one of the most popular fields in aerogel research. There are three main types of 3D printing methods that have thus far been developed for aerogels: light-based printing, 3D extrusion printing, and 3D printed templating (Table 6). This section discusses these printing methods.

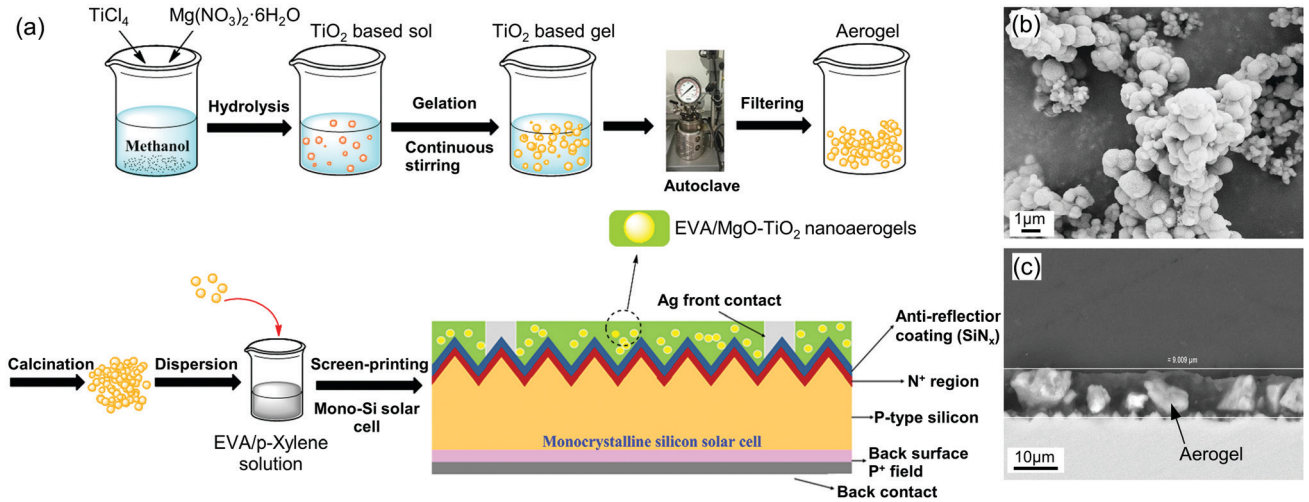

Fig. 10 (a) Screen printing process for MgO-TiO_2 aerogel particles onto the surface of a mono-Si solar cell. (b) SEM image of MgO-doped TiO_2 aerogel. (c) Cross-section SEM image of a solar cell after coating with EVA/MgO-TiO_2. Adapted with permission from ref. 185. Copyright 2018 John Wiley & Sons, Ltd.

Light-based printing. Based on photopolymerization, there are two main types of light-based 3D printing: SLA and DLP.[210]

SLA printing technology uses an ultraviolet laser as the light source. A lens system is used to control the scanning of the laser spot on the top surface of the liquid resin. When this layer is photopolymerized by the laser, the sample holding platform drops a certain distance (usually in the range of 25 to 100 μm).[210] The cured layer therefore is immersed in liquid resin, and the surface of the liquid resin is scanned and photopolymerized again to create the subsequent layer. This process is repeated until a complete 3D structure is obtained.

DLP printing technology first uses the slicing software to cut the model into slices, and uses a projector to project the sliced image, usually from the bottom of a transparent container into the photocurable resin pool, so that photopolymerization occurs in a very thin resin layer. The sample holding platform then moves up by one layer's distance, and the projector projects the next sliced image and cures the layer. The cycle continues until a 3D printed object is created.

The differences between these two technologies are: The light source of SLA is a laser while for DLP it is a projector. Also, the resin curing of SLA is from spot to line, and then line to

Table 6 3D printing processes for aerogels categorized by curing or gelation methods

Curing or gelation methods	Description	Advantages	Disadvantages
Light-based printing	Using photo-curable resin to cure layer by layer to form a 3D structure by ultraviolet or visible light in the presence of a photoinitiator. Printing aerogel accuracy: 10 μm.[244]	Compatible with traditional molecule-derived sols.	Precursor sols must be compatible with photo-curable resins, initiators, *etc.*
		Usually short curing time and relatively high efficiency. High printing accuracy.	The solution needs to be transparent to the light.
Extrusion-based printing	Preparing the ink with appropriate viscosity firstly, and form the required 3D structure layer by layer by means of nozzle extrusion. Printing aerogel accuracy: 100–400 μm.[19,260]	Various shapes printable.	Requirements for specific ink viscosity.
		Suitable for non-molecular-based inks.	Need some curing measures.
		Low equipment cost.	Diameter of nozzles always above 100 microns, print accuracy is not fine enough. Inefficient for mass printing.
3D printed templating	Using 3D printed resin as a template or mould. After injecting sol, the template is removed by dissolution or pyrolysis to form a 3D structure. Aerogel size accuracy: 200 μm.[243]	Suitable for traditional molecule-derived sols.	Limited to the fluidity of sol or ink, fine structure is difficult to achieve.
			Need to remove template.
		No special requirements for sol control.	Limited to low viscosity sols or inks.

layer and eventually to object. On the other hand, for DLP, it is from layer to object.

For printing aerogels, light-based 3D printing methods always use a mixture of photo-curable resin and a pre-polymerized sol as precursors. In the presence of a photoinitiator, light with a specific wavelength and intensity is used to focus on the surface of the mixture, to complete the curing/drawing operation. The main challenge is the development of a photocurable resin that has a (i) short curing time to shorten the printing time, and (ii) low enough viscosity to ensure quick reflowing and filling so that the next layer can be printed.[244]

For traditional SLA or DLP printing of polymers, the inks are always composed of a photocurable resin (monomers and oligomers) and a photoinitiator. However, light-based 3D printing of molecule-derived oxide aerogels poses additional challenges. Taking SiO_2 aerogel as an example, polymerization of the photocurable resin alone without that of photocurable SiO_2 precursor can lead to discontinuous chemical structures or even print failure. It is therefore important to introduce a hybrid SiO_2 precursor containing siloxane groups (Si–O–R) and acrylate groups, which can support both the hydrolysis-polycondensation reaction and photopolymerization reaction. Two such hybrid precursors, TMSM[205,208] and APTMS,[206] have been demonstrated for successful printing of SiO_2 sols. The typical molecular structure and chemical reaction for APTMS when used as a hybrid precursor are shown in Fig. 7b.[206] The light wavelengths that are used to initiate the photopolymerization are either in the visible green (λ = 532 nm),[205,208] or UV (λ = 385 or 405 nm) region.[244,266] In the first demonstration of printed aerogels by SLA in 2015, 3D letter-shaped aerogels were fabricated using a template with hollow letters as a mask (Fig. 11a–c).[205] The light-induced instantaneous gelation spreads and completes within a few seconds in the entire illuminated area. It is suggested that the rapid gelation is due to the polymerization that releases heat and increases the local temperature, accelerating the gelation without any direct heating from the laser beam. In 2018, SiO_2 aerogels with a 3D complex shape (Fig. 11d–f) were fabricated through light-based printing[206] using a commercial DLP 3D printer. In this demonstration, each gel layer with a thickness of 200–400 μm can be completely cured within 2–5 s.

In addition to the above, direct production of aerogel-polymer composites can also be realised using light-based printing. By adjusting the catalysts, the siloxane groups of the hybrid precursors can be hydrolysed-condensed first to form a gel. The gel can be then exposed to a laser in a hexagonal pattern to completely penetrate the entire gel, initiating photopolymerization reaction to form a polymer.[266] After solvent exchange and supercritical drying, a SiO_2 aerogel composite, composed of an *in situ* formed honeycomb wall of polymer (which is exposed to the laser) and hexagonal aerogel filler can be obtained (Fig. 11g–i).[266]

Besides molecule-derived SiO_2 aerogels, PmSLA has also been used to print 3D GO and polyethylene glycol diacrylate (PEGDA)/CNF aerogels.[22,244] For the GO aerogels,[244] the authors used GO flakes with photocurable acrylates (bisphenol A ethoxylate dimethacrylate, and PEGDA) and photoinitiator. This reported PmSLA technique (Fig. 12) can achieve a resolution down to 10 μm to form more intricate structures than previously reported methods.[244]

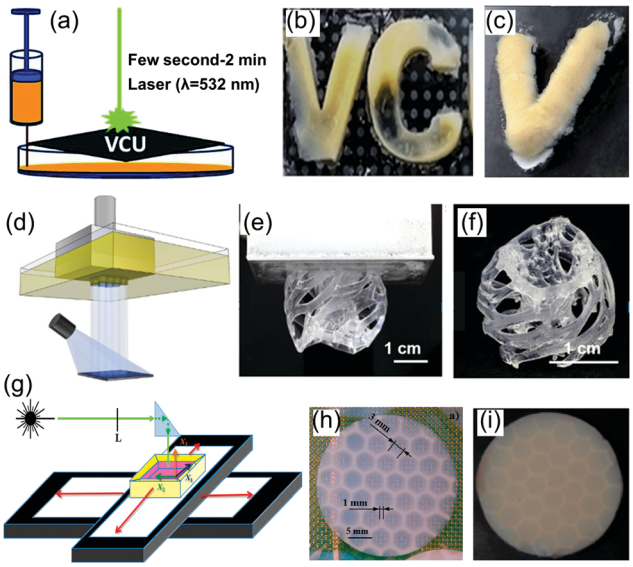

Fig. 11 Schematic diagrams and photographs of light-based 3D printing processes for SiO_2 aerogels. (a) Schematic diagram of a laser-based printing process with a mask, (b) wet-gel letters, and (c) dried aerogel letter "V". (a-c) Adapted from ref. 205 with permission from the Royal Society of Chemistry. (d) Schematic diagram of a DLP printing process, (e) wet 3D gel after DLP printing, and (f) dried 3D aerogel structure after solvent removal. (d–f) Reproduced with permission from ref. 206. Copyright 2018 American Chemical Society. (g) Schematic diagram of the setup used to fabricate a honeycomb pattern of cross-linked aerogel, (h) digital photo of the alcogel, and (i) dried honeycomb aerogel composite. (g–i) Adapted with permission from ref. 266. Copyright 2018 American Chemical Society.

Extrusion-based printing. Extrusion-based 3D printing of aerogels can be achieved by automated movement of extrusion nozzles which have a typical inner diameter of several hundred microns. Extrusion can be enabled by pneumatic pressure *via* air-powered fluid dispensers, with the air pressure and the writing speed being the key parameters for successful 3D printing. For aerogel printing, extrusion-based 3D printing is the most versatile method. It can be widely used in both molecule-derived and nanomaterial-based inks, as long as the rheology of the inks is adjusted to a suitable range.

The resolution of the printed structures largely depends on the movement precision of the nozzle or the sample holding platform. For extrusion-based 3D printing, the main challenges are: (i) to achieve uniform dispersion of each component in the ink,[186,233,239,249] (ii) to adjust the rheological properties of the ink not only with shear-thinning behaviour for reliable extrusion, but also with enough viscoelasticity to self-support and retain the shape immediately after printing,[18,186,231,232,240,249] and (iii) to control/maintain the nanostructures of the gels through adjustment of chemical compositions on the basis of meeting the rheological requirements for printing.[19]

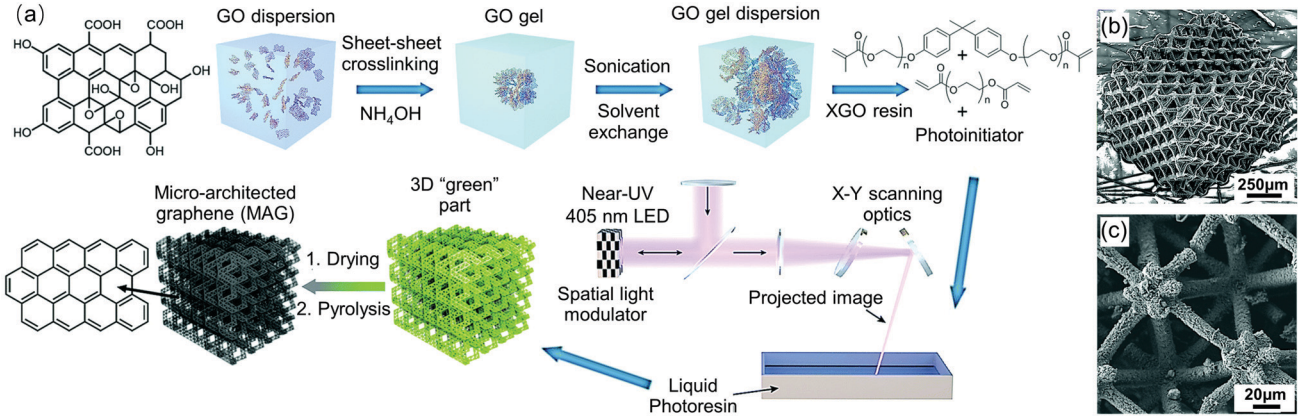

Fig. 12 Fabrication of PmSLA printed graphene aerogels using photo-activated GO resin. (a) Schematic illustration of a synthesis process of micro-architectured graphene (MAG). (b) and (c) SEM images of crosslinked GO particle (XGO)-derived MAG. Adapted from ref. 244 with permission from the Royal Society of Chemistry.

Based on the curing method, extrusion-based 3D printing can be divided into three categories: (i) Direct ink writing without curing or additive agent. For this, the ink consists of nano-materials and solvents only. No curing agent or additive is included. This ink usually has a high enough viscosity. (ii) Gelation or thickening with cross-linking or gelating agent which increases the ink viscosity, allowing it to self-support and maintain the printed shape after the deposition. (iii) Curing by freeze-casting. In this strategy, cooling is applied to solidify the printed slurry immediately after deposition, stopping the liquid flow to maintain the printed shape. Selected examples of the print parameters for extrusion-based 3D printed aerogels are summarized in Table 7. Below we discuss these abovementioned extrusion strategies in more detail.

(i) For direct ink writing without curing or additive agent, it is possible to reach the desired rheological properties through direct mixing of nanomaterials with solvents. This is typically achieved by exploiting the hydrogen bonding interaction on the surface of the nanomaterials. This ink can be printed directly in the air at room temperature. The deposited material can support itself and retain the printed shape without additional curing measures (Fig. 13). Using a single or multiple nanomaterial, such as graphene,[257,259] GO-,[216,235,256,263] and CNF-based,[227,230] and a mix of 1D nanofibre and 2D nanosheet materials, inks have been formulated without any additives. These inks have been demonstrated to be directly 3D-printable for aerogel fabrication.

The printability of these inks largely depends on the solid content which governs their rheological properties. For GO aqueous inks from exfoliated layers, <5 mg mL^{-1} concentration is generally unsuitable for 3D extrusion printing due to low viscosity.[18] Experimentally, the demonstrated concentration range of such dispersions to be printable is in the range of 5 to 50 mg mL^{-1}.[235,256,259,263] To avoid the use of a large amount of solvent or surfactants prevalent in the conventional liquid phase exfoliation method of 2D materials,[267–269] and maintain the stability of high-concentration graphene inks against sedimentation, an alkaline solution with a pH of 14 was used.[257] This increased the viscosity of the slurry by two orders of magnitude compared to that with a pH of 7. Using this strategy, the authors could maintain a slurry concentration of up to 50 mg mL^{-1} for a prolonged period.[257]

The obvious advantage of this additive-free ink is that it does not require any subsequent impurity removal process. However, the disadvantage that comes with this approach is that the viscosity of the ink is primarily determined by the concentration of the nanomaterials. This limits the manoeuvrability with material concentration and performance adjustment of the resultant structure, such as the density, mechanical strength, and electrical or thermal conductivity.

(ii) Ink viscosity can be better adjusted through gelation or thickening with other cross-linking or gelating agents. This adaptability allows the printing of a wider range of aerogel types, in particular, those that are difficult to extrude, such as molecule-derived SiO_2[179,207] and RF sol[19] with low-viscosity, or 1D nanofibre CNCs[181] and metal nanowires[217] with a low number of reactive sites. Based on whether the additive chemically reacts with the original sol or ink, these additives can be further divided into three types: cross-linker, gelation catalyst, and thickener.

Chemical cross-linking agents form stable covalent bonds with the precursor or nanomaterials through chemical reactions, thereby increasing the viscosity of the sol or ink and the mechanical strength of the gel after printing. Generally, the formed chemical structure is retained in the final aerogel, and becomes a part of the aerogel's 3D network. Examples of cross-linking agents include silk fibroin biopolymers,[207] RF,[18] Kymene,[176,181] acrylamide (AAm) and *N*,*N*′-methylenebis-(acrylamide) (MBAA) with post-printing UV-gelation.[229] Examples of aerogels printed using these agents include SiO_2,[207] GO,[18] CNC,[181,229] and CNF.[176]

The gelation catalyst mainly changes the electric double layer balance of the system by catalysing the reaction or adjusting the pH value, so that the system undergoes cross-linking for gel curing. Although after this process most of the gelation catalysts generally remain in the pore solvent, a small

Table 7 Printing parameters for extrusion-based 3D printed aerogels

Curing or gelation methods	Main composition of the inks	Concentration mg mL^{-1}	Viscosity Pa s	Substrate	Printing environment	Nozzle diameters μm	Moving speed mm s^{-1}	Ref.
Direct ink writing without curing or additives	GO + water	5–25	—	—	Air	200	3.5	235
	GO + water	17.5–50	2×10^2–2×10^3	Glass	Air	108–210	1–8	263
	Graphene + water	80–230	8×10^3	—	Air	200–600	—	257
	GO + water	15	—	PET	Air	200	—	259
	GO + water	20	—	PET	Air	200	—	171
	Large GO + water	20	1.4×10^4	—	Air	400	10	256
	CNT/GO, GO/CNF + water	180, 90	3×10^3	—	Air	305	—	216
	CNF + water	5–21	1×10^3–2×10^3	Plastic	Air	410–840	5–12	230
	CNF + water, $CaCl_2$ bath	20	2.7×10^5	Glass	Air	300	5	227
Cross-linking or gelating agent or thickening	SiO_2 sol, aerogel particle, PPGNH + 1-pentanol	—	1×10^3–2×10^5	Glass	Air	100–1190	12–18.4	179
	SiO_2-SF sol + water	112, 126	—	Silicone	Air	838	10	207
	RF, Na_2CO_3 + water	164	6×10^4	—	Air	410	30–150	180
	RF, cellulose, SiO_2 + water	349	2×10^4	Glass	Isooctane	100–400	3	19
	CNC, Kymene, + water	118–300	—	—	Air	200–500	2	181
	Ag nanowire, GO + water	187.5	8×10^4	PET	Air	110–500	4–10	217
	GO, fumed SiO_2 + water	156.7	2.3×10^3	Silicon	Isooctane	250	—	18
	Polyaniline, GO + NMP/water	17.6–20.9	6×10^2–3×10^3	Polystyrene	Air	400–600	—	248
	T-CNF, Kymene + water	28.6	6×10^2	—	Air	800	10	176
	CNF, alginate, $CaCl_2$ + water	10–14	5×10^4–3×10^5	Glass	Air	580	2	225
	CNF, alginate, $CaCl_2$, water	19.5	—	—	Air	410	—	226
	GO, EDA + water	10	—	—	Air	—	Inkjet	238
	GO, $CaCl_2$ + water	20.1	1×10^5	Glass	Air	100–400	4–10	41
	GO, $CaCl_2$ + water	20	—	Glass	Air	250	4–6	236
	CNT/GO, $CaCl_2$ + water	10	8×10^4	Glass	Air	250	4–6	258
	GO, ascorbic acid + water	—	7×10^3	Glass	Air	400	4–20	107
	GO, GNP, SiO_2, RF + water	284.6	2.4×10^3	Silicon	Isooctane	250	—	20
	GO, HPMC + water	90	—	Glass	Air	400	3	21
	GO, HPMC + water	90	—	Glass	Air	400	5	237
	GNP, EGB, DBP, PVB + ethanol	200	1×10^3	—	Air	300–500	5–15	232
	GO, HMPC, Pluronic F127, $(NH_4)_2CO_3$ + water	40	1×10^3	—	Air	250	—	234
	CeZrLa/GO, methyl cellulose + water	—	—	—	Air	400–800	33	247
	GO, NCOH, SA + water	50	4×10^4	—	Air	—	5	249
	Graphene, Pluronic F127, Cu + water	25–60	—	Graphite	Air	100–1000	6–12	231
	Graphene, DNa, PEG, PEI + water	366	5×10^3	Al_2O_3	Air	400	—	239
	CNF, Cellulose + water	112.5	2×10^6–6×10^6	PET	Air	840	—	228
	CNC, Au, AAm, MBAA + water	254	—	Glass	Air	500	1.6	229
	g-C_3N_4, Au, SA + water	90	3×10^4	Glass	Glycerol–$CaCl_2$	50–80	3–6	183
Freezing	Graphene, rGO, CNT + Phenol or camphene	2–100	—	—	Air	159	—	178
	Cellulose, NMMO + water	50	—	—	Air	413	—	219
	CNC, xyloglucan + water	40	30–2000	Cu plate	−3 °C to 1 °C	838	3	220
	Aramid, KOH + DMSO	20	1×10^2–4×10^2	Cold plate	−10 °C	330	14	223
	Ag nanowire, PVA + water	10	—	Cold plate	−30 °C	120	Inkjet	54
	GO + water	10	—	Cold plate	−25 °C	—	Inkjet	109
	GO + water	—	—	Cold plate	−25 °C	—	Inkjet	241
	ATM, GO + water	46	—	Nickel foam	−30 °C	—	Inkjet	242

amount still exists in the solid skeleton of the gel network. Subsequent processes such as washing or drying can remove it. For example, when printing GO-based inks, a trace amount (15 mmol L^{-1}) of calcium chloride can be used as a gelation catalyst,[41,236,258] increasing the storage modulus from 3500 Pa to 60 000 Pa and the yield stress from 40 Pa to 160 Pa, improving the printability and self-supporting property of the ink.[41]

Thickeners, also known as viscosifiers, usually have high molecular weights (organic) or high surface area (inorganic), and can be used to increase the viscosity or storage modulus, and thus the printability of these inks. Generally, they do not chemically react with the gel network and only change the physical properties of the ink. A range of organic (such as hydroxypropyl methyl cellulose,[19,21,237] PPGNH,[179] and methyl cellulose[247]) or inorganic materials (including fumed SiO_2[18–20] and nanoclay[270]) have been used as thickeners. In particular, fumed SiO_2 has been used to prepare GO-[18] and RF-based inks[19] for extrusion 3D printing. Adding ~10 wt% SiO_2 to the inks could increase the storage modulus and yield stress by an order of magnitude,[19] improving the extrusion printability of the inks. We note that the thickeners used in this example remain in the gel network skeleton. Subsequent steps such as high-temperature annealing or etching are required to remove them.

Recently, based on a similar method, a breakthrough on printing pure SiO_2, polymer-reinforced SiO_2, or SiO_2–MnO_2

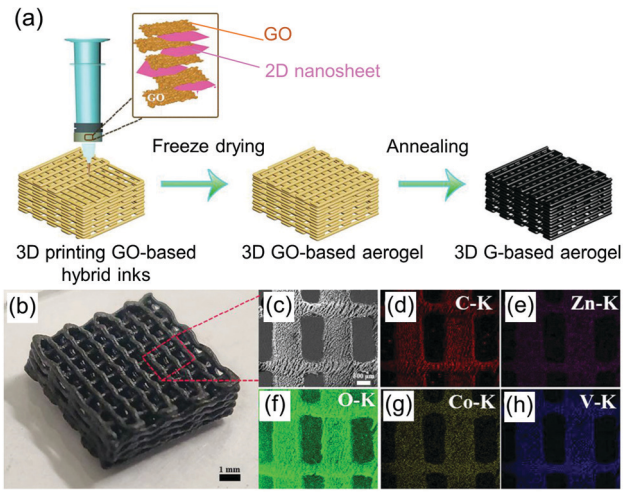

Fig. 13 (a) Schematic illustration of 3D printing of a graphene-based aerogel electrode. (b) Photographs of as-prepared G/ZnV_2O_6@$Co_3V_2O_8$ aerogel. (c) SEM image. (d–h) Corresponding EDS mapping images. Adapted with permission from ref. 260. Copyright 2019 WILEY-VCH.

aerogel objects was achieved.[179] The authors demonstrated 3D extrusion of hybrid molecule-(ethyl silicate) and nanomaterial-derived (SiO_2 aerogels) inks, coupled with an ammonia vapour post-treatment (Fig. 14),[179] followed by solvent exchange and drying to solidify the printed structures. Here, SiO_2 aerogel introduced to the ink formulation not only acts as a thickener in the ink, but also as the skeleton in the final printed structure.

(iii) For the case of freeze casting, the printing is carried out on a plate or environment at a temperature lower than the freezing point of the ink solvent. This ensures that the printed material is rapidly cooled and solidified immediately after deposition to retain the original shape. In addition to the conventional extrusion,[178,219,220,223] 3D drop-on-demand inkjet printing can also be combined with freeze-curing,[54,109,241,242] where overhanging structures using a multi-nozzle system can be achieved. For this, water can be loaded in one of the nozzles to print "blank" ice as a temporary support.[109] This strategy can also be divided into low-temperature- and room temperature freeze-curing.

For the case of low-temperature freeze-curing, water is used as the ink solvent (Fig. 15). The temperature of the cold plate is generally set from −30 °C to −25 °C when using 3D drop-on-demand inkjet printing.[54,109,241,242] The newly deposited droplets make successive thin layers at the top of the previously printed layer, which usually melts and re-solidifies. Therefore, the different layers adhere well with each other without creating an interface. Using this method, graphene,[109] MnO_2-graphene,[241] MoS_2-graphene,[242] and Ag nanowire[54] 3D aerogels have been printed on ice supports or Cu plates. DMSO has also been used as the solvent for aramid nanofibre-based inks. Since the freezing temperature of DMSO (18.5 °C) is higher than that of water, the cold plate can be set at −10 °C to ensure fast-enough casting.[223] When 3D printing CNC aerogels by the extrusion method,[220] the ambient temperature can be set between −3 °C and 1 °C. This temperature ensures that the top two printed layers do not freeze, ensuring good adhesion between all the printed layers.

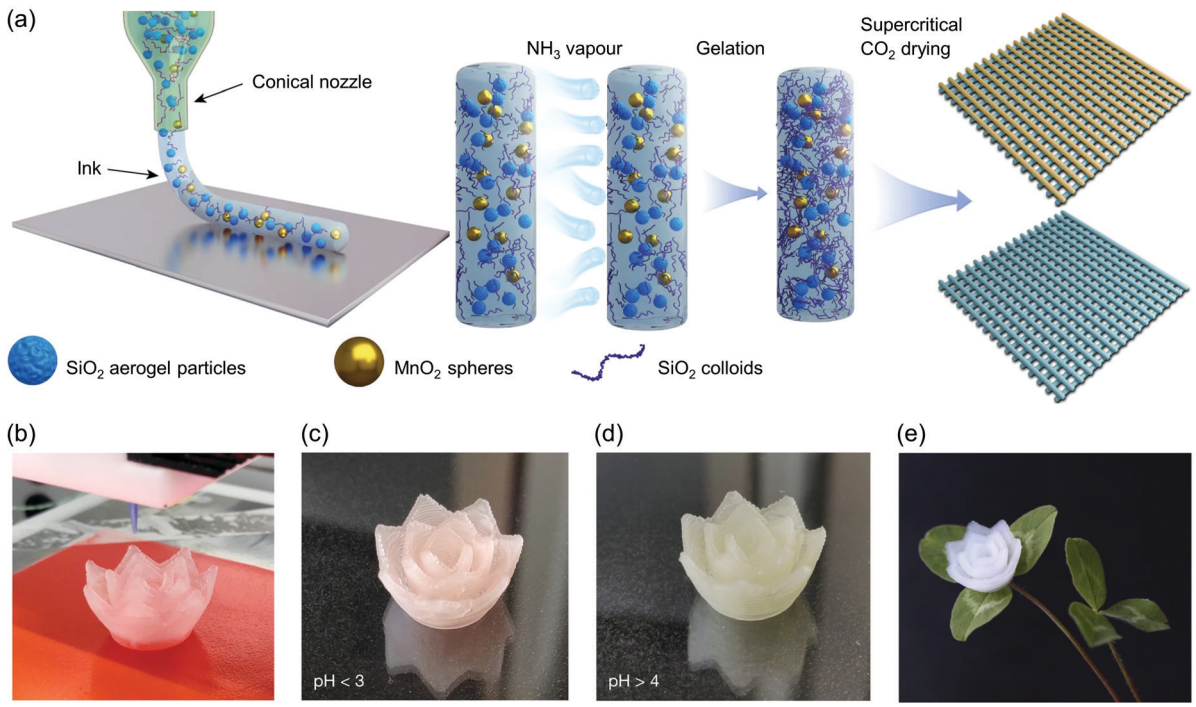

Fig. 14 Extrusion-printed pure SiO_2 or SiO_2–MnO_2 aerogels from inks with thickeners. (a) Schematic diagram of the 3D printing process, (b) 3D printed lotus flower of SiO_2 gel using 38 layers. Photographs of the hydrogel (c) before solidification, (d) after ammonia-vapour-induced gelation and (e) after drying. Reproduced with permission from ref. 179. Copyright 2020 Springer Nature.

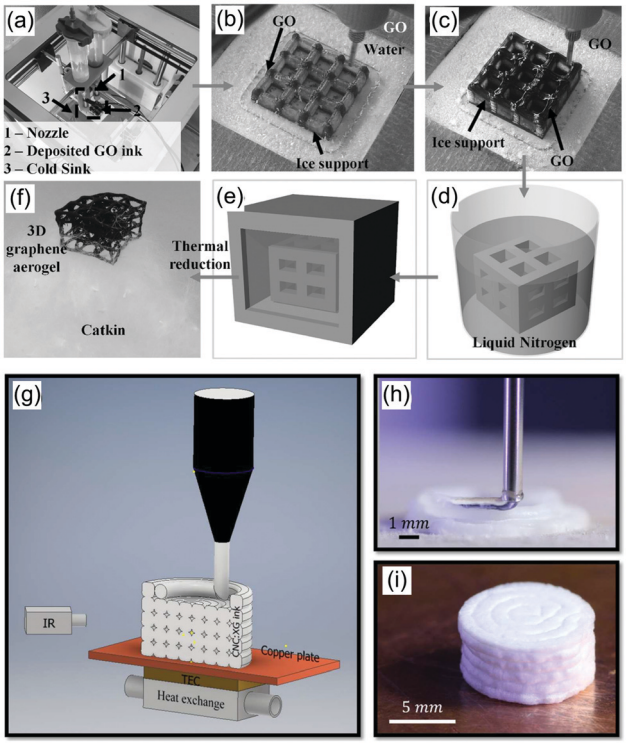

Fig. 15 3D printing of GO-based gels and CNC gels cured by the low temperature freezing method. (a) 3D printing setup of GO-based gels. (b) 3D printed ice support. (c) 3D printed GO suspension. (d) Immersed printed ice structure into liquid nitrogen. (e) Freeze drying. (f) 3D ultralight graphene aerogel obtained by thermal reduction. (a–f) Reproduced with permission from ref. 109. Copyright 2016 WILEY-VCH. (g) Schematic illustration of the printing setup of CNC gels on a cold Cu plate, (h) photograph of the printing process, and (i) the final CNC aerogel. (g–i) Reproduced from ref. 220. Published by MDPI.

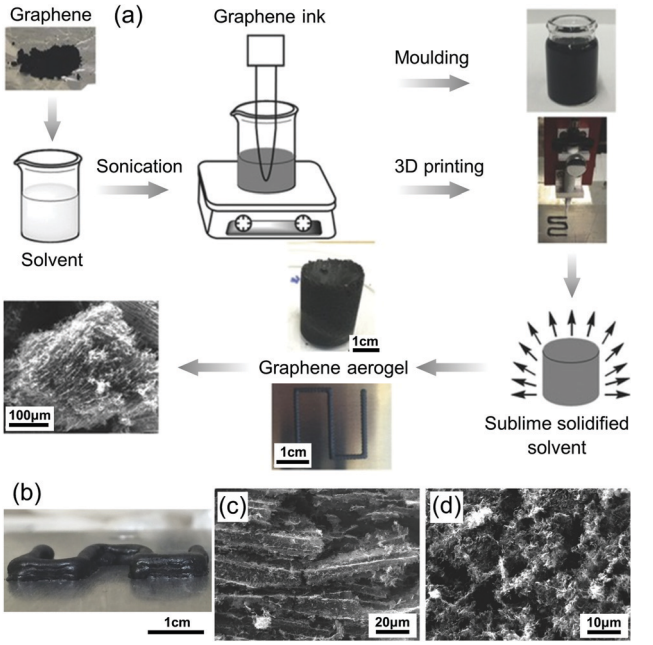

Fig. 16 Printed graphene aerogels prepared by room temperature freeze gelation (RTFG). (a) Schematic illustration of the RTFG process. (b) Photograph of a three-layer thick graphene aerogel using phenol as a solvent. SEM images of graphene aerogels produced (c) in phenol and (d) in camphene. Reproduced from ref. 178. Published by WILEY-VCH.

A simple room temperature freeze-curing method was first reported to fabricate printed aerogels,[178] using solvents that are solid at room temperature, have a high vapor pressure and are prone to sublimation at room temperature. Solvents such as phenol or camphene can be used, where they can be mixed with graphene above their melting temperature (for example, 50–60 °C), and be extruded in the air (Fig. 16). The ink solidifies as it cools to room temperature. Using a similar principle, cellulose/*N*-methylmorpholine-*N*-oxide (NMMO) ink at 70 °C could be 3D printed through extrusion, to obtain self-supported 3D cellulose gel.[219]

The advantage of a freeze-curing method is that because the viscosity is not taken into account, even low viscous Newtonian inks can be 3D printed. This allows printing of ultra-low concentration inks (for examples, <10 mg mL^{-1} or even as low as 2 mg mL^{-1})[54,109,178] for ultra-low density 3D printed materials, with densities as low as 0.5 mg cm^{-3} for 3D graphene aerogel[109] and 1.3 mg cm^{-3} for 3D Ag nanowire aerogel.[54] On the other hand, because of low viscosity, retaining dimensional stability and size accuracy is challenging when using this method.

Aerogels from a 3D printed template. The 3D printed template method uses one of the polymer 3D printing technologies (*e.g.*, SLA) to first print out a 3D polymer mould, leaving the desired aerogel volume empty with connected channels. Sols are then injected into the mould and after gelation, the mould is removed before or after drying, to finally obtain a 3D aerogel. There are two basic requirements for this method: the template should be removable without damaging the structure of the gel or aerogel; the viscosity of the sol is low enough for its complete filling into the tiny channels of the template.

The 3D printing templates that have been reported thus far include hollow polymer architectures by mask-image-projection-based SLA techniques,[243] honeycomb pillar arrays by 3D printing using an acrylonitrile butadiene styrene ink,[245] and hollow mould of high impact polystyrene in an inverse gyroid shape printed by a fused filament fabrication method.[177] The sols or inks that have been demonstrated to fill the templates are traditional polyimide sol,[177] GO/ethylenediamine (EDA) ink,[243] and GO/L-ascorbic acid,[245] which are all liquids with enough fluidity to ensure complete filling. After gelation and drying, the polymer templates could be removed either by demoulding,[245] high temperature pyrolysis,[243] or solvent dissolution,[177] to obtain 3D aerogels[177,243,245] with complex shapes (Fig. 17). Depending on the resolution of the 3D polymer template, the wall thickness of the GO-based aerogel can be as thin as 250 μm.[245]

The advantage of this method is that it can be applied to almost all the traditional sols used in the preparation of aerogels. This is unlike SLA which is only applicable to limited types of aerogels or extrusion printing with limitations in structure and narrow operating time window determined by the fluidity and cross-linking reaction.[177] Furthermore, this 3D

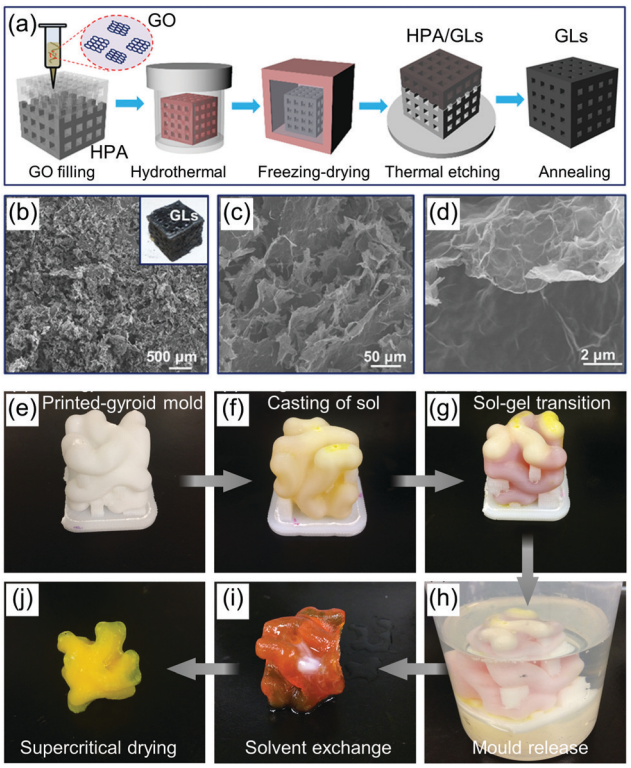

Fig. 17 Fabrication process steps for (a–d) 3D graphene aerogel lattice and (e–j) polyimide aerogel by means of a 3D printed template. (a) Schematic diagram of using a 3D printed polymer mould to fabricate a graphene aerogel lattice through thermal etching. (b and c) SEM images of porous microstructures within the graphene aerogel lattice. (d) SEM image of the multilayer graphene cellular wall with typical wrinkled morphology. (a–d) Reproduced with permission from ref. 243. Copyright 2018 American Chemical Society. (e) Printed gyroid mould for the fabrication of polyimide aerogel, (f) cast sol in mould, (g) sol–gel transition, (h) mould removal process, (i) solvent exchange, and (j) supercritical drying. (e–j) Adapted with permission from ref. 177. Copyright 2019 American Chemical Society.

printed template method can produce more complex structures with desirable resolutions.

4.3 Drying methods

When fabricating a 3D printed aerogel, the next step after printing a static, well-defined gel is 'drying'. This is a very important stage that determines whether a low-density nanoporous aerogel can be obtained. This is because conventional drying in ambient air usually exerts high capillary tension, which destroys the skeleton and induces large volume shrinkage, producing only cracked fragments or dense bulk material. This section discusses the phase change mechanism during drying, the rules for successful drying of aerogels, and three commonly used drying methods.

4.3.1 Rules for successful drying of aerogels. The liquid in the pores of the gel must be replaced with a gas to obtain aerogel. The aim here is to maintain the sizes of the skeleton and pores after this process. If an attempt is made to dry the gel directly in the air by raising the temperature, the magnitude of hydrostatic pressure due to capillary forces (Fig. 18a) arising from the surface tension can be expressed as[271]

$$p_r = \frac{2\gamma \cos\theta}{r} \quad (2)$$

where p_r is the capillary stress, γ is the surface tension of the liquid, θ is the contact angle of the liquid with the pore wall, and r is the radius of the pore.

If the drying process is conducted at atmospheric pressure with pore sizes in the nanometre range, it can be calculated from eqn (2) that the skeletons would experience oblique pulling stresses of ~10 MPa (for a typical aquagel with hydrophilic skeleton and average diameter of 30 nm) as the liquids in the pores are evaporated. Such a large stress compresses the gel continuously during the drying process as the liquid evaporates, causing the gel to gradually shrink and become dense, thwarting the production of low-density aerogels. Additionally, when the pore radiuses on the two sides of a common wall are not equal, eqn (2) dictates that the two sides will be subjected to unequal stresses, causing the pore wall to break (Fig. 18a).[188,272] In this case, only fragments can be obtained. Indeed, the drying process in the air already starts, to some extent, during printing in the ambient air which initiates the shrinkage process. This is why it is a common practice for 3D printing to be carried out directly in liquid baths.[18–20,183]

Therefore, the principles of successful drying to obtain aerogels are to: (i) minimize or (ii) avoid the capillary stress. The minimization route generally follows drying the gel at ambient pressure. This is why it is also called ambient drying. There are two ways to minimize the capillary stress. One is to change the liquid with a solvent with a lower surface tension, *i.e.*, to reduce γ in eqn (2). The second is to modify the chemical state of the pore wall surface with hydrophobic chemical groups to increase the contact angle, *i.e.*, to increase θ in eqn (2). Both measures can reduce the capillary stress p_r, and thus minimize the shrinkage during drying. Furthermore, the capillary stress can be eliminated by avoiding the interfaces between liquid and gas, *i.e.*, to prevent the phase transition from going through the curve connecting C–D–E in Fig. 18b. This can be realized by supercritical or freeze drying by forming a homogeneous supercritical fluid or by transforming the liquid–gas interfaces to solid–gas interfaces, respectively.

4.3.2 Freeze, ambient, and supercritical drying for printed aerogels

Freeze drying. Freeze drying involves freezing the solvent in the gel first, followed by its sublimation into the gaseous stage, under a vacuum environment, commonly realised by continuous operation of a vacuum pump. From the perspective of temperature, phase and vapor pressure changes, the liquid in the gel goes through the liquid–solid phase equilibrium curve connecting C–F–G by freezing to become a solid first, and then through the solid–gas phase equilibrium curve connecting A–B–C by sublimation under vacuum to become a gas (Fig. 18b and c). Though this method can bypass the liquid–gas phase equilibrium curve, avoiding the shrinkage of the gel caused by the capillary stress, it still needs to undergo two

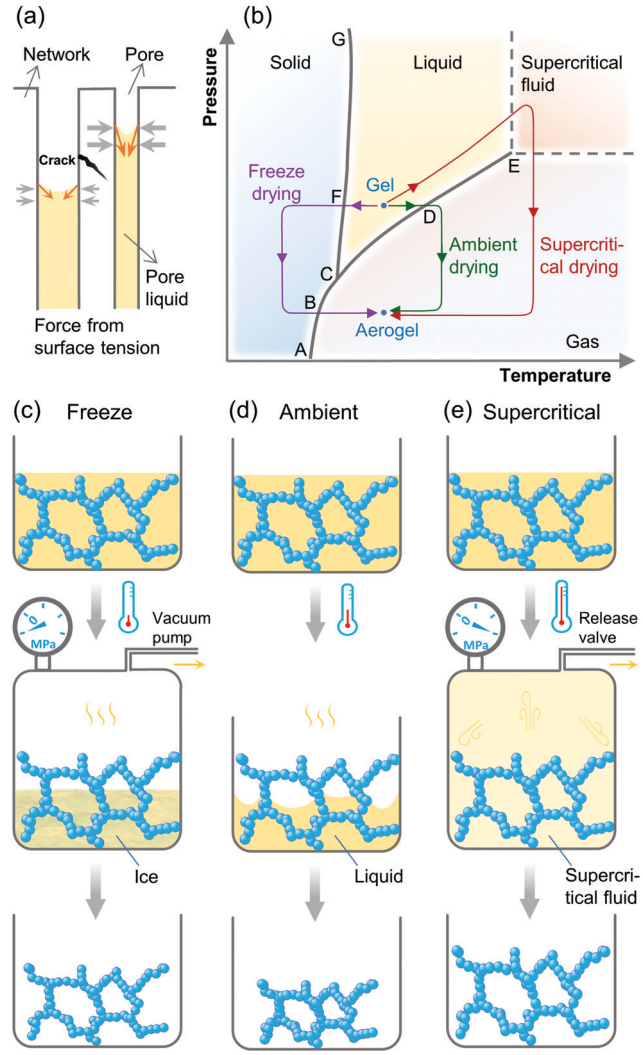

Fig. 18 (a) Capillary forces inducing cracks or shrinkage in the pores of the gels. Adapted with permission from ref. 272. Copyright 1998 Wiley-VCH. (b) Typical phase diagram of solvent in the gel and the pressure–temperature changes in three routes for drying the gels to make aerogels. (c–e) Schematic illustrations of three drying routes (freeze, ambient, and supercritical). Adapted with permission from ref. 27. Copyright 2017 Wiley-VCH.

separate phase transitions (liquid–solid and solid–gas). The latter transition does not affect the gel's nanostructures. However, the liquid–solid transition process always results in a volume change because the densities of solid and liquid phases of the same solvent are typically different. In addition, this may also change the nanopore structure of the gel due to the liquid–solid transition process where solvent (such as water) crystals may grow much larger than the pore size of the gel.[273] Therefore, when this drying method is used on conventional molecule-derived gels with mainly nanometre-size pores, obtaining aerogel monoliths could be challenging. Indeed, in such instances, only powders are usually obtained.[83]

The freeze-drying method is mostly used for drying nanomaterial-based gels, for example, of 0D metal nanoparticles,[62] 1D CNC,[181,220,221] CNF,[22,176,218,228] and Ag nanowires,[54,217] 2D graphene,[231,257] and GO.[241,242,244–246,254,264] Water is the most commonly used solvent. *Tert*-butanol, which has a freezing point (25.7 °C, Table 8) close to room temperature, can also be used as a solvent.[274] To prevent the solvent crystals from growing too large, this process requires a fast cooling rate. This is usually achieved by immersion in liquid nitrogen.[273] In addition, the room-temperature freeze-solidification method that uses high vapor pressure phenol (freezing temperature = 40.5 °C) or camphene (freezing temperature = 51.5 °C) as solvents[178] allows sublimation under ambient conditions without the need for a vacuum unlike conventional freeze drying.

Table 8 Relevant physical properties of commonly used solvents when preparing or drying gels

Solvent	Freezing temperature (°C)	Critical temperature (°C)	Critical pressure (MPa)	Surface tension[a] (mN m^{-1})
CO_2	−78	31	7.3	0.59
H_2O	0	374	22.1	72.0
Methanol	−97	239.4	8.1	22.3
Ethanol	−114.3	243	6.3	21.9
Acetone	−94.9	235	4.7	22.7
Isopropanol	−88.5	235	4.7	21.2
n-Hexane	−89.5	234.7	3.0	17.9
n-Heptane	−90.5	267.3	2.7	19.7
Tert-butanol	25.7	233.2	4.0	20.1

Data collected from ref. 272 and 276–283. [a] At room temperature.

Ambient drying. Ambient drying involves slow evaporation of the solvent in the gel pores at a heating temperature below the boiling point under ambient pressure (Fig. 18d). Water is the most commonly used solvent for inks to print gels, because of its very high surface tension (72.0 mN m^{-1}, Table 8). However, the wet gel or printed structure dried under ambient conditions could exhibit a large linear shrinkage of ≥45%.[217,230,275] Therefore, before drying, to minimize the shrinkage, the gels are always modified with water-repelling chemical groups to increase the contact angle first, then exchanged with lower surface tension solvents such as *n*-hexane[284,285] or *n*-heptane (surface tensions of 17.9 and 19.7 mN m^{-1}, respectively; Table 8).[184] In addition, to control the volatilization rate of the solvent (such that the solvent can volatilize slowly, minimizing the shrinkage), the printed gel is usually placed in a container, leaving only a small hole to vent the vapour.[206] Ambient drying has thus far been used to dry inkjet printed SiO_2 microspheres[184] and CdSe/CdS films,[182] and 3D printed GO-based[247] gels. These gels always have small dimensions which may help the diffusion of solvent from the inside of the structure to the surface. This additionally improves the uniformity of the solvent distribution in the overall structure such that it can be evaporated homogeneously, reducing the shrinkage to some extent.

Supercritical drying. Supercritical drying is the most commonly used method for traditional aerogel preparation. When the temperature and pressure of the liquid exceed the critical point (point E in Fig. 18b), the interface between the liquid phase and the gas phase disappears and becomes a homogeneous fluid. This is also termed as a 'supercritical' fluid,

which fills the entire space, usually in an autoclave. In the absence of a liquid–gas interface, the high-pressure supercritical fluid can be slowly discharged through a pressure relief valve while maintaining the temperature above the critical point, producing an aerogel after releasing the pressure down to ambient and then cooling down to room temperature (Fig. 18e). This process essentially bypasses the liquid–gas phase equilibrium curve connecting C–D–E in Fig. 18b, through a liquid–supercritical–gas phase transition. The critical temperature and critical pressure data for common solvents are shown in Table 8. Based on the critical temperature of the solvent used, this process can be divided into low- and high-temperature supercritical drying.

Low-temperature supercritical drying uses CO_2 as the drying medium which has a relatively low (31 °C) critical temperature (Table 8). The drying temperature of the autoclave is generally set at a mild temperature of 40–90 °C.[209] The high-temperature supercritical drying strategy usually uses alcohol (such as ethanol and isopropanol) as the drying medium. In this case, the critical temperature is always above 230 °C (Table 8), while the drying temperature is set at 260–300 °C. The maximum pressures applied for these two drying methods are typically above 10 MPa.[209] For the case of printed aerogels for supercritical drying, the most common route uses low-temperature supercritical drying of CO_2. Examples of this strategy have been applied to SiO_2-based,[179,207] RF,[19] aramid,[223] alginate,[209] CdSe/CdS,[182] graphene,[18,20,244] and g-C_3N_4-sodium alginate[183] gels. There are also a few examples of SiO_2–polymer aerogels prepared by high-temperature supercritical drying of ethanol.[205,208] However, if the solvent in the printed gel is water, this process needs some modification. The critical temperature and pressure of water are difficult to achieve, and its solubility in supercritical CO_2 fluid is small. Therefore, for both low- and high-temperature supercritical drying, the water in the printed gel needs to be replaced with an organic solvent, which is more CO_2-soluble or has lower critical temperature and pressure, such as ethanol,[209,223] methanol,[207] and acetone.[182]

4.3.3 Comparison of the drying methods. A comparison between the three drying methods is summarized in Table 9. From the perspective of the aerogel pore structure, the shrinkage rate of supercritical drying is the lowest, offering the best preservation of the nanostructures. On the other hand, the shrinkage rate of ambient drying is the largest. From the perspective of cost, the ambient drying appears to be the most economical as no special equipment is needed. Conversely, the cost of supercritical drying is the highest, as expensive high-pressure equipment and a large amount of energy consumption due to heating and cooling are required. In terms of industrial production, ambient pressure drying is the most suitable as aerogels can be continuously produced in an assembly line. While freeze and supercritical drying need vacuum or high-pressure conditions, each drying process requires opening and closing the vacuum or autoclave chamber. They can therefore only be dried in batches.

Based on the process characteristics, the degree of suitability of the drying method is also dependent on the gel types. For example, freeze drying is suitable for the drying of nanomaterial-derived gels,[41,54,62] as the pores of these gels are usually larger. On the other hand, it is not suitable for molecule-derived gels with smaller pores. Likewise, ambient drying is suitable for gels with small dimensions such as inkjet printed microspheres.[184] This is because the small dimension allows easy and complete replacement of the solvent and homogeneous evaporation. Finally, supercritical drying is the most versatile of all, and is suitable for almost all types of gels.

4.4 Post-treatment after drying

The step of post-treatment after the drying process is optional. This mainly involves sintering, chemical reduction, or a wide range of techniques for the removal of impurities. The basic requirement of post-treatments is not to damage the aerogel skeleton and pore structure. Therefore, the process is usually carried out in a controlled gas atmosphere. If a liquid phase is involved, a secondary solvent exchange and subsequent drying process are always required. This section discusses the three major post-treatment processes: heat treatment, chemical reduction, and etching.

4.4.1 Heat treatment. Heat treatment is the most common post-treatment method in aerogel preparation. Based on the effects of heat treatment, they can be divided into the following three categories: (i) Carbonization: Under a high-temperature inert atmosphere, organic aerogels can be converted into carbon aerogels. For example, under nitrogen atmospheres, printed RF aerogels can be carbonized at 1050 °C to form carbon aerogels.[19,20] This process usually results in a large mass loss and volume shrinkage. (ii) Removal of organic impurities by thermal decomposition or oxidation: This process is performed at high temperature in an inert atmosphere (thermal

Table 9 Comparison of three drying routes for printed aerogels

Drying method	Advantages	Disadvantages	Preferable application
Freeze	Moderate cost of equipment Mild conditions	Phase change-induced volume change Pore size expansion effect High energy consumption	Nanomaterial-based gels, specifically those with ultralow densities
Ambient	Simple process No pressure vessel required Continuous production	Large shrinkage Solvent-exchange requires a large amount of solvent	Small size or thin gels
Supercritical	Small shrinkage Best nanostructure preservation	High equipment cost High energy consumption Hidden dangers with high temperature and pressure	Almost all kinds of gels

decomposition) or in the air (oxidation). For example, organic binders in printed hybrid GO aerogels can be removed in an inert atmosphere at 500 °C or in the air at 475 °C.[239,247] (iii) Thermal reduction: This process is usually performed when preparing graphene aerogels, *i.e.*, turning GO into rGO to improve its electrical properties. This reduction method can be achieved purely through thermal reduction or by hydrogen thermal reduction. Pure thermal reduction heats GO-based aerogel to a high temperature of 800–2727 °C in an inert atmosphere,[18,258] to break the oxygen-containing chemical bonds, causing small molecules of water and CO_2 to escape. Hydrogen thermal reduction is based on a pure thermal reduction process but uses 3–10% hydrogen in the flowing inert gas (argon). This way the required temperature can be reduced to 600–900 °C.[186,231,242,261]

4.4.2 Chemical reduction. The chemical reduction process is mainly performed on printed GO aerogels to reduce it to graphene, improving its electrical conductivity. For the chemical reduction of GO, many reducing agents have been explored, including hydrohalic acids, borohydrides, and sulphur- as well as nitrogen-containing reducing agents.[286] These reducing agents can be applied either in gas or in a liquid phase. For example, for gas phase reduction of printed GO aerogels, hydrazine hydrate can be used as a nitrogen-containing reducing agent.[217,263] Examples of liquid-phase reduction reaction of GO include hydroiodic acid in which the aerogel needs to be immersed.[235,248] We note that because the liquid phase reduction reintroduces a solvent, one of the three above-mentioned drying methods must be used afterwards.[235]

4.4.3 Etching. Etching usually uses a corrosive liquid to dissolve impurities through a chemical reaction, followed by washing with solvents (such as water) several times. When formulating inks for printed aerogels, fumed SiO_2 can be added as a viscosity modifier to improve the printability of the ink.[18–20] The SiO_2 is an impurity itself and may affect the final aerogel's intended properties, and therefore, should be removed. The most common approach to achieve this is through etching, which is performed after the carbonization process. This typically involves immersion of the resultant structure in hydrofluoric acid, which reacts with the SiO_2 content on the printed aerogel but does not affect its carbon skeleton. Once the chemical etching is completed, the aerogel is washed several times to remove the impurities. Again, to recover the pure aerogel, one of the three drying processes must be used. This method has been exploited to obtain printed carbon[19] and graphene[18,20] aerogels.

In the above section, we have comprehensively reviewed the technical aspects involved in the whole process of printing aerogels, including raw materials, ink formulation, printing methods, and drying and post-treatment strategies. Research progress in recent years has demonstrated many advantages of printed aerogels, including rich form factors (such as microspheres, films, patterns, and 3D architectures), on-demand shaping/fabrication, and the variety of materials (organic and inorganic aerogels such as nanocellulose, alginate, SiO_2, graphene) that can be printed. In our opinion, these advantages will greatly promote the application of aerogels in conventional as well as new application areas, by overcoming previously unsurmountable obstacles.

5. Applications of printed aerogels

Traditional non-printed aerogels have already demonstrated huge potential for a wide range of applications. The use of printing technology can greatly promote these application opportunities, especially in the field of functional materials that require intricate structures and shaping. Indeed, printing technology offers unparalleled processability and designability on the micron scale, addressing a major weakness of traditional aerogels due to their brittleness and poor structural strength. In particular, printing enabled processability can be used to directly form and readily redesign complex aerogel structures. This makes aerogels significantly more versatile and designable for target applications. Based on the published literature on printed aerogels, we divide this section into six broad technology and application areas of thermal management, energy storage, electronics, chemical, biomedical, and light-harvesting.

5.1 Printed aerogels for thermal management

Thermal insulation materials are widely used in aerospace, petroleum pipelines, industrial furnaces, chemical reactors, cold storage, and buildings. In terms of performance alone, aerogels are widely considered as one of the best thermal insulators because of their ultralow thermal conductivities. Indeed, the conventional SiO_2 aerogel is also currently the most successfully commercialized aerogel product for thermal insulation. However, applications requiring thermal insulations usually demand various shapes, which must be assembled precisely and tightly to achieve effective insulation. The brittleness and difficulty in shaping aerogels therefore put them at a great disadvantage. Printing technologies can address the shaping of aerogel thermal insulations, making materials with fine and complex structures and ability to customize design and production, a reality.

We note that the issue of mechanical reinforcement can be partially addressed using a support structure. For example, a honeycomb polymer reinforcement was *in situ* printed inside a SiO_2 gel using photopolymerization (Fig. 11i).[266] This allowed a well-integrated, high strength SiO_2 aerogel, with a thermal conductivity of 0.0136 W m^{-1} K^{-1}, between that of pure aerogel and pure polymer.[266]

Using inks containing SiO_2 aerogel powder and an organic binder, SiO_2 aerogel thin films with thicknesses of several microns were inkjet-printed for thermal insulations.[211] The printed aerogels keep a relatively low thermal conductivity of 0.05 W m^{-1} K^{-1} in the range of 30 to 300 °C, though higher than that of pure aerogel powders (0.02 W m^{-1} K^{-1}).

Extrusion-printed pure SiO_2[179] and SiO_2–silk fibrion[207] aerogels have also been investigated for thermal insulation. In particular, printed pure SiO_2 aerogel (Fig. 19),[179] demonstrates an ultralow thermal conductivity of 0.0159 W m^{-1} K^{-1}, as low as most

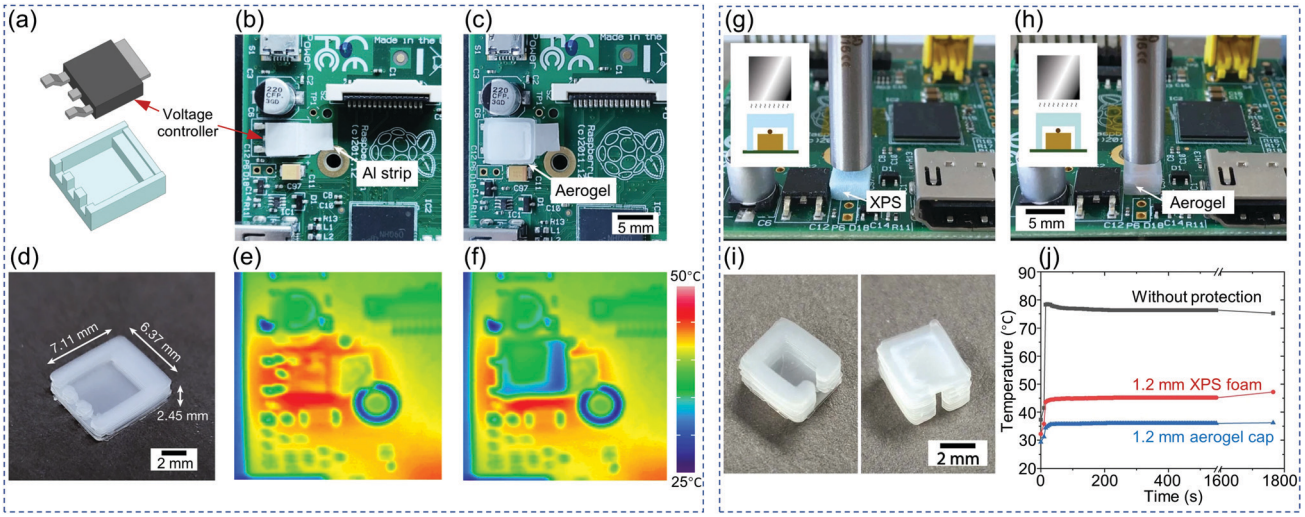

Fig. 19 Performance of 3D-printed SiO_2 aerogels for thermal insulation. (a) Sketch and (d) photograph of a printed aerogel. Photographs (b and c) and corresponding infrared images (e and f) of a circuit board, (b and e) without and (c and f) with the printed aerogel to cover the heat-generating component. Protection of a temperature-sensitive capacitor from a heat source with a (g) polystyrene foam cap (XPS) and (h) printed SiO_2 aerogel cap. (i) 3D-printed aerogel cap. (j) Temperature evolution of the capacitor after contact with the cartridge heater. Adapted with permission from ref. 179. Copyright 2020 Springer Nature.

reported SiO_2 aerogels prepared by traditional sol–gel processes.[287] As pointed out earlier, extrusion printing allows the manufacturing of miniaturized and complex shapes of fragile aerogel objects, which are extremely challenging to make using traditional shaping methods (mould casting and subtractive manufacturing). Very importantly, the printed objects can be applied to small electronic components to ensure a low outer surface temperature (Fig. 19a–f), or to protect temperature-sensitive parts from a nearby heat source (Fig. 19g–j).

5.2 Printed aerogels for energy storage

Due to high specific surface area, good mass transfer ability enabled by the open-pore structure and high electrical conductivity, carbon-based and metal aerogels have great application prospects in the field of energy storage. To fully realize the potential of aerogels in energy storage, two challenges must be overcome: (i) the formation of complex or even curved structures required by batteries or supercapacitors to minimize their volume; (ii) highly connected, direct and unobstructed hierarchical channels to ensure fast and effective mass transfer.[186] 3D printing can address both the above. Indeed, printed aerogels with excellent performance for supercapacitors, lithium batteries, sodium ion batteries, and hybrid energy storage have already been demonstrated, underscoring their huge potential in the field of energy storage.

5.2.1 Supercapacitors. A supercapacitor is a type of energy storage device between traditional capacitors and rechargeable batteries, widely used in power systems and as the starting power source for electric vehicles. The charging and discharging process in a supercapacitor is always a physical process. It therefore has the advantages of long life and wide operating temperature limit. Although a high specific surface area is the most basic requirement for supercapacitor electrode materials, it alone is insufficient for high-performance. This is because electrolytes may not be able to access ultra-micropores and narrow, long micropore channels even though they could contribute to the overall specific area of the electrodes.[288] Therefore, designing the channels of 3D architectures offers means to improve the performance of supercapacitors. Thus far, the demonstrated material platforms for printed aerogel-based supercapacitors have exploited extrusion based 3D printing technology of carbon,[19] graphene,[20,178,231,234] MnO_2 loaded graphene,[21,241] graphene-based hybrid,[186,260] rGO,[41,263] and Ag nanowire[217] aerogels. Typical photographs of printed aerogel supercapacitors or electrodes are shown in Fig. 20a–d, underlining the versatility of printing technology to accommodate arbitrarily shaped devices.

There have been detailed investigations to understand whether 3D printing technology can improve the rate capability of capacitors over non-printed bulk aerogels.[19–21,237] The results show that when ink formulations of the two supercapacitors or electrodes are the same (*i.e.*, the surface area, conductivity, and pore size of the aerogels are the same), 3D printed aerogel electrodes show better specific capacitances, 1.4–12.9 times those of the corresponding non-printed aerogels;[19–21,237] see Table 10 for comparison. The capacitance retention values are also better than those of the capacitors based on non-printed aerogels (Table 10).

The ordered macropores formed between the printed gel filaments improve the penetration of the electrolyte and hence, ion diffusion, resulting in excellent rate capability.[20] Compared with bulk aerogel electrodes with mainly sub-micron or smaller pores, which severely restricts ion diffusion, 3D printed aerogels can be designed to have faster ion diffusion kinetics (Fig. 20e).[186] Additional performance enhancements can be achieved by printing finer aerogel features to further reduce the diffusion length.

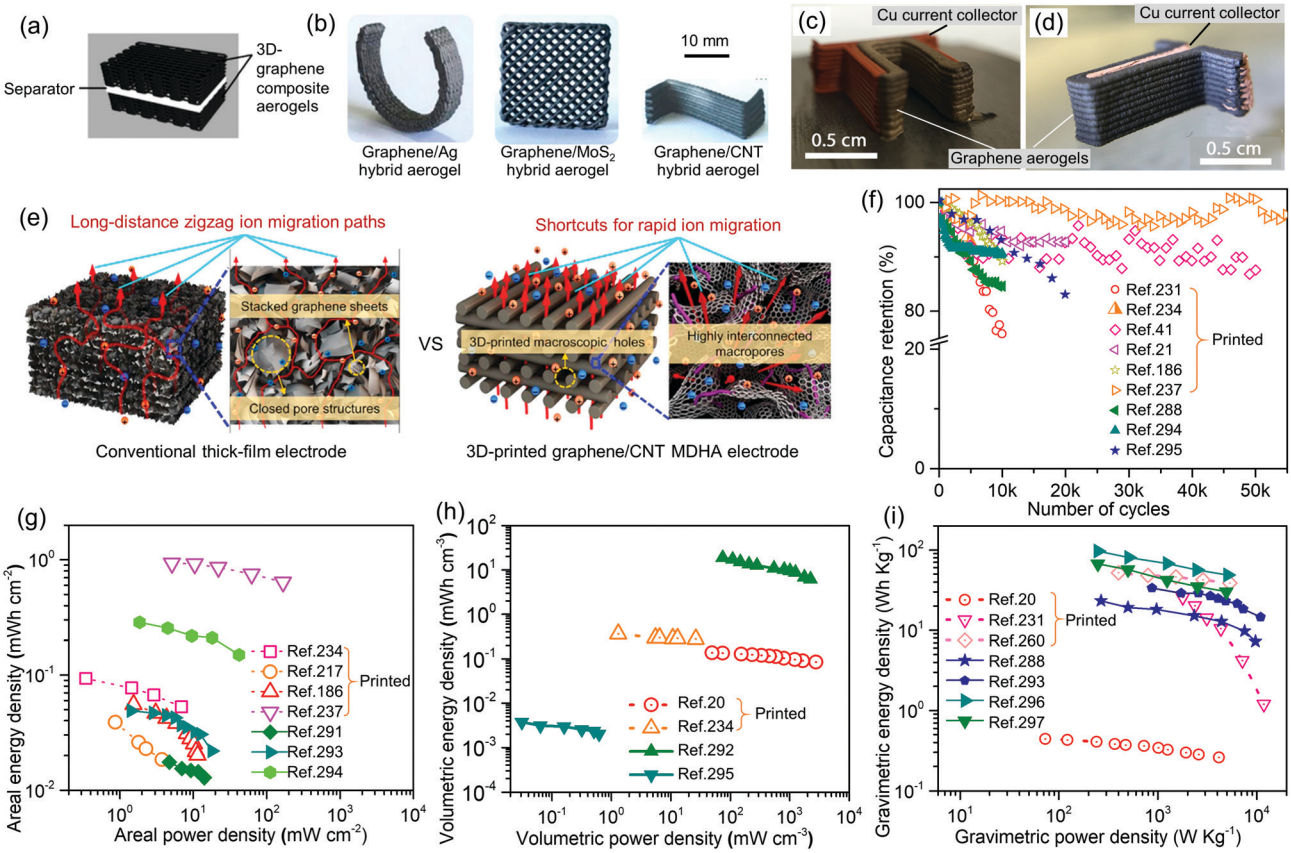

Fig. 20 Printed aerogels for supercapacitors and electrodes. (a) Schematic illustration of the 3D-GCA symmetric supercapacitor. Reproduced with permission from ref. 20. Copyright 2016 American Chemical Society. (b) Photographs of the 3D-printed Graphene/Ag, Graphene/CNT, and Graphene/MoS_2 mixed dimensional hybrid aerogels (MDHAs). Reproduced with permission from ref. 186. Copyright 2018 American Chemical Society. Photographs of a printed graphene aerogel supercapacitor composed of a (c) two-leg electrode and (d) one-leg electrode, both with Cu current collectors. (c and d) Reproduced with permission from ref. 231. Copyright 2017 American Chemical Society. (e) Schematic illustrations of insufficient ion migration for a conventional thick-film electrode and sufficient ion migration for the 3D-printed Graphene/CNT MDHA electrode. Reproduced with permission from ref. 186. Copyright 2018 American Chemical Society. Comparative survey from published literature: (f) capacitance retention as a function of cycle number, (g) areal energy density as a function of areal power density, (h) volumetric energy density as a function of volumetric power density, and (i) gravimetric energy density as a function of gravimetric power density.

From this perspective, deliberate design and printing of graphene aerogel microlattices with a gradient porous structure can further promote rapid diffusion of electrolyte ions and effective usage of the electrode volume.[41,289,290] In addition, since extrusion-based 3D printing can increase the electrode thickness,[19,21,217,260] which linearly increases the corresponding capacitance,[21,237] this fabrication approach could also be used to tailor the overall performance metrics.

Fig. 20f–i show comparisons between printed and the state-of-the-art non-printed aerogel supercapacitors in terms of capacitance retention at long cycles, areal energy density, volumetric energy density, and gravimetric energy density. The performance parameters of the printed devices are comparable, and in the majority of the cases, better than their non-printed counterparts.[288,291–299] In particular, we note that even after 50 000 cycles at 10 A g^{-1}, two reports on supercapacitors fabricated by 3D printed graphene aerogels show a high capacitance retention of 90% (Fig. 20f),[41,234] in comparison to rapid retention drops in the non-printed devices. This is very likely due to a combination of factors, including structural and electrochemical stability of the aerogel skeleton,[41] and better diffusion kinetics. Therefore, the added advantage of creating complex structures and customised geometries from 3D printing offer significant device integration benefits over traditional bulk aerogels, which can only be formed by hand cutting.[234]

5.2.2 Lithium ion or metal batteries. The lithium-ion battery (LIB) is a type of rechargeable battery which uses an intercalated lithium compound as the electrode material. Its operation depends on the movement of lithium ions between the electrodes. The skeleton structure of the electrode material in LIBs should have a high specific surface area to shorten the lithium ion diffusion path, reduce the surface current density, and improve the battery's dynamic performance. Fully 3D printed LIBs have been demonstrated,[261] using lithium iron phosphate ($LiFePO_4$) and lithium titanium oxide ($Li_4Ti_5O_{12}$) as the active materials for GO-based positive and negative electrodes, respectively, to obtain a pair of miniaturized interdigitated electrodes (Fig. 21a). The fully charged battery has initial charging and discharging capacities of

Table 10 Capacitive performance of various electrodes made from 3D printed and non-printed bulk aerogels

Category	Electrode	Rate capability	Capacitance (at highest current density)	Thickness
3D printed	DIW-CA[19]	69% (from 1 to 10 A g^{-1})	86 F g^{-1} (10 A g^{-1})	—
	GO-GNP-SiO_2-2[20]	88.7% (from 0.5 to 10 A g^{-1})	63.6 F g^{-1} (10 A g^{-1})	1000 μm
	3D G/MnO_2[21]	56% (from 0.5 to 50 mA cm^{-2})	*ca.* 6.43 F cm^{-2} (50 mA cm^{-2})	1000 μm
	SF-3D GA[237]	73.2% (from 5 to 100 mA cm^{-2})	*ca.* 1.16 F cm^{-2} (100 mA cm^{-2})	2000 μm
	DIW-ACA[19]	79% (from 1 to 10 A g^{-1})	*ca.* 171 F g^{-1} (10 A g^{-1})	—
	PG/MWCNT 4 : 1[178]	*ca.* 60.4% (from 1 to 100 A g^{-1})	*ca.* 100.5 F g^{-1} (100 A g^{-1})	—
	rCMG/Cu[231]	*ca.* 75.9% (from 3 to 30 A g^{-1})	13 F g^{-1} (30 A g^{-1})	—
	PPy-GA-0.1M[234]	90% (from 0.1 to 4 A g^{-1})	395 F g^{-1} (1 A g^{-1})	2000 μm
	3DGC-1[41]	85.9% (from 0.5 to 100 A g^{-1})	183 F g^{-1} (100 A g^{-1})	300 μm
	MnO_2/GA[241]	*ca.* 33% (from 1 to 10 A g^{-1})	90 F g^{-1} (10 A g^{-1})	—
	G/ZnV_2O_6@$Co_3V_2O_8$//G/VN[260]	78% (from 0.5 to 8 A g^{-1})	116.8 F g^{-1} (8 A g^{-1})	—
	Graphene/MWCNT MDHA 2 mm[186]	71.4% (from 4 to 40 mA cm^{-2})	456.69 mF cm^{-2} (40 mA cm^{-2})	2000 μm
Bulk (non-printed)	Bulk CA[19]	31% (from 1 to 10 A g^{-1})	*ca.* 17 F g^{-1} (10 A g^{-1})	—
	Bulk GO-GNP-SiO_2-2[20]	*ca.* 82% (from 0.5 to 10 A g^{-1})	*ca.* 47 F g^{-1} (10 A g^{-1})	1000 μm
	Bulk G/MnO_2[21]	11% (0.5–50 mA cm^{-2})	*ca.* 0.50 F cm^{-2} (50 mA cm^{-2})	1000 μm
	Bulk SF GA[237]	29.0% (from 5 to 100 mA cm^{-2})	*ca.* 0.40 F cm^{-2} (100 mA cm^{-2})	—
	pCA-KOH-700[288]	90.9% (from 1 to 10 A g^{-1})	330 F g^{-1} (10 A g^{-1})	—
	CNF/RGO/MoO_xN_y[292]	62% (from 1 to 15 A g^{-1})	421 F g^{-1} (15 A g^{-1})	—
	AAP(rGO-Co_3O_4//rGO)[293]	59.7% (from 2 to 30 mA cm^{-2})	119.8 mF cm^{-2} (30 mA cm^{-2})	—
	FeOCl@CDCA[294]	~58% (from 2 to 50 mA cm^{-2})	74 F g^{-1} (50 mA cm^{-2})	—
	AASC(MnO_2@CNTs@3DGA//PPy@CNTs@3DGA)-3.9[295]	~84.6% (from 1 to 20 mA cm^{-2})	950 mF cm^{-2} (1 mA cm^{-2})	—
	N-GA@V_2O_5 NWAs[296]	*ca.* 50% (from 0.5 to 10 A g^{-1})	360 F g^{-1} (10 A g^{-1})	—
	RGO/V_2O_5[297]	55.6% (from 1 to 8 A g^{-1})	178 F g^{-1} (8 A g^{-1})	—
	Graphene hydrogel film-1 M H_2SO_4[298]	80% (from 1 to 20 A g^{-1})	~152 F g^{-1} (20 A g^{-1})	—
	GAMOF(Fe^{3+})[299]	74.4% (from 1 to 20 A g^{-1})	353 F g^{-1} (20 A g^{-1})	—

117 and 91 mA h g^{-1}, respectively; Fig. 21c. This 3D printing method proves that battery arrays can be designed and printed in specific shapes and sizes to meet specific requirements of voltage and current (Fig. 21b).

Rechargeable lithium metal batteries (LMBs) using lithium metal or lithium alloy as the anode material and non-aqueous electrolyte solution are considered as the next-generation Li-based rechargeable batteries. This is because of the highest theoretical energy density and lowest standard reduction potential of lithium metal among the candidate materials.[300] However, the existing lithium metal electrodes are always planar, making it difficult to meet the requirements of miniaturization and customized form factors. Recently, CNF was used to manufacture LMBs *via* 3D extrusion printing.[218] The 3D printed CNF (Fig. 21d) was first carbonised to obtain a carbon aerogel (Fig. 21e). Molten lithium was then injected to form a high aspect ratio carbon/Li anode (Fig. 21f). Importantly, the fully 3D printed LMBs show a high capacity of 80 mA h g^{-1} at a charge and discharge rate of 10C (Fig. 21g), with an 85% capacity retention after 3000 cycles (Fig. 21h). This stable cycling performance of the full cell is attributed to the macroporous structure of the 3D printed carbon aerogel scaffold. The authors suggest that the scaffold offers two benefits. First, it allows the cathode to have good electrolyte accessibility, which accelerates the charge transfer during cycling. Second, it helps to improve the anode ion accessibility and reduce the local current density of the lithium anode, effectively stabilizing Li and suppressing dendrite formation.[218]

5.2.3 Sodium ion or metal batteries. The structure of a sodium ion (Na^+) battery (SIB) is very similar to that of a LIB. It works by insertion and extraction of Na^+ back and forth between the two electrodes to store and release electrical energy. Due to the rich reserves of sodium salt in the world, SIBs have the advantage of low cost, while their energy density is comparable to lithium iron phosphate batteries. Since the size of Na^+ (0.102 nm) is larger than that of the lithium ion (0.076 nm),[264] the electrolyte penetration and diffusion of Na^+ through the supported framework is harder than that in LIBs, resulting in low reversible capacity and low energy storage rate. Therefore, the design of electrode materials with a suitable pore structure will be key to the widespread success of sodium ion batteries.

Recently, highly porous aerogels of rGO[238,264] and hybrid MoS_2-graphene[242] have been 3D printed to address this challenge. Using $Na_3V_2(PO_4)_3$ (NVP)- and GO-containing aqueous inks (Fig. 22),[264] the first implementation of 3D printed SIBs was demonstrated. The printed continuous frameworks and hierarchically porous structure (Fig. 22b–d) can facilitate the rapid transport of Na^+ and electrons. The capacity retention is over 90% after 900 cycles at 1C (Fig. 22f). In another example, an SIB with 3D inkjet printed hybrid MoS_2-graphene aerogel electrodes was demonstrated.[242] The results show that the 3D printed macroporous structure can sustain fast and stable high-capacity intercalation of large Na^+ ions.

For sodium metal applications, inkjet printing of a 3D graphene lattice was demonstrated for sodium metal anodes.[238] The 3D printed hierarchical and multiscale structure shows better stability (reversible and stable beyond 500 cycles) in coulombic efficiency than non-printed porous graphene papers (only stable to ~170 cycles).

5.2.4 Hybrid energy storage devices. Battery-supercapacitor systems which store charge through a battery-type faradaic

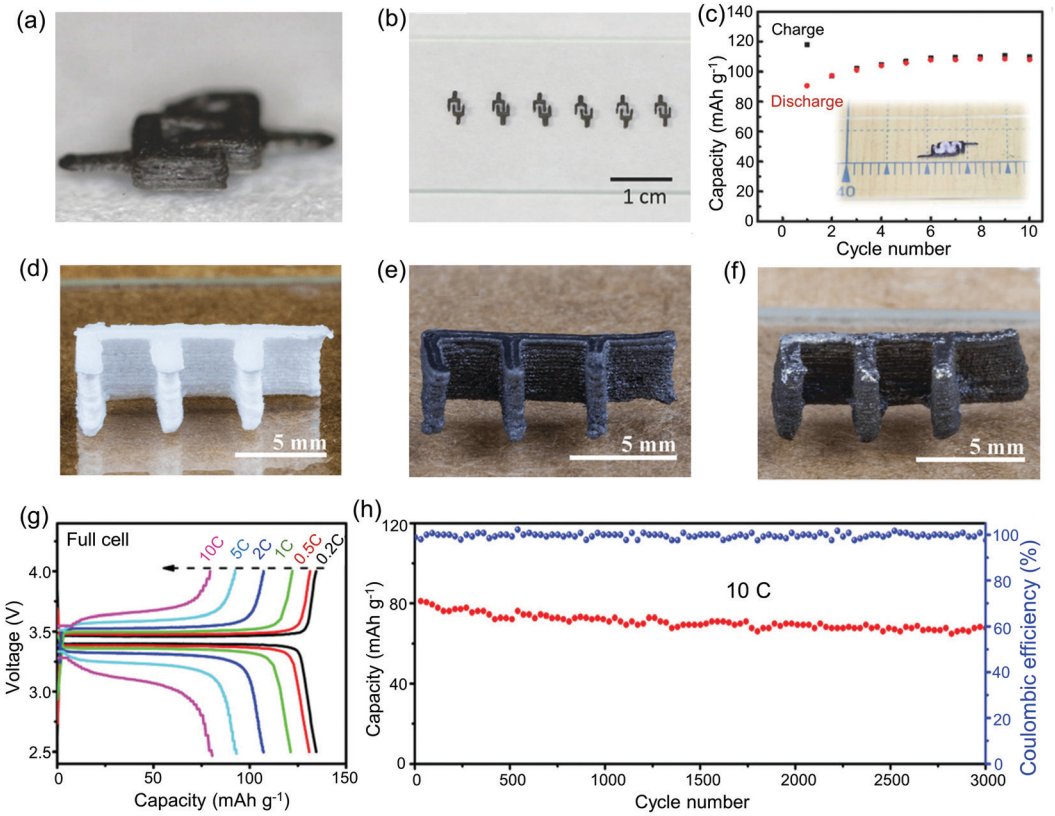

Fig. 21 (a–c) Lithium-ion batteries and (d–h) lithium metal micro-batteries assembled by 3D printing of aerogels. (a) Digital image of a 3D-printed miniaturized electrode pair. (b) Digital image of the 3D-printed electrode arrays. (c) Cycling stability of the 3D-printed full cell. The inset is a digital image of the 3D-printed full cell consisting of $LiFePO_4$/rGO, $Li_4Ti_5O_{12}$/rGO, and polymer electrolyte. (a–c) Reproduced with permission from ref. 261. Copyright 2016 WILEY-VCH. Photographs of a (d) 3D printed CNF aerogel scaffold, (e) carbon scaffold, and (f) carbon/Li electrode with designed 3D structure for lithium metal micro-batteries. (g) Voltage profiles at various rates from 0.2 to 10C. (h) Long-term cycling performance at 10C for the full cell with carbon/$LiFePO_4$ cathode and carbon/Li anode. (d-h) Reproduced with permission from ref. 218. Copyright 2019 WILEY-VCH.

process in one electrode and a capacitor mechanism in the other electrode fall into the category of hybrid energy storage devices. Since these devices combine the characteristics of supercapacitors and secondary batteries, they have the advantage of both high energy density and high-power density. They are considered as the ultimate source of power for multifunctional electronic equipment and electric/hybrid power vehicles in the future.[301,302] In 2018, such a hybrid energy storage device,[249] in which both electrodes were aerogels, was manufactured by 3D extrusion printing (Fig. 23). The half battery-electrode was a 3D printed $Ni_{0.33}Co_{0.66}S_2$/graphene (3DP-NCS/G) aerogel, while the half supercapacitor-electrode was a 3D printed CNT/graphene (3DP-CNT/G) aerogel.[186]

The areal energy density of the printed aerogel device is higher than that of other Ni–Co–S based electrodes (Fig. 23f),[303–308] partly because of its higher mass loading (17.86 mg cm^{-2})[249] compared to other electrode materials (1.77–11.2 mg cm^{-2}).[303–305] Importantly, the capacitance of other electrodes with high mass loading drops significantly, due to the limited electron/ion transport capacity in the thick film electrodes.[309] The advantage of 3D printing is that the architecture with interconnected network and highly open macropores created during the 3D printing process can improve both the electrical conductivity and serve as an effective mass transfer channel (Fig. 23e), shortening the travel distance for electrons/ions in the redox reaction, ensuring excellent electrochemical performance under high mass loading.[249]

5.3 Printed aerogels for electronics

With the rapid development of artificial intelligence, the demand for miniaturization of various electronic devices has accelerated, especially in the field of wearables. Among them, sensors and actuators, many of which can benefit from the unique properties of aerogels, represent an important family of devices. Requirements for miniaturization and flexibility for direct integration of aerogels on wearable substrates bring unprecedented challenges to their design and manufacture. As a broad technology platform, functional printing can address this need. Key applications in this category include strain or tactile sensors, mechanical linear actuators or electrical fuses, triboelectric nanogenerators (TENGs) and gas or chemical sensors.

5.3.1 Strain or tactile sensors. These sensors are an important part of traditional or intelligent human-machine interaction platforms for the measurement of displacement, pressure or motion. Among these, resistive sensors, which use the mechanisms

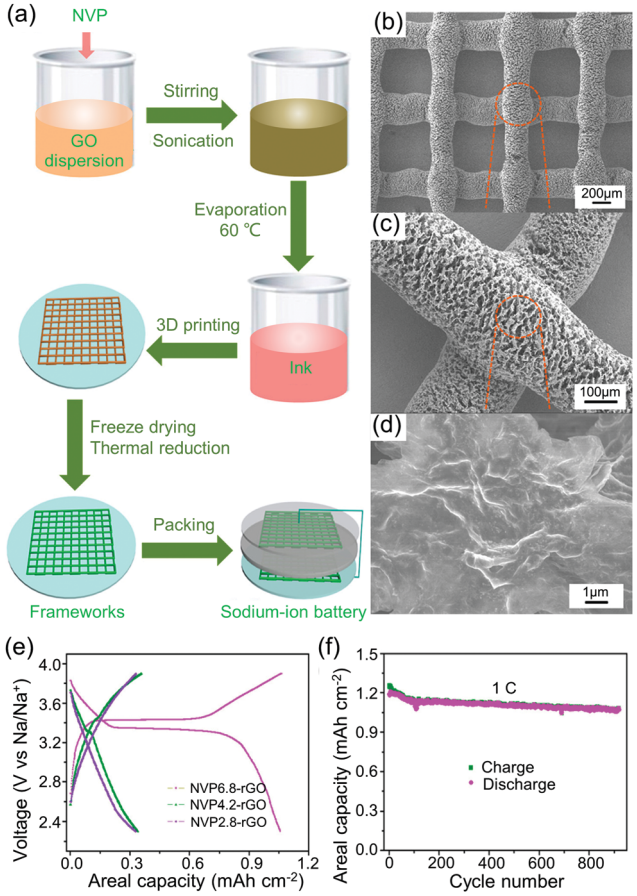

Fig. 22 Sodium-ion batteries fabricated by 3D printed rGO aerogels. (a) Schematic illustration showing the fabrication process of 3D-printed hierarchical porous frameworks. (b–d) SEM images of 3D-printed rGO aerogel frameworks with different magnifications. (e) Charge and discharge profiles at 2C. (f) Long cycling performance of NVP6.8-rGO at 1C. Reproduced with permission from ref. 264. Copyright 2017 American Chemical Society.

where materials change their electrical resistance under mechanical strain, are the most studied in the area of wearable sensors.[310] Since the majority of application scope of these devices require them to be directly or indirectly (*e.g.*, through textile) attached to the human body, they need to be lightweight, sensitive, flexible and capable of withstanding a wide range of strains, with long cycle life.

Graphene[104,311,312] or fibrous carbon-based[313] aerogels are highly flexible, and can endure high strain through expansion and compression processes, resulting in a large change in the contact area between the nanosheets or fibres, and consequently, the overall electrical resistance.[311] The application of printing technology can further increase the deformation range of the flexible aerogels. For example, 3D printed porous GO-CNT aerogel mesh can reach 200% elongation, whereas traditional aerogels break at 25%.[258]

Materials for aerogel based 3D printed strain sensors demonstrated to date have mainly focused on graphene,[18,109,171,235,259] and CNT-graphene hybrids.[258] Tactile sensors from 3D printed PDMS microbeads/GO nanocomposite,[240] or graphene[235] aerogels have also been demonstrated. The densities of these printed aerogels are usually in the range of 0.5 to 25 mg cm^{-3},[109,235,258] with typical electrical conductivity between 15.4 and 130 S m^{-1}.[109,235] We note that the miniaturization of these ultra-light sensors is directly related to the nozzle diameter of the extruders. The internal diameter of typical extrusion nozzles for current generation 3D printing is in the range of tens to hundreds of microns, with the best printing accuracy of 50 μm.[258]

Fig. 24 shows two examples of wearable strain[235] and tactile[259] sensors using 3D extrusion printed graphene aerogels. In the first example, four serpentine resistive aerogel sensors were integrated on to the finger joints on to gloves (Fig. 24a) to accurately monitor the complex and subtle changes in human finger joints (Fig. 24b and c).[235] Inspired by the structure–activity relationship between the different microstructures of the spiral and radial lines in the spider web, the second example of an extrusion printed sensor (Fig. 24d–f) demonstrated a multi-resolution tactile platform to analyse and classify touch in different directions, distances and locations.[259] The authors also designed a simulated graphene skin to manipulate the corresponding mechanical fingers with very small pressures ($<3.83 \times 10^{-3}$ Pa).[259]

The above examples imply that 3D printing technology has brought these aerogel-based resistive sensors a degree of design freedom that is difficult to achieve by traditional shaping methods. With this flexibility, complex connected structures in a millimetre-scale form-factor can be engineered to achieve a desired impedance range and pressure detection accuracy, promoting their development in customizable miniaturised sensors.[314]

5.3.2 Actuators. Unlike the strain sensors which can be used to convert mechanical forces into electrical signals, actuators convert electrical signals directly into mechanical forces or displacements. Miniaturization of such devices opens huge opportunities in soft robotics, micromanipulation, and medical applications.[315,316] In particular, conductive polymer based bending actuators are very popular for these applications due to their low operating voltage (0.5–7 V), thin form-factor and high force-to-size ratio, even at the microscale regime. In addition to the linear expansion actuators, there are bi- and tri-layer bending actuators (Fig. 25a).[315] In the trilayer variety, which sometimes offers better degrees of control, both sides of the polymer separator are coated with conductive polymer electrodes. The entire actuator is saturated with electrolyte. When an external voltage is applied, the electrolyte ions move into or out of the electrode to compensate for the charge, causing the electrode volume to expand and contract, showing a bending drive.[213] If nanoporous aerogel is used as an electrode, it may help in adjusting the porosity and conductivity of the electrodes, affecting their driving performance.

Aerogels were first introduced in actuators in 2017, by inkjet printing a mixture of PEDOT-poly(styrenesulfonate) (PEDOT:PSS) conducting polymer and ACA on both sides of a PVDF membrane.[212,213] Compared to the pure PEDOT: PSS variety, the actuator with PEDOT:PSS-ACA electrodes achieved a higher bending stress (Fig. 25b) due to the higher conductivity, ion diffusion rate, and specific capacitance. In this example, inkjet

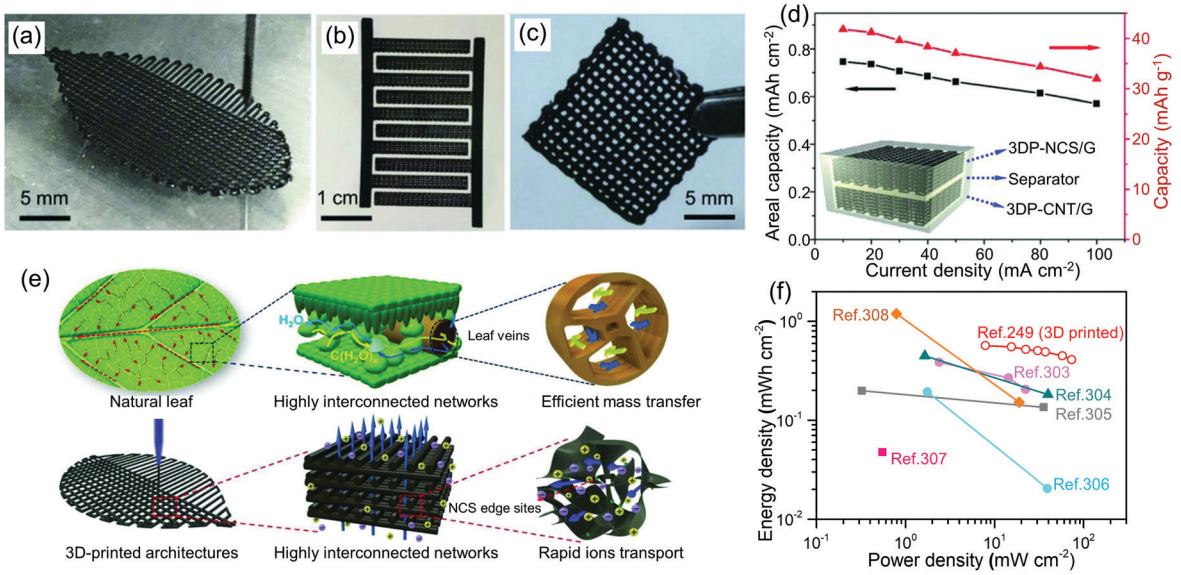

Fig. 23 3D printed graphene-based hybrid energy devices. Photographs of the printed objects before drying (a and b) and aerogel (c). (d) Calculated specific capacitances of the device at different current densities. Inset: Schematic illustration of the hybrid energy storage device. (e) Schematic illustration of the mass transport process in a natural leaf and 3DP-NCS/G aerogel electrode. (a–e) Reproduced with permission from ref. 249. Copyright 2018 WILEY-VCH. (f) Ragone plots of areal energy densities *versus* power densities of the 3D printed graphene-based hybrid energy device compared with non-printed electrodes based on Ni–Co–S materials.

printing allowed the authors to control the shape and thickness of the polymer-aerogel hybrid films.

In another example, 3D extrusion printing technology was used to fabricate a micro oscillator based on graphene-shape memory polymer (G-SMP) nanocomposite aerogels (Fig. 25c–f).[236] The stretchable 3D printed graphene aerogel framework, with high electrical ($\sim$1100 S m^{-1}) and thermal conductivity ($\sim$3.6 W m^{-1} K^{-1}), acts as an overall energy conversion grid for rapid heat generation and injection (Fig. 25c). This method increased the response speed of the oscillator to 50 milliseconds which is several orders of magnitude better than traditional bulk SMP composites, and is comparable to shape memory alloys. The G-SMP aerogel oscillator (Fig. 25d) can respond and oscillate with negligible hysteresis (80 ms) (Fig. 25e and f), because of its fast thermal energy generation and injection. The performance of the actuator is also very repeatable and stable, primarily due to the highly stretchable and intricate grid structure printed by 3D extrusion technology.

5.3.3 Triboelectric nanogenerators. TENGs are devices that can convert mechanical energy into usable electrical energy based on the triboelectric effect.[317,318] When there is friction between two different materials, opposite charges are generated on both the surfaces under friction, forming a triboelectric potential between them. The advantages of TENGs are that they are lightweight and inexpensive, and can harvest almost all kinds of mechanical energy from vibrations, including biomechanical energy.[319] Besides the selection of two materials with large differences in electronic affinity, increasing the area by changing the physical structure of the surfaces under friction can improve the performance of TENGs.[319] High elasticity is another important requirement, especially for soft devices and wearables. Because nanomaterial-based aerogels have high surface area and elasticity, they have excellent potential for TENG applications.

Based on 3D extrusion printing, two different types of TENGs have thus far been fabricated by graphene (Fig. 26a–c)[107] and CNF (Fig. 26d–f)[228] aerogels, respectively. In one example, a 3D printed graphene aerogel has been used as one of the electrodes of the TENG, the other being an Al foil. The Young's modulus of this printed aerogel is more than three times higher than that of the super-elastic bulk graphene materials (Fig. 26a). In this TENG structure, the two electrodes are separated by a fluorinated ethylene propylene (FEP) film (Fig. 26b). When the TENG is manually tapped, ten LEDs connected in series could be fully lit (Fig. 26c), indicating sufficient conversion efficiency.[107]

In an all-printed TENG (AP-TENG) design,[228] the two friction layers of PDMS and CNF aerogels, and the corresponding Ag electrodes were fabricated by 3D extrusion (Fig. 26d). The output voltage of this AP-TENG is 75% higher than that of a traditional TENG (Fig. 26e) and is stable under different pressures (Fig. 26f).

The above examples demonstrate that the combination of 3D printing technology and nanoporous aerogels could enhance the contact area, surface properties, and mechanical flexibility of TENGs, improving the mechanical resilience and triboelectric response.

5.3.4 Chemical sensors. Gas sensors are used to identify and measure the concentration of target gases to investigate or control an environment.[320] Among the various types, resistive (also called chemiresistive) gas sensors are the most widely used. Their primary advantages include simple structure and support electronics, and low cost. Printed chemiresistive gas sensors offer additional advantages through easy processability, design flexibility, and suitability for a variety of substrates.[321]

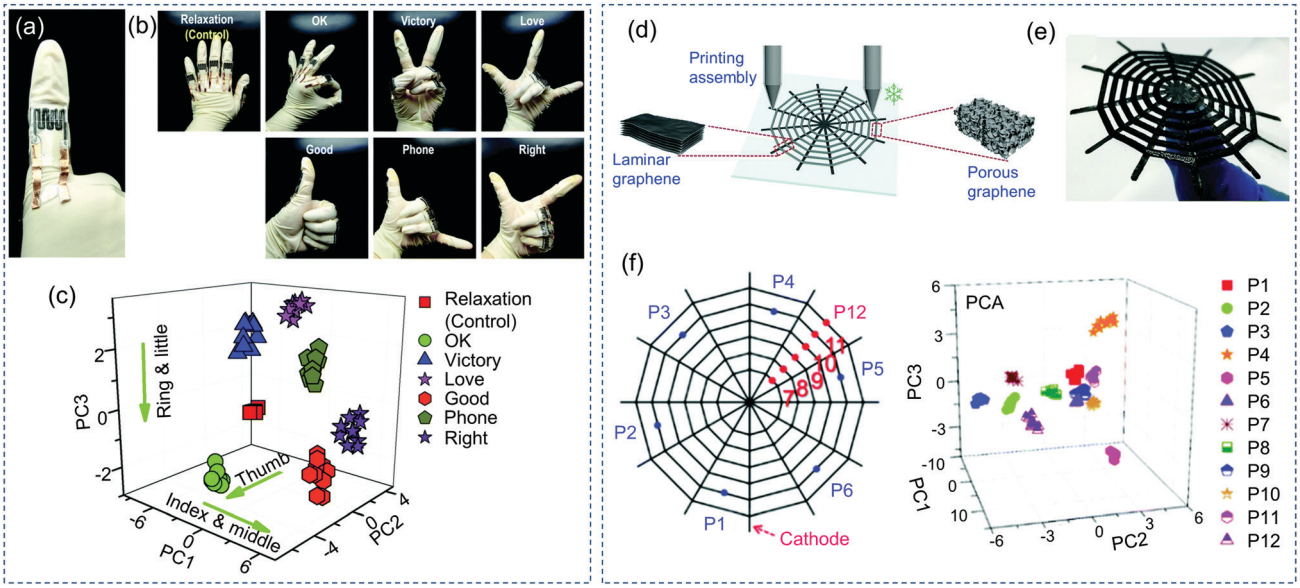

Fig. 24 3D printed aerogel (a–c) strain and (d–f) tactile sensors. (a) Photograph showing the printed graphene aerogel sensor attached on the index finger joint. (b) Sensors placed on the finger joints, and different gestures with the deformation degree of the sensors, (c) 3D representation of the principal component analysis (PCA) result showing a clear clustering of the seven different gestures as variables in the trends of the joint movements. (a–c) Reproduced from ref. 235 with permission from the Royal Society of Chemistry. (d) Schematic illustration of print-manipulated graphene nanosheets assembled into different micro-structures in the spiral and radial threads. (e) Photograph of the multi-resolution graphene tactile sensor under pressure. (f) Electronic discrimination analysis of positions based on the multi-resolution graphene tactile sensor. (d–f) Reproduced from ref. 259 with permission from the Royal Society of Chemistry.

The mechanism of resistive gas sensing is that the resistance of the active sensing layer changes when gas molecules come in contact with its surface.[201] The main performance parameters of the gas sensor include sensitivity, selectivity, detection limit, response and recovery time, and stability.[320,322] Because aerogels have high specific surface area and open-pore structures, they can provide a large number of abundant active sites to efficiently adsorb and detect gases. Aerogel-based gas sensors therefore usually have high sensitivity, and can be designed to have low detection limits.[3]

Printing technology can be used to design aerogel's macroporous structure and facilitate their direct integration on to the substrates and contacts. The former may promote enhanced gas diffusion and sensing compared to the bulk aerogels. Graphene aerogel lattices by a 3D printed template method have already been used to demonstrate sensors for volatile organic compound (VOC) detection (Fig. 27).[243] The conductivity of the graphene aerogel decreases after it comes in contact with liquid reagents, and the light intensity of the LED lamp becomes dim (Fig. 27a–d). This sensor can be used to detect different types of chemical reagents (Fig. 27e) and different concentrations (Fig. 27f), showing excellent measurement repeatability (Fig. 27g).[243]

3D printing on aerogels allows engineering and fine tuning of the pores and skeleton structures on multiple scales. Therefore, the sensor sensitivity can be adjusted accordingly,[243] while the mass transfer can be improved by careful design of hierarchical pores,[270] increasing the adsorption and desorption rate, and improved detection efficiency.

5.3.5 Other electronics. Flexibility, electrical conductivity, and macrostructural designability of printed aerogels make them an attractive proposition for stretchable[245] or anisotropic conductors.[239] For example, a graphene honeycomb (GHC) structure (Fig. 28b) by a 3D printed template was used to fabricate a stretchable light-emitting display consisting of an LED array with two sets of GHCs as conductors (Fig. 28a and c). This structure greatly improves the flexibility of graphene aerogels, allowing the LED array to exhibit a stable performance under different load modes, such as stretching and bending without any cracks or breaks (Fig. 28d–f).[245] Such ordered hexagonal honeycomb structures at a millimetre scale would be challenging to fabricate using traditional shaping methods.

3D printing technology has also been used to directly print Ag nanowire (AgNW) aerogel circular ring electrodes and ZnO nanowire (ZONW) aerogels as cylindrical photosensitive materials (Fig. 28g) to fabricate UV sensors directly onto microfibres (Fig. 28h). These UV sensors, which can be woven directly into fabrics at a precise location, with specific material combination through extrusion,[217] offer stretchability or repeatable performance (Fig. 28j). Such manufacturing adaptability would be challenging to replicate using conventional approaches.

5.4 Printed aerogels for chemical applications

The intrinsic characteristics of aerogels such as large surface area, high porosity, and adjustable surface chemistry endow them with excellent supporting and adsorption capacity. Therefore, they are very attractive as potential catalyst supports or adsorbents in chemical synthesis or environmental protection.[323] However, the mesoporous structure of aerogels exhibits relatively poor mass transfer performance. Therefore,

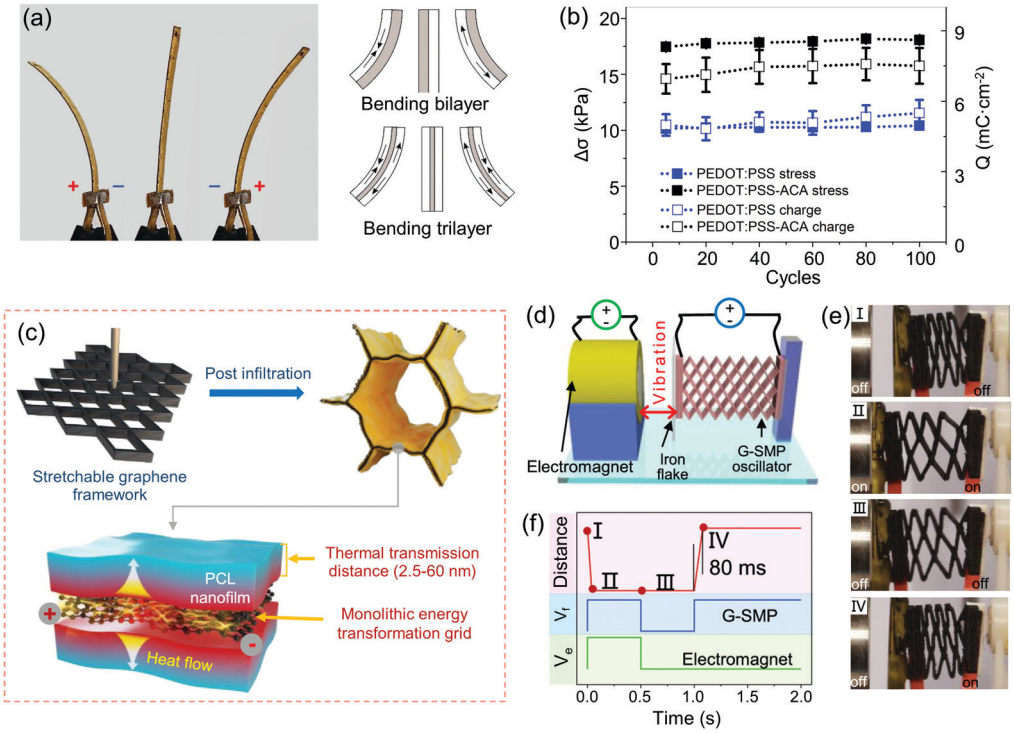

Fig. 25 Printed aerogels as actuators and oscillators. (a) Photograph and schematic illustration of bending of an ionic electromechanically active polymer actuator. Adapted from ref. 315. Published by MDPI. (b) Durability of stress (filled) and charge density (empty) of PEDOT:PSS- and PEDOT:PSS-ACA-PVDF trilayer at linear actuation. Reproduced with permission from ref. 212. Copyright 2017 Elsevier B.V. (c) Schematic illustration of the fabrication process of a graphene/SMP nanocomposite aerogel that encompasses a monolithic graphene framework and polycaprolactone (PCL) nanofilm. (d) Schematic illustration of the high-speed G-SMP oscillator. (e) The original state (I) and three critical states (II, III, IV) during one oscillation cycle. (f) Impulse voltage on G-SMP (V_f), electromagnet (V_e), and the consequent distance change in a cycle. (c–f) Adapted with permission from ref. 236. Copyright 2019 American Chemical Society.

when aerogel is used as a catalyst or adsorbent, it is generally applied in the form of particles, not in large monoliths. However, the drawback of poor mass transfer inside the aerogel particles, and low space utilization due to too large pores between the particles still exist. Since 3D printing offers design and regulation of aerogel macropores, it can be used to optimise mass transfer in materials, for example, through designs following Murray's law which mimics animal respiratory or plant vascular systems with hierarchical, area/volume preserving networks and precise pore diameter ratios,[289] promoting their application in catalysis and adsorption.

5.4.1 Catalysts. Aerogels have been widely used as catalysts in gas-solid and liquid–solid catalytic reactions due to its high porosity and specific surface area.[1,2,324] Recently an extrusion-printed 3D CeZrLa-GO nanocatalyst has been demonstrated (Fig. 29)[247] which allows the 3D aerogel structure to be directly installed into the reactor (Fig. 29b) for propylene carbonate production. Compared with the starting powder form, the 3D printed CeZrLa-GO nanocatalysts show higher activity and conversion, and no significant change in selectivity (Fig. 29c). The all-in-one 3D printed nanocatalysts can be easily separated from the reaction mixture. Compared to traditional methods, this 3D printed catalyst reactor has many operational and structural advantages, including direct and customizable installation, high volume efficiency, and better mass and heat transfer, as well as excellent mechanical and structural integrity.[247,325]

5.4.2 Adsorbents. A large number of studies have investigated aerogels as adsorbents for water treatment (such as water and oil separation, heavy metal ion removal) and air purification (such as volatile solvent, toxic gas removal, CO_2 capture).[323,326,327] Depending on the specific application, the general research in this area focuses on the surface chemical modification, design of porous structures, and mechanical flexibility and reusability.

3D printing technology can promote microstructure design, and improve adsorption selectivity and capacity.[140,328] Indeed, porous graphene lattices by 3D printed templates have been demonstrated as selective adsorbents for inorganic and organic solvents (Fig. 30),[243] with adsorption capacities of organic solvents as high as >2000% (Fig. 30a). The nanoporous structure of the aerogels produces a strong adsorption by capillary tension, while the macropores created by printing provide a mass transfer channel to ensure that high-viscosity liquids like asphalt can be adsorbed and removed by Joule heating. Such designs also ensure the reusability and structural stability for multiple adsorption-combustion cycles for various combustible liquids (Fig. 30b).

5.5 Printed aerogels for biomedical applications

The majority of aerogel applications in the fields related to biocompatibility include tissue engineering, drug delivery and

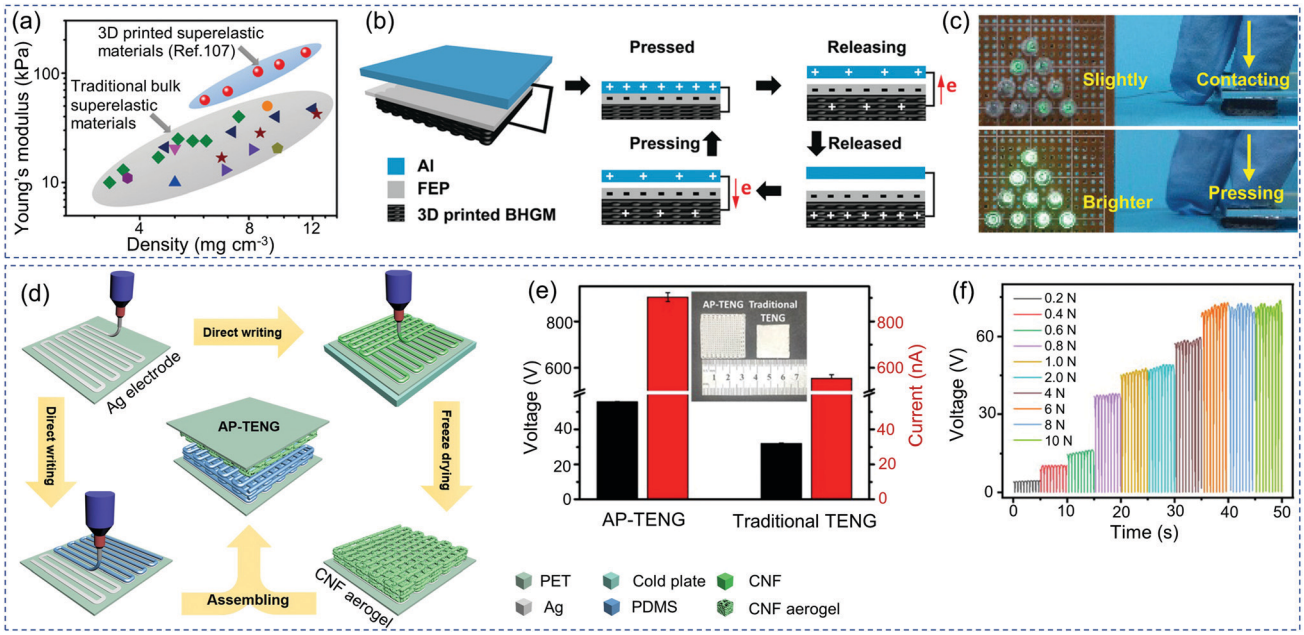

Fig. 26 3D printed aerogels for TENGs. (a) Young's modulus of 3D-printed hierarchical graphene materials (BHGMs). (b) Schematic illustration of electricity generation in a nanogenerator in contact-separation mode. (c) Photographs of ten green LEDs powered by hand tapping at (top) small compression and (bottom) large compression. (a–c) Adapted with permission from ref. 107. Copyright 2019 WILEY-VCH. (d) Schematic illustration showing the fabrication process of an AP-TENG. (e) The output of a 3D hierarchical patterned AP-TENG and the mould-cast flat microporous TENG counterpart. (f) The output performance of the AP-TENG at different pressures. (d–f) Adapted with permission from ref. 228. Copyright 2019 Elsevier Ltd.

biosensing. The high porosity of aerogels and their connectivity in open nanostructures are conducive to cell attachment, provide channels for nutrition and oxygen to cells, and additionally eliminate cell metabolism by-products, making aerogels a very attractive material for regenerative medicine.[329]

5.5.1 Tissue engineering. A large number of aerogels, including those based on hybrid SiO_2,[330] rGO,[331] collagen-alginate,[332] nanocellulose,[333] and carbon[334] have been investigated in tissue engineering applications. However, traditionally prepared aerogels often lack macropores, which are necessary for bone ingrowth and vascularization.[188] This issue can be addressed by 3D printing, which can precisely manufacture aerogels with designed macropores, and additionally, with shapes customised to certain organs or even individuals. Such flexibility in design makes printed aerogels very attractive for tissue engineering applications.[188]

For tissue regeneration, 3D printed aerogel scaffolds of a range of materials, including CNC,[181] CNF,[230] CNF/alginate,[225] PEGDA/CNF,[22] and gelatin/poly(lactic-*co*-glycolic acid) (PLGA)[23] have been investigated. For example, 3D printed gelatin/PLGA[23] has been evaluated for *in vitro* cartilage regeneration using scaffolds in conjunction with chondrocytes (Fig. 31).[23] A large number of live cells (green) are observed in both the non-printed (Fig. 31a) and the 3D printed (Fig. 31g) samples, with cartilage-like tissue forming in both groups (Fig. 31b and h). Indeed, as seen in Fig. 31c and i, chondrocytes produced rich extracellular matrixes, covering both the scaffolds. However, the specimens from the non-printed group are irregularly shaped and form very thin tissues (Fig. 31d–f). In contrast, the specimens in the 3D printed group with controlled pore

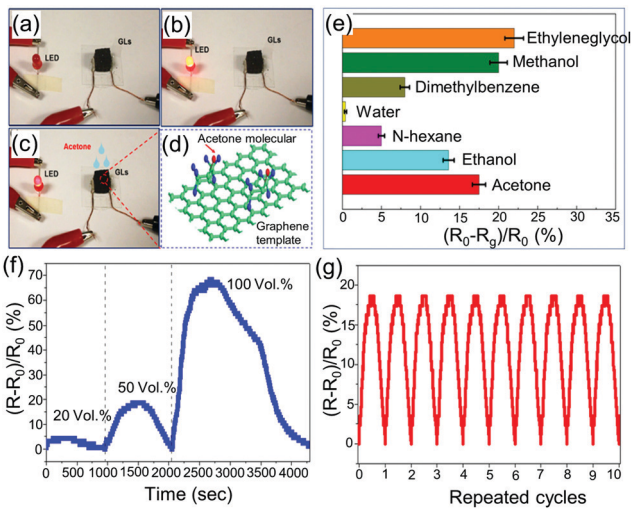

Fig. 27 Printed aerogels for chemical sensor applications. (a) Photograph of a chemiresistive sensor with LED light detection. (b) The LED glows brightly in the initial state before chemical reagent is added. (c) LED light dimmed, indicating change in electrical resistance in response to chemical agent. (d) Schematic illustration of sensing of acetone through interaction with rGO. (e) Resistance changes of the chemiresistors for different chemical agents. (f) Resistance changes of the sensor under different volume% of acetone. (g) Cycling stability of acetone sensing over 10 times. Reproduced with permission from ref. 243. Copyright 2018 American Chemical Society.

structure retain their original square shape and form thicker tissues (Fig. 31j–l). The authors propose that the improved cartilage regeneration in the 3D printed samples is primarily due to the

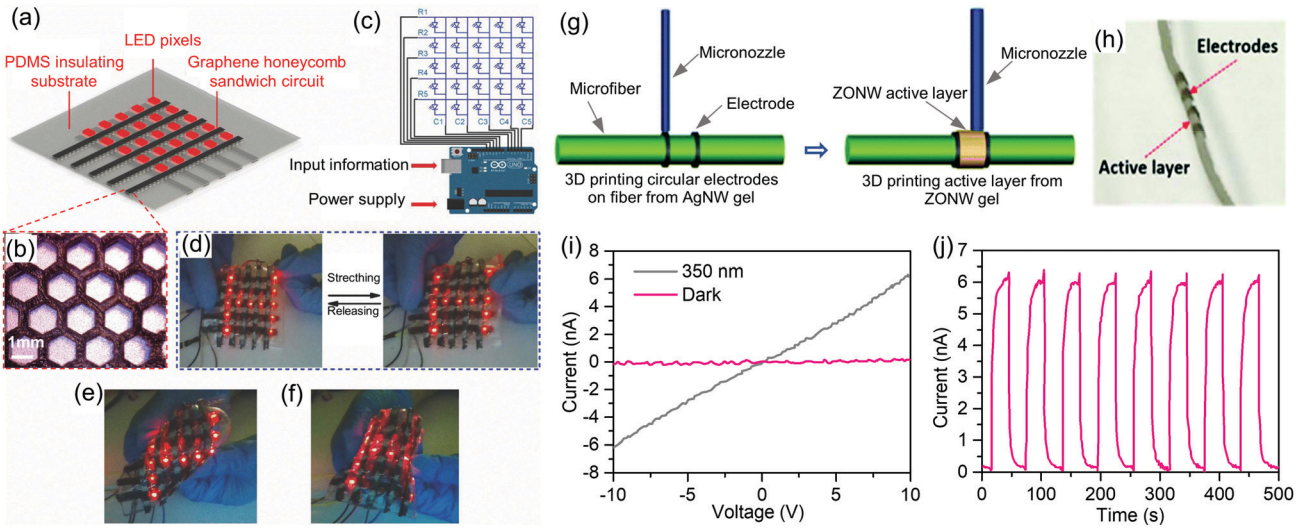

Fig. 28 3D printed aerogels used as electrical conductors and UV sensors. (a) Stretchable light-emitting display constructed using GHC sandwich as conductors. (b) Photograph of GHC. (c) Circuit connection in the display electronic system. (d) Photographs of the stretchable light-emitting display. (e and f) Performance of the conductors under twisting and bending. (a–f) Adapted with permission from ref. 245. Copyright 2018 WILEY-VCH. (g) Schematic illustration of extrusion-based printed UV sensors. (h) As-prepared fibre-based UV sensor. (i) *I*–*V* curves of the fibre-based UV sensor in the dark and under UV (350 nm) illumination at a bias of 10.0 V. (j) Reversible switching of electrical current for the fibre-based UV sensor at 10.0 V biasing voltage in the dark state and under UV light irradiation. (g–j) Adapted from ref. 217 with permission from the Royal Society of Chemistry.

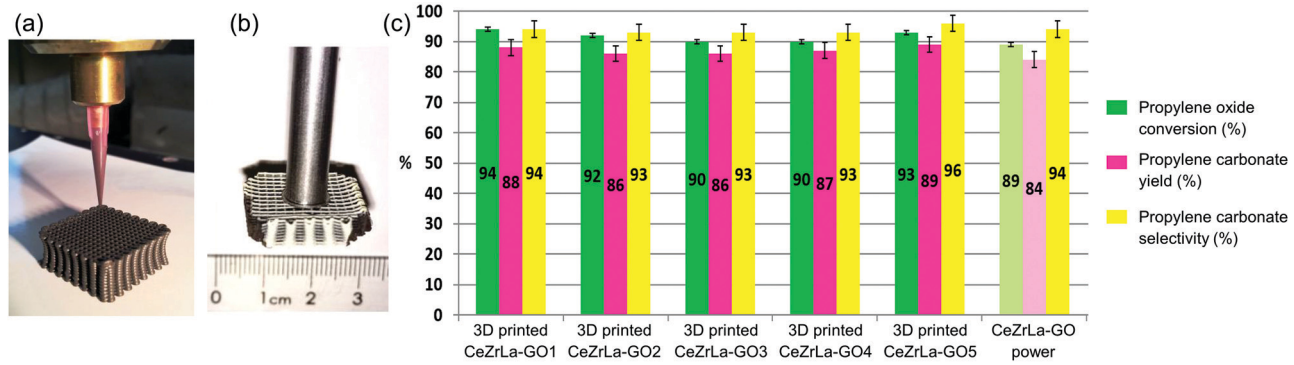

Fig. 29 3D printed graphene aerogels loaded with CeZrLa for catalyst applications. (a) 3D printing process of GO-supported CeZrLa structures. (b) Typical GO-supported CeZrLa structure mounted onto an impeller shaft of a stirred batch reactor cell. (c) Experimental results (repeatability tests) for the green synthesis of propylene carbonate using the printed GO-supported CeZrLa catalyst (first five sets from left to right) in comparison to its powder counterpart. Adapted with permission from ref. 247. Copyright 2019 Elsevier Ltd.

controlled pore structure of the 3D printed scaffolds, which ensures uniform cell distribution and nutritional supply, forming a relatively uniform cartilage-like tissue. This printed aerogel scaffold has good biocompatibility and rich macroporous structure, all of which are beneficial for its application in tissue engineering.[22,23]

5.5.2 Drug delivery. Drug delivery involves loading drugs in a carrier that provide accurate control of drug release rate in both time and space, so that the drug can reach the target efficiently to reduce the dosage and avoid unexpected side effects. This is especially important for cytotoxic (toxic to cells) drugs used to treat certain diseases. These delivery systems need to protect the carried drugs from severe degradation by the physiological environment in the body before arriving at the target.[188] Additionally, the carrier should be sufficiently small (micron-millimetre range) to be able to flow freely in the human circulatory system (such as blood vessels, respiratory tract, digestive tract, *etc.*) to reach the target site.

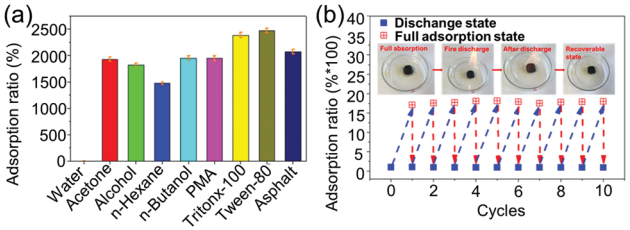

Fig. 30 3D printed graphene aerogel lattices for adsorbent applications. (a) Adsorption ratios of different chemical solvents. (b) Cycling stability of adsorption capacity of alcohol with natural adsorption and fire discharge processes. Reproduced with permission from ref. 243. Copyright 2018 American Chemical Society.

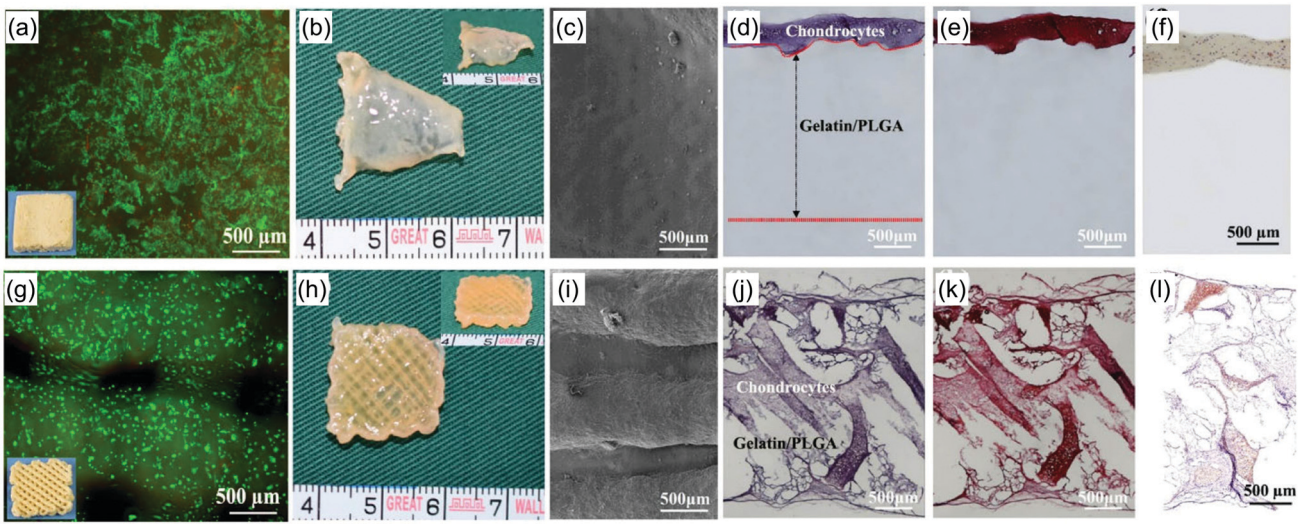

Fig. 31 3D printed gelatin/PLGA for *in vitro* cartilage regeneration. Fluorescence micrographs of chondrocytes seeded on (a) non-printed freeze-shaped gelatin/PLGA scaffold and (g) 3D-printed scaffold for 24 h (live and dead cells are dyed green and red, respectively). Overall appearance of cell-scaffold constructs in (b) non-printed and (h) 3D-printed groups after six weeks of *in vitro* culturing. SEM images present the extracellular matrix deposition in the (c) non-printed and (i) 3D-printed groups after six weeks. Histological analysis of cell-scaffold constructs in (d–f) non-printed and (j–l) 3D-printed groups after six weeks of *in vitro* culturing. Reproduced with permission from ref. 23. Copyright 2019 Elsevier Ltd.

A wide variety of drug carrier materials in an aerogel form have been investigated thus far, including SiO_2,[335] TiO_2,[336] chitosan,[337] pectin,[338] carrageenan,[339] alginate,[340] starch,[341] and cellulose.[342] These aerogels are traditionally shaped by one of the methods such as milling from monoliths, droplets through syringe into solution, and emulsion polymerization.[338,343–345]

Inkjet printing can produce fine ink droplets with diameters of tens of microns and as discussed before, can be used to fabricate ultrafine aerogel microspheres for drug delivery applications. Indeed, such a strategy to prepare alginate aerogel microspheres has been demonstrated for lung inhalation delivery of salbutamol sulphate (a drug used to treat bronchi or lung diseases); Fig. 32.[209] Inkjet printing was used to obtain uniform and fine particle size (23.8 ± 4.5 μm, Fig. 32a and b) for high fluidity. Importantly, the salbutamol sulphate-loaded microsphere's fine particle fraction (indicating the flowability) is close to 50%, better than some commercial salbutamol sulphate formulations (26–28%).[346,347] Additionally, fine nanopores in the aerogels ensure low continuous drug release for up to 10 hours (Fig. 32c). This method can be universally extended to other drug delivery approaches.

5.6 Printed aerogels for light-harvesting applications

Solar energy can be harvested through conversion to heat, electricity, and energy-rich chemicals (fuel), based on mechanisms such as solar-thermal conversion, photovoltaic effect, photocatalysis, photosynthesis, and photoelectrochemistry.[348,349] Thus far, non-printed aerogels have been used for a range of light-harvesting applications, including rGO-polyacrylamide (rGO-PAM),[350] hollow-carbon-nanotubes,[351] conjugated microporous polymer nanotubes,[352] graphene,[353] and MoS_2-graphene[254] for solar-steam generation, g-C_3N_4/GO for broad-spectrum photocatalysts,[354] g-C_3N_4/graphene/NiFe hydroxide for solar-driven photoelectrochemical water oxidation,[355] and SiO_2–TiO_2 for dye-sensitized solar cells.[356] Printing technologies allow for fabrication and direct integration of these aerogels into light-harvesting devices, especially in fine and gradient structure configurations, and therefore, can greatly enhance device performance and overall manufacturability.

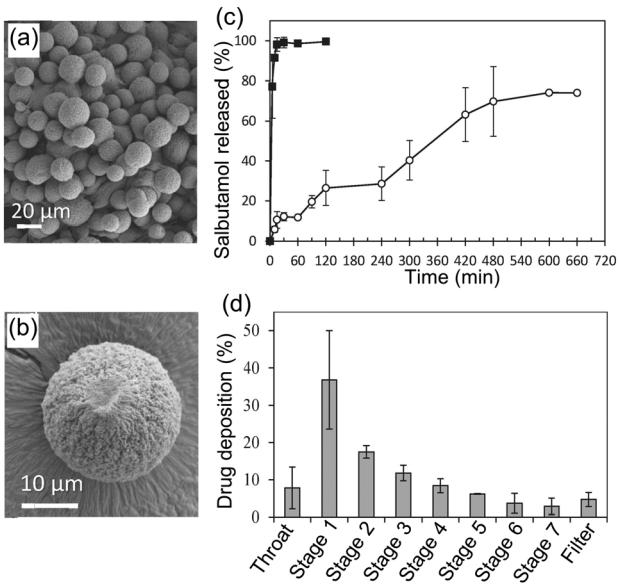

Fig. 32 Inkjet-printed aerogels for drug delivery. (a and b) SEM images of alginate aerogel microspheres obtained by inkjet printing. (c) *In vitro* release profile of salbutamol sulphate from the aerogel microspheres (white circles) in phosphate buffer solution, compared to the dissolution profile of salbutamol sulphate (black squares) under the same operating conditions. (d) Drug deposition profile of salbutamol sulphate loaded in alginate aerogel microspheres with a next generation impactor. Adapted with permission from ref. 209. Copyright 2018 Elsevier B.V.

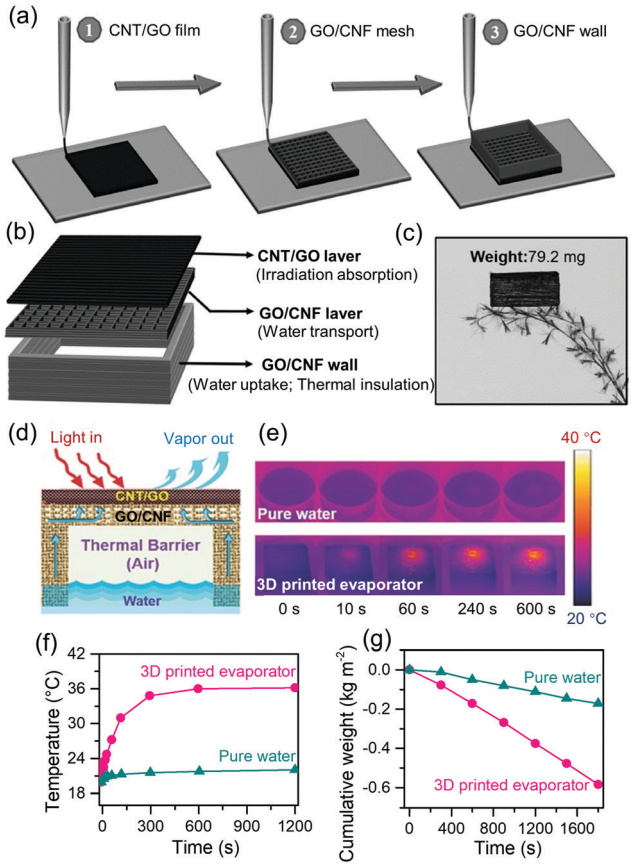

Fig. 33 All-in-one 3D printed aerogel structure for solar steam generation. (a) Schematic diagram showing the 3D printing enabled fabrication process. (b) Three-layer structure of the 3D printed evaporator. (c) Photograph of light-weight evaporator. (d) Schematic illustration of solar steam generation. (e) Infrared images of pure water and the generator at various time points under 1 Sun illumination. (f) Curves showing surface temperature change of pure water and the generator as a function of irradiation time. (g) Cumulative weight loss of pure water and the generator through water evaporation over time. Reproduced with permission from ref. 216. Copyright 2017 WILEY-VCH.

5.6.1 Solar steam generation. A solar steam generator is a device that can directly absorb sunlight, and turn it into heat to create steam from water. To achieve a highly efficient energy conversion, it is necessary to have strong light absorption, stable water transmission, and effective heat insulation of the steam generators.[357,358] To address these, a layered 3D printing technology has been used to fabricate an integrated device with a concave structure that can efficiently generate solar steam with a high efficiency of 85.6% under 1 sun illumination (Fig. 33).[216] The integrated structure is composed of three parts of aerogels, CNT/GO sunlight absorbing layer, GO/CNF water diffusion layer, and GO/CNF water delivery wall (Fig. 33b). The air surrounded by the GO/CNF wall can act as an effective thermal insulation, reducing the heat loss at the top. This example of 3D printing to create an integrated stacking of three different aerogels provides a new method to efficiently convert sunlight energy into steam, which may promote its use in areas such as desalination.

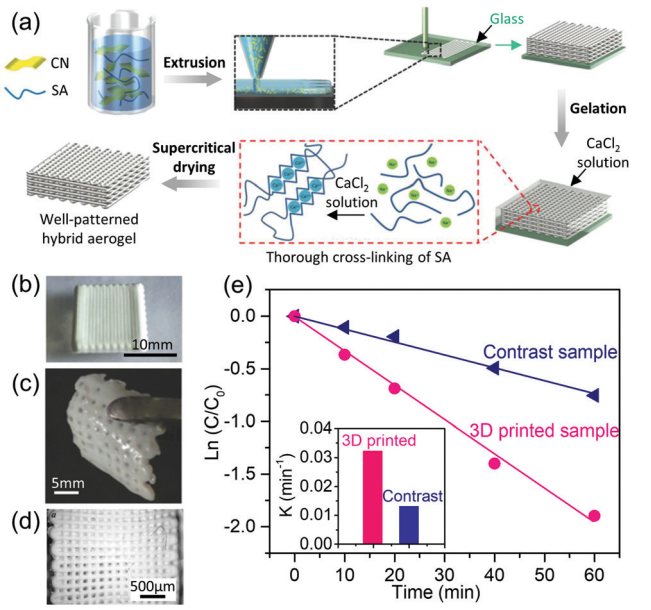

Fig. 34 Photocatalysis application of printed Au/CN-SA aerogels. (a) Schematic illustration of the aerogel fabrication/printing process. Photographs of (b) a structure printed directly in air, (c) the printed structure after thorough cross-linking in a $CaCl_2$ solution, and (d) supercritically dried aerogel. (e) Comparison of the photocatalytic methylene blue degradation rates ($\lambda > 420$ nm) of the 3D-printed structure and non-printed contrast aerogel sample. Adapted with permission from ref. 183. Copyright 2018 WILEY-VCH.

5.6.2 Photocatalysis application. 3D printed aerogel membranes with patterned macrostructures have also been used for solar wastewater remediation (Fig. 34).[183] The extrusion printed Au/g-C_3N_4-sodium alginate (Au/CN-SA) aerogel shows excellent photodegradation activity of methylene blue, reaching an efficiency of more than 93% in 60 minutes; this is 1.5 times more active than a control sample of non-printed aerogel (Fig. 34e). The authors propose that the performance enhancement is due to the fast liquid flow and efficient dye diffusion facilitated by the ordered 3D printed macropore structure. These examples all show that printing technologies bring clear advantages in device fabrication and integration, and specific performance improvement in the application of aerogels in photovoltaics and photocatalysis.

6. Conclusions and perspectives

6.1 Research perspectives: challenges and future directions

In the past 5 years, significant breakthroughs have been achieved in combining aerogels and advanced printing technologies, leading to the realization of a variety of printed aerogels with a wide range of functionalities. Indeed, this has clearly brought a great improvement in aerogel properties and application-specific adaptability, considerably expanding their scope. However, this field is still in its infancy and great strides are needed before they can be widely accepted and exploited on an industrial scale as an additive manufacturing technology. In this section, we summarize the research achievements, and present our opinion on the key challenges that need to be

overcome in the near- to mid-term from the perspectives of design and ink formulation, printing process, and application.

6.1.1 Design and ink formulation. Considerable recent progress has been made in the formulation of inks for printed aerogels. Examples include a new type of photocurable siloxane precursor designed for light-based printing,[206] SiO_2-based[179,207] and RF[180] sol prepared from the traditional molecule-derived route, and a variety of ink formulation approaches with 1D (Table 4) and 2D (Table 5) nanomaterials. Nevertheless, the range of suitable material types in these formulations is still limited, and faces a series of following challenges:

(i) Design and synthesis of precursors: For printing oxide aerogels from molecule-derived formulation, the types of aerogel precursors that have been studied thus far are very few, and are limited to only SiO_2-based precursors. New types of precursors and chemical structures need to be designed and synthesized for printing other materials and oxides such as polymers, Al_2O_3 and ZrO_2.

For photocurable printed aerogels, the design and synthesis of new precursor materials containing both photocurable groups and hydrolysable polycondensation groups are required.

For the formulation of inks using the nanomaterial-derived route, another important research direction is the development of inexpensive material synthesis strategies such that the materials can be directly used for ink preparation without any purification and other processes.

(ii) Standardization of ink formulation: Generally, the lower the target aerogel density, the lower the concentration of corresponding materials in the ink, and consequently, the ink viscosity (and *vice versa*). To meet various printing requirements and wide target application performance (such as a wide density range), designing and synthesizing inks with appropriate rheological properties to fit different printing technologies has always been a difficult research challenge. For example, 3D extrusion requires inks not only with suitable viscosity but also with shear-thinning behaviour to ensure smooth extrusion and self-supported filaments after printing. This can be addressed by introducing different ink additives. Rapid gelation formulations through light excitation, gas reaction, and liquid bath are also promising means to address this issue. However, these approaches are mostly empirically derived and do not currently have a general understanding or standardized protocol. Such universal criterion for extrusion ink formulation can considerably simplify this step.

(iii) Design of hierarchically porous structures: For applications such as tissue engineering and catalysis, pore size gradient and hierarchical distribution is critical to reconcile and coordinate two competing properties of volume utilization rate and mass transfer.[289,359] For 3D printing aerogel scaffolds, the pore structure of the printed aerogel consists of the nanopores of the aerogel itself and the voids between the printed filament structures (*i.e.*, pores above the micrometer range). The design and optimization of these pore structures, including their pore size hierarchy and proportions are important determinants of the aerogel performance. In spite of this, very limited research in this area has been carried out thus far. For specific applications, conceiving the hierarchically ideal pore structure through theoretical calculations,[289] then adjusting the print parameters, ink formulation, and gelation process to realize the designed pore structure and to verify mass transfer and related performance would be a game changer for the aerogel family of materials.

(iv) Strengthening of aerogel structure: Since aerogels are low-density, high-porosity materials, their mechanical strength is very low. For the case of layer by layer 3D printing, additional structural weakness may appear at the interface between the layers. The traditional method of reinforcement is to add fibres to form a composite material. In the field of printing, this may lead to new challenges in terms of ink rheology and printability. Therefore, understanding the effect of reinforcements, and the design of skeleton crosslinking through chemical reactions while maintaining the print performance, could form an important research direction. Adding short fibres or introducing special supramolecular interaction or dynamic covalent bond linking between the printed layers may address this, and improve the *Z*-direction strength. This could offer huge flexibility in ink formulation for printed aerogels.

6.1.2 Printing process. Thus far, a variety of printing technologies for aerogels have been developed and verified, such as inkjet, screen, light-based, 3D extrusion printing, and 3D printed templates. On the printed shape, aerogel microspheres, films, patterns, complex shapes, and 3D scaffolds have been successfully printed, breaking the boundaries of traditional machining or mould shaping methods. Despite these achievements, there are still some significant challenges.

(i) Printing of fine and intricate structures: Certain applications demand extremely strict size and resolution, and require the basic structural unit to be sufficiently small. For example, tissue engineering requires very high print dimensional accuracy to mimic the environment of the cell.[360] In addition to the dimensional accuracy, the availability of printing complex structures to achieve the best mechanical strength is also an important prerequisite for structural design.[361] Since 3D extrusion printing of aerogels requires the use of a slurry in a semi-gel state, controlling the dimensional accuracy of printing is very challenging. The size of the extrusion nozzle and the step resolution of the stages, also directly affects the print dimensions and accuracy. However, reducing the nozzle diameter may not always offer a solution as narrower nozzles are prone to clogging when nanomaterial derived inks are used. Although PmSLA 3D printing has been used to demonstrate print resolutions down to 10 microns, this has only been demonstrated on GO inks.[244] Printing aerogels with high-resolution and intricate structures still remains as one of the key research challenges. To this end, research advances in two-photon polymerization could allow achieving print resolutions as fine as 100 nm.[360]

(ii) Exploitable aerogel materials: The majority of the printed aerogels have focused on nanomaterial-derived inks such as 1D CNF or CNC (Table 4) and 2D nanosheets (such as GO, Table 5). Formulation of molecule- (such as for Al_2O_3, ZrO_2) or 0D nanoparticle- (such as metal, non-oxide ceramics) derived inks is less common. This is, in our opinion, primarily due to the

challenges involved in ink formulation. For example, control of the cross-linking degree of Al_2O_3 or ZrO_2 precursors, and therefore the viscosity, is more difficult than that of the precursors of SiO_2. The time window of printability is also shorter. Similarly, the 0D nanoparticle-derived inks (such as metal and non-oxide ceramics) may struggle to form a solid structure after the binder is removed as the particles do not entangle like 1D nanofibres or 2D nanosheets. The investigation into these materials is critical to expand the application scope of aerogels. Indeed, the huge potential of these materials for high temperature catalysis or support (Al_2O_3, Pt, SiC, *etc.*), and electromagnetic shielding and energy devices (*e.g.*, MXene) make them worth exploring.

(iii) Improving the print speed: The efficiencies of inkjet or screen printing for aerogel microspheres or films are somewhat acceptable. However, for 3D printing such as light- or extrusion-based techniques, the print speed and overall print efficiency are low for mass production. Light-based 3D printing usually has a very low print speed of only a few millimetres per hour in the vertical direction,[142] and is limited by the rheology of the inks. The print-head movement speed in extrusion-based 3D printing is usually less than 20 mm s^{-1} (Table 7). These are unacceptable for industrial scale production. Therefore, relevant research in improving the efficiency of 3D printing of aerogels is very important towards their industrial exploitation. The development of new printing methods, such as multi-nozzle, multi-material printing may greatly increase the production efficiency.[362] For light-based printing, computed axial lithography[143] or DLP assisted by continuous liquid interface production[142] could be used. However, considerable challenges in ink formulation with these photocurable resins and aerogel precursors remain, and require extensive investigation.

6.1.3 Application. As discussed above, example applications of aerogel printing include inkjet printed aerogel microspheres for drug delivery, and intricate and customised 3D architectures for thermal insulations,[179] supercapacitors,[21] batteries,[218] TENGs,[228] catalysis,[247] and even tissue engineering.[22] The motivations for those examples are typically, either to achieve superior performance, or to conquer the difficulty of shaping and integration that cannot be addressed by the traditional methods. However, from the perspective of practical applications, these developments are still very preliminary and imperfect. We believe that the near and mid-term challenges in these areas are:

(i) Comprehensive testing of printed aerogels: Printed aerogels clearly exhibit advantages in both mechanism and performance parameters in a wide range of application areas. However, for printed aerogel technologies to be adopted in industrial production for commercial applications, in-depth research into long-term performance and stability is needed, in particular, the changes in microstructure under realistic operating conditions, performance degradation rates, and their causes. In addition, the toxicity, health effects, and degradation of printed aerogels are also subjects that need close investigation, especially for tissue engineering and drug delivery.

(ii) Standardization of design and processing: the use of printing technologies can greatly improve the flexibility of design and allow customization and quick realization of prototypes. However, the presence of multiple design software, materials, printing and drying methods, and application fields, without standardization, is a hindrance towards their practical use. To serve a wider range of applications, we believe that it is necessary to learn from the experience of industrialized large-scale production, and standardize the design software, ink, process, testing methods, product performance, and protective measures for handlers to achieve complete and comprehensive quality control, ensuring continuity, repeatability and unity of production.

The above research perspectives and directions involve multiple disciplines and require strengthening the relationship not only between different branches of academia (such as experts in software and hardware, chemistry, chemical engineering, materials, environment, bioengineering, medicine, and health and safety), but also between industry and academia. This would promote joint interdisciplinary research and accelerate the transfer of knowledge and expertise from the laboratory to the pilot scale, and then to large-scale industrial production to serve industrial progress, economic development, and environmental and societal wellbeing.

6.2 Concluding remarks

The world of aerogels is exciting and fascinating. Apart from the mature thermal insulation industry, research and applications of aerogels have thrived in the past decade. From thermal insulation to energy and biotechnology applications, the social and economic impact of these porous solids, in our opinion, will become increasingly apparent in the coming years. However, in combination with the rapidly progressing additive manufacturing technologies, printed aerogels have only just begun to appear in the past 5 years. Indeed, recent research efforts and attempts in this direction already indicate great potential in many fields of applications and new market opportunities by overcoming the limitations of current aerogel materials. This statement is especially relevant to processing. For example, the unique designs of macrostructures such as minimum-surface Schwarts, Gyroid, and Diamond structures could be efficiently realized by 3D printing to fine-tune and improve application-specific aerogel properties. Therefore, in spite of the future technological challenges discussed above, we are convinced that the adoption of printing technologies could herald a new generation of low-cost, customizable, and adaptable aerogels that could potentially create new functionalities and boost the existing application areas, in particular, in energy, sensing, and bio-medical fields.

Conflicts of interest

There are no conflicts to declare.

Acknowledgements

J. Z. Feng, J. Feng, and L. Wang acknowledge financial support from the National Natural Science Foundation of China

(51712360). B. L. Su thanks the Program for Changjiang Scholars and Innovative Research Team in University (IRT_15R52) of the Ministry of Education, China, the National Natural Science Foundation of China (U1663225), the 111 Project (Grant No. B20002) from the Ministry of Science and Technology and the Ministry of Education, China. T. Hasan and O. Ogbeide acknowledges support from the Engineering and Physical Sciences Research Council (EP/L016087/1) and Alphasense Limited, United Kingdom.

References

1 N. Shaari and S. K. Kamarudin, *Int. J. Energy Res.*, 2019, **43**, 2447–2467.
2 H. Maleki and N. Hüsing, *Appl. Catal., B*, 2018, **221**, 530–555.
3 J. Yang, Y. Li, Y. Zheng, Y. Xu, Z. Zheng, X. Chen and W. Liu, *Small*, 2019, **15**, 1902826.
4 H. Maleki, *Chem. Eng. J.*, 2016, **300**, 98–118.
5 X. Xu, Q. Zhang, M. Hao, Y. Hu, Z. Lin, L. Peng, T. Wang, X. Ren, C. Wang, Z. Zhao, C. Wan, H. Fei, L. Wang, J. Zhu, H. Sun, W. Chen, T. Du, B. Deng, G. J. Cheng, I. Shakir, C. Dames, T. S. Fisher, X. Zhang, H. Li, Y. Huang and X. Duan, *Science*, 2019, **363**, 723–727.
6 S. Zhao, W. J. Malfait, N. Guerrero-Alburquerque, M. M. Koebel and G. Nyström, *Angew. Chem., Int. Ed*, 2018, **57**, 7580–7608.
7 Y. Kebukawa, K. Okudaira, H. Yabuta, S. Hasegawa, M. Tabata, Y. Furukawa, M. Ito, A. Nakato, A. L. David Kilcoyne, K. Kobayashi, S. I. Yokobori, E. Imai, Y. Kawaguchi, H. Yano and A. Yamagishi, *Geochem. J.*, 2019, **53**, 53–67.
8 S. B. Riffat and G. Qiu, *Int. J. Low-Carbon Technol.*, 2013, **8**, 1–6.
9 I. Smirnova and P. Gurikov, *Annu. Rev. Chem. Biomol. Eng.*, 2017, **8**, 307–334.
10 N. Bheekhun, A. R. A. Talib and M. R. Hassan, *Adv. Mater. Sci. Eng.*, 2013, 406065.
11 K. Dong, X. Peng and Z. L. Wang, *Adv. Mater.*, 2020, **32**, 1902549.
12 J. D. Prince, *J. Electron. Resour. Med. Libr.*, 2014, **11**, 39–45.
13 Manufacturing - The third industrial revolution | Leaders | The Economist, https://www.economist.com/leaders/2012/04/21/the-third-industrial-revolution, accessed 28 March 2020.
14 A. Ambrosi and M. Pumera, *Chem. Soc. Rev.*, 2016, **45**, 2740–2755.
15 B. Bhushan and M. Caspers, *Microsyst. Technol.*, 2017, **23**, 1117–1124.
16 A. Zhakeyev, P. Wang, L. Zhang, W. Shu, H. Wang and J. Xuan, *Adv. Sci.*, 2017, **4**, 1700187.
17 W. Gao, Y. Zhang, D. Ramanujan, K. Ramani, Y. Chen, C. B. Williams, C. C. L. Wang, Y. C. Shin, S. Zhang and P. D. Zavattieri, *Comput. Des.*, 2015, **69**, 65–89.
18 C. Zhu, T. Y. J. Han, E. B. Duoss, A. M. Golobic, J. D. Kuntz, C. M. Spadaccini and M. A. Worsley, *Nat. Commun.*, 2015, **6**, 6962.
19 S. Chandrasekaran, B. Yao, T. Liu, W. Xiao, Y. Song, F. Qian, C. Zhu, E. B. Duoss, C. M. Spadaccini, Y. Li and M. A. Worsley, *Mater. Horiz.*, 2018, **5**, 1166–1175.
20 C. Zhu, T. Liu, F. Qian, T. Y. J. Han, E. B. Duoss, J. D. Kuntz, C. M. Spadaccini, M. A. Worsley and Y. Li, *Nano Lett.*, 2016, **16**, 3448–3456.
21 B. Yao, S. Chandrasekaran, J. Zhang, W. Xiao, F. Qian, C. Zhu, E. B. Duoss, C. M. Spadaccini, M. A. Worsley and Y. Li, *Joule*, 2019, **3**, 459–470.
22 D. Sun, W. Liu, A. Tang, F. Guo and W. Xie, *Soft Matter*, 2019, **15**, 8092–8101.
23 W. Chen, Y. Xu, Y. Liu, Z. Wang, Y. Li, G. Jiang, X. Mo and G. Zhou, *Mater. Des.*, 2019, **179**, 107886.
24 S. S. Kistler, *Nature*, 1931, **127**, 741.
25 J. Alemán, A. V. Chadwick, J. He, M. Hess, K. Horie, R. G. Jones, P. Kratochvíl, I. Meisel, I. Mita, G. Moad, S. Penczek and R. F. T. Stepto, *Pure Appl. Chem.*, 2007, **79**, 1801–1829.
26 A. C. Pierre and G. M. Pajonk, *Chem. Rev.*, 2002, **102**, 4243–4265.
27 C. Ziegler, A. Wolf, W. Liu, A. K. Herrmann, N. Gaponik and A. Eychmüller, *Angew. Chem., Int. Ed*, 2017, **56**, 13200–13221.
28 ''Aerogel.org'' What is Aerogel? http://www.aerogel.org/?p=3, accessed 21 May 2020.
29 S. M. Jung, H. Y. Jung, M. S. Dresselhaus, Y. J. Jung and J. Kong, *Sci. Rep.*, 2012, **2**, 849.
30 D. Shin, J. Kim, C. Kim, K. Bae, S. Baek, G. Kang, Y. Urzhumov, D. R. Smith and K. Kim, *Nat. Commun.*, 2017, **8**, 16090.
31 L. Wang, J. Feng, Y. Jiang, S. Zhang, L. Li and J. Feng, *J. Sol-Gel Sci. Technol.*, 2020, **94**, 88–97.
32 F. Cao, L. Ren and X. Li, *RSC Adv.*, 2015, **5**, 18025–18028.
33 G. O. Kiselev, A. P. Kiseleva, D. A. Ilatovskii, E. D. Koshevaya, D. A. Nazarovskaia, D. S. Gets, V. V. Vinogradov, P. V. Krivoshapkin and E. F. Krivoshapkina, *Chem. Commun.*, 2019, **55**, 8174–8177.
34 Y. Kong, X. D. Shen and S. Cui, *Mater. Lett.*, 2014, **117**, 192–194.
35 A. E. Gash, T. M. Tillotson, J. H. Satcher Jr, L. W. Hrubesh and R. L. Simpson, *J. Non. Cryst. Solids*, 2001, **285**, 22–28.
36 Y. J. Huang, Y. J. Lin, H. J. Chien, Y. F. Lin and K. C. Ho, *Nanoscale*, 2019, **11**, 12507–12516.
37 H. Bi, I. W. Chen, T. Lin and F. Huang, *Adv. Mater.*, 2015, **27**, 5943–5949.
38 M. B. Bryning, D. E. Milkie, M. F. Islam, L. A. Hough, J. M. Kikkawa and A. G. Yodh, *Adv. Mater.*, 2007, **19**, 661–664.
39 M. A. Worsley, S. O. Kucheyev, J. H. Satcher, A. V. Hamza and T. F. Baumann, *Appl. Phys. Lett.*, 2009, **94**, 073115.
40 X. Zhao, W. Yao, W. Gao, H. Chen and C. Gao, *Adv. Mater.*, 2017, **29**, 1701482.
41 Y. Jiang, Z. Xu, T. Huang, Y. Liu, F. Guo, J. Xi, W. Gao and C. Gao, *Adv. Funct. Mater.*, 2018, **28**, 1707024.

42 R. W. Pekala, *J. Mater. Sci.*, 1989, **24**, 3221–3227.
43 M. Aghabararpour, M. Mohsenpour and S. Motahari, *Mater. Res. Express*, 2019, **6**, 075059.
44 Z. Saadatnia, S. G. Mosanenzadeh, E. Esmailzadeh and H. E. Naguib, *Sci. Rep.*, 2019, **9**, 1370.
45 J. Lyu, Z. Liu, X. Wu, G. Li, D. Fang and X. Zhang, *ACS Nano*, 2019, **13**, 2236–2245.
46 Y. Xiao, L. Li, S. Zhang, J. Feng, Y. Jiang and J. Feng, *J. Mater. Sci.*, 2019, **54**, 12951–12961.
47 P. Tseng, B. Napier, S. Zhao, A. N. Mitropoulos, M. B. Applegate, B. Marelli, D. L. Kaplan and F. G. Omenetto, *Nat. Nanotechnol.*, 2017, **12**, 474–480.
48 Z. Li, L. Zhong, T. Zhang, F. Qiu, X. Yue and D. Yang, *ACS Sustainable Chem. Eng.*, 2019, **7**, 9984–9994.
49 S. Takeshita, A. Sadeghpour, W. J. Malfait, A. Konishi, K. Otake and S. Yoda, *Biomacromolecules*, 2019, **20**, 2051–2057.
50 R. Rodríguez-Dorado, C. López-Iglesias, C. García-González, G. Auriemma, R. Aquino and P. Del Gaudio, *Molecules*, 2019, **24**, 1049.
51 G. W. Nyce, J. R. Hayes, A. V. Hamza and J. H. Satcher, *Chem. Mater.*, 2007, **19**, 344–346.
52 F. Qian, A. Troksa, T. M. Fears, M. H. Nielsen, A. J. Nelson, T. F. Baumann, S. O. Kucheyev, T. Y.-J. J. Han and M. Bagge-Hansen, *Nano Lett.*, 2020, **20**, 131–135.
53 M. Georgi, B. Klemmed, A. Benad and A. Eychmüller, *Mater. Chem. Front.*, 2019, **3**, 1586–1592.
54 P. Yan, E. Brown, Q. Su, J. Li, J. Wang, C. Xu, C. Zhou and D. Lin, *Small*, 2017, **13**, 1701756.
55 L. W. Yap, S. Gong, Y. Tang, Y. Zhu and W. Cheng, *Sci. Bull.*, 2016, **61**, 1624–1630.
56 M. Rousseas, A. P. Goldstein, W. Mickelson, M. A. Worsley, L. Woo and A. Zettl, *ACS Nano*, 2013, **7**, 8540–8546.
57 L. Su, M. Li, H. Wang, M. Niu, D. Lu and Z. Cai, *ACS Appl. Mater. Interfaces*, 2019, **11**, 15795–15803.
58 D. Lu, L. Su, H. Wang, M. Niu, L. Xu, M. Ma, H. Gao, Z. Cai and X. Fan, *ACS Appl. Mater. Interfaces*, 2019, **11**, 45338–45344.
59 X. Zhang, R. Lv, A. Wang, W. Guo, X. Liu and J. Luo, *Angew. Chem., Int. Ed.*, 2018, **57**, 15028–15033.
60 L. Korala, J. R. Germain, E. Chen, I. R. Pala, D. Li and S. L. Brock, *Inorg. Chem. Front.*, 2017, **4**, 1451–1457.
61 J. L. Mohanan, I. U. Arachchige and S. L. Brock, *Science*, 2005, **307**, 397–400.
62 A. Freytag, S. Sánchez-Paradinas, S. Naskar, N. Wendt, M. Colombo, G. Pugliese, J. Poppe, C. Demirci, I. Kretschmer, D. W. Bahnemann, P. Behrens and N. C. Bigall, *Angew. Chem., Int. Ed*, 2016, **55**, 1200–1203.
63 V. Sayevich, B. Cai, A. Benad, D. Haubold, L. Sonntag, N. Gaponik, V. Lesnyak and A. Eychmüller, *Angew. Chem., Int. Ed.*, 2016, **55**, 6334–6338.
64 R. Wendt, B. Märker, A. Dubavik, A.-K. Herrmann, M. Wollgarten, Y. P. Rakovich, A. Eychmüller, K. Rademann and T. Hendel, *J. Mater. Chem. C*, 2017, **5**, 10251–10259.
65 B. Cai, K. Akkiraju, W. P. Mounfield, Z. Wang, X. Li, B. Huang, S. Yuan, D. Su, Y. Román-Leshkov and Y. Shao-Horn, *Chem. Mater.*, 2019, **31**, 9422–9429.
66 A. E. Aliev, J. Oh, M. E. Kozlov, A. A. Kuznetsov, S. Fang, A. F. Fonseca, R. Ovalle, M. D. Lima, M. H. Haque, Y. N. Gartstein, M. Zhang, A. A. Zakhidov and R. H. Baughman, *Science*, 2009, **323**, 1575–1578.
67 H. Im, T. Kim, H. Song, J. Choi, J. S. Park, R. Ovalle-Robles, H. D. Yang, K. D. Kihm, R. H. Baughman, H. H. Lee, T. J. Kang and Y. H. Kim, *Nat. Commun.*, 2016, **7**, 10600.
68 Y. L. Li, I. A. Kinloch and A. H. Windle, *Science*, 2004, **304**, 276–278.
69 J. T. Korhonen, P. Hiekkataipale, J. Malm, M. Karppinen, O. Ikkala and R. H. A. Ras, *ACS Nano*, 2011, **5**, 1967–1974.
70 Y. Song, B. Li, S. Yang, G. Ding, C. Zhang and X. Xie, *Sci. Rep.*, 2015, **5**, 10337.
71 F. Matter, A. L. Luna and M. Niederberger, *Nano Today*, 2020, **30**, 100827.
72 T. Linhares, M. T. Pessoa De Amorim and L. Durães, *J. Mater. Chem. A*, 2019, **7**, 22768–22802.
73 F. Peng, Y. Jiang, J. Feng, L. Li, H. Cai and J. Feng, *J. Eur. Ceram. Soc.*, 2020, **40**, 2480–2488.
74 Z. Zhao, D. Chen and X. Jiao, *J. Phys. Chem. C*, 2007, **111**, 18738–18743.
75 Y. Nakanishi, Y. Hara, W. Sakuma, T. Saito, K. Nakanishi and K. Kanamori, *ACS Appl. Nano Mater.*, 2020, **3**, 49–54.
76 Y. Xiao, L. Li, S. Zhang, J. Feng, Y. Jiang and J. Feng, *Macromol. Mater. Eng.*, 2019, 1900137.
77 S. Zhang, J. Feng, J. Feng and Y. Jiang, *Chem. Eng. J.*, 2017, **309**, 700–707.
78 S. Bag, P. N. Trikalitis, P. J. Chupas, G. S. Armatas and M. G. Kanatzidis, *Science*, 2007, **317**, 490–493.
79 K. S. Subrahmanyam, D. Sarma, C. D. Malliakas, K. Polychronopoulou, B. J. Riley, D. A. Pierce, J. Chun and M. G. Kanatzidis, *Chem. Mater.*, 2015, **27**, 2619–2626.
80 P. D. Brown, S. K. Gill and L. J. Hope-Weeks, *J. Mater. Chem.*, 2011, **21**, 4204–4208.
81 B. J. Clapsaddle, B. Neumann, A. Wittstock, D. W. Sprehn, A. E. Gash, J. H. Satcher, R. L. Simpson and M. Bäumer, *J. Sol-Gel Sci. Technol.*, 2012, **64**, 381–389.
82 J. Mrowiec-Białoń, A. B. Jarzębski, L. Pajak, Z. Olejniczak and M. Gibas, *Langmuir*, 2004, **20**, 10389–10393.
83 D. Levy and M. Zayat, *The Sol-Gel Handbook*, 2015, vol. 2, pp. 519–574.
84 S. Karamikamkar, H. E. Naguib and C. B. Park, *Adv. Colloid Interface Sci.*, 2020, **276**, 102101.
85 S. D. Bhagat, H. Hirashima and A. Venkateswara Rao, *J. Mater. Sci.*, 2007, **42**, 3207–3214.
86 D. B. Mahadik, A. V. Rao, P. B. Wagh and S. C. Gupta, *AIP Conference Proceedings*, American Institute of PhysicsAIP, 2013, vol. 1536, pp. 553–554.
87 Z. Shao, F. Luo, X. Cheng and Y. Zhang, *Mater. Chem. Phys.*, 2013, **141**, 570–575.
88 F. Rechberger and M. Niederberger, *Nanoscale Horiz.*, 2017, **2**, 6–30.
89 C. A. Saez Cabezas, G. K. Ong, R. B. Jadrich, B. A. Lindquist, A. Agrawal, T. M. Truskett and D. J. Milliron, *Proc. Natl. Acad. Sci. U. S. A.*, 2018, **115**, 8925–8930.

90 D. Wen, W. Liu, D. Haubold, C. Zhu, M. Oschatz, M. Holzschuh, A. Wolf, F. Simon, S. Kaskel and A. Eychmüller, *ACS Nano*, 2016, **10**, 2559–2567.
91 R. Du, Y. Hu, R. Hübner, J. O. Joswig, X. Fan, K. Schneider and A. Eychmüller, *Sci. Adv.*, 2019, **5**, eaaw4590.
92 L. Dong, W. Wang, J. Chen, X. Ding, B. Fang, X. Miao, Y. Liu, F. Yu, H. Xin and X. Wang, *Biomater. Sci.*, 2018, **6**, 2312–2315.
93 H. Zhang, S. Lyu, X. Zhou, H. Gu, C. Ma, C. Wang, T. Ding, Q. Shao, H. Liu and Z. Guo, *J. Colloid Interface Sci.*, 2019, **536**, 245–251.
94 H. Yang, Z. Li, G. Sun, X. Jin, B. Lu, P. Zhang, T. Lin and L. Qu, *Adv. Funct. Mater.*, 2019, **29**, 1901917.
95 G. Markevicius, R. Ladj, P. Niemeyer, T. Budtova and A. Rigacci, *J. Mater. Sci.*, 2017, **52**, 2210–2221.
96 P. R. Aravind, P. Shajesh, G. D. Soraru and K. G. K. Warrier, *J. Sol-Gel Sci. Technol.*, 2010, **54**, 105–117.
97 M. A. Einarsrud, S. Haereid and V. Wittwer, *Sol. Energy Mater. Sol. Cells*, 1993, **31**, 341–347.
98 S. S. Prakash, C. J. Sankaran, A. J. Hurd and S. M. Rao, *Nature*, 1995, **374**, 439–443.
99 D. Klvana, J. Chaouki, M. Repellin-Lacroix, G. Pajonk, M. Repellin-lacroix and G. Pajonk, *J. Phys., Colloq.*, 1989, **50**, 29–32.
100 X. Zhang, Z. Sui, B. Xu, S. Yue, Y. Luo, W. Zhan and B. Liu, *J. Mater. Chem.*, 2011, **21**, 6494–6497.
101 M. J. Oh and P. J. Yoo, *Korean J. Chem. Eng.*, 2020, **37**, 189–208.
102 H. Sun, Z. Xu and C. Gao, *Adv. Mater.*, 2013, **25**, 2554–2560.
103 Y. Si, X. Wang, C. Yan, L. Yang, J. Yu and B. Ding, *Adv. Mater.*, 2016, **28**, 9512–9518.
104 Z. Wang, R. Wei, J. Gu, H. Liu, C. Liu, C. Luo, J. Kong, Q. Shao, N. Wang, Z. Guo and X. Liu, *Carbon*, 2018, **139**, 1126–1135.
105 W. Gao, N. Zhao, W. Yao, Z. Xu, H. Bai and C. Gao, *RSC Adv.*, 2017, **7**, 33600–33605.
106 R. Bian, G. He, W. Zhi, S. Xiang, T. Wang and D. Cai, *J. Mater. Chem. C*, 2019, **7**, 474–478.
107 M. Peng, Z. Wen, L. Xie, J. Cheng, Z. Jia, D. Shi, H. Zeng, B. Zhao, Z. Liang, T. Li and L. Jiang, *Adv. Mater.*, 2019, **31**, 1902930.
108 M. Han, X. Yin, K. Hantanasirisakul, X. Li, A. Iqbal, C. B. Hatter, B. Anasori, C. M. Koo, T. Torita, Y. Soda, L. Zhang, L. Cheng and Y. Gogotsi, *Adv. Opt. Mater.*, 2019, **7**, 1900267.
109 Q. Zhang, F. Zhang, S. P. Medarametla, H. Li, C. Zhou and D. Lin, *Small*, 2016, **12**, 1702–1708.
110 S. Liao, T. Zhai and H. Xia, *J. Mater. Chem. A*, 2016, **4**, 1068–1077.
111 P. Paraskevopoulou, D. Chriti, G. Raptopoulos and G. C. Anyfantis, *Materials*, 2019, **12**, 1543.
112 Z. Xu, Y. Zhang, P. Li and C. Gao, *ACS Nano*, 2012, **6**, 7103–7113.
113 Z. Xu, L. Peng, Y. Liu, Z. Liu, H. Sun, W. Gao and C. Gao, *Chem. Mater.*, 2017, **29**, 319–330.
114 G. Li, G. Hong, D. Dong, W. Song and X. Zhang, *Adv. Mater.*, 2018, **30**, 1801754.
115 X. Y. Sun, W. B. Luo, J. Meng, X. Qing, W. Y. Fu, Y. Shuai and C. G. Wu, *Sens. Actuators, A*, 2015, **228**, 69–74.
116 A. S. Gaikwad, S. A. Gupta and A. M. Mahajan, *Mater. Res. Express*, 2016, **3**, 086403.
117 X. Wang, Y. Zhang, J. Luo, D. Wang, H. Gao, J. Zhang, Y. Xing, Z. Yang, H. Cao and W. He, *New J. Chem.*, 2018, **42**, 6525–6531.
118 M. A. B. Meador, E. J. Malow, R. Silva, S. Wright, D. Quade, S. L. Vivod, H. Guo, J. Guo and M. Cakmak, *ACS Appl. Mater. Interfaces*, 2012, **4**, 536–544.
119 L. S. White, D. R. Echard, M. F. Bertino, X. Gao, S. Donthula, N. Leventis, N. Shukla, J. Kośny, S. Saeed and K. Saoud, *Transl. Mater. Res.*, 2016, **3**, 015002.
120 G. Hu, J. Kang, L. W. T. Ng, X. Zhu, R. C. T. Howe, C. G. Jones, M. C. Hersam and T. Hasan, *Chem. Soc. Rev.*, 2018, **47**, 3265–3300.
121 L. W. T. Ng, G. Hu, R. C. T. Howe, X. Zhu, Z. Yang, C. G. Jones, T. Hasan, L. W. T. Ng, G. Hu, R. C. T. Howe, X. Zhu, Z. Yang, C. G. Jones and T. Hasan, *Printing of Graphene and Related 2D Materials*, Springer International Publishing, 2018, pp. 103–134.
122 A. Moya, G. Gabriel, R. Villa and F. Javier del Campo, *Curr. Opin. Electrochem.*, 2017, **3**, 29–39.
123 A. Kamyshny and S. Magdassi, *Chem. Soc. Rev.*, 2019, **48**, 1712–1740.
124 T. D. Ngo, A. Kashani, G. Imbalzano, K. T. Q. Nguyen and D. Hui, *Composites, Part B*, 2018, **143**, 172–196.
125 P. Wu, J. Wang and X. Wang, *Autom. Constr.*, 2016, **68**, 21–31.
126 2012, ASTM International F2792-12a.
127 A. J. Pinkerton, *Opt. Laser Technol.*, 2016, **78**, 25–32.
128 T. DebRoy, T. Mukherjee, J. O. Milewski, J. W. Elmer, B. Ribic, J. J. Blecher and W. Zhang, *Nat. Mater.*, 2019, **18**, 1026–1032.
129 A. Nycz, M. W. Noakes, B. Richardson, A. Messing, B. Post, J. Paul, J. Flamm and L. Love, *Solid Freeform Fabrication 2017*, Proceedings of the 28th Annual International, 2017, pp. 24–33.
130 R. J. Mobbs, M. Coughlan, R. Thompson, C. E. Sutterlin and K. Phan, *J. Neurosurg. Spine*, 2017, **26**, 513–518.
131 A. Al-Halhouli, L. Al-Ghussain, S. El Bouri, H. Liu and D. Zheng, *Polymers*, 2019, **11**, 1518.
132 A. Al-Halhouli, L. Al-Ghussain, S. El Bouri, F. Habash, H. Liu and D. Zheng, *Appl. Sci.*, 2020, **10**, 480.
133 T. Fiegl, M. Franke and C. Körner, *Opt. Laser Technol.*, 2019, **111**, 51–57.
134 J. H. Martin, B. D. Yahata, J. M. Hundley, J. A. Mayer, T. A. Schaedler and T. M. Pollock, *Nature*, 2017, **549**, 365–369.
135 Y. Zheng, Z. Z. He, J. Yang and J. Liu, *Sci. Rep.*, 2014, **4**, 4588.
136 S. Sun, X. Gan, Z. Wang, D. Fu, W. Pu and H. Xia, *Addit. Manuf.*, 2020, **33**, 101176.
137 C. Zhang, X. Lu, G. Fei, Z. Wang, H. Xia and Y. Zhao, *ACS Appl. Mater. Interfaces*, 2019, **11**, 44774–44782.
138 D. Lv, W. Chen, W. Shen, M. Peng, X. Zhang, R. Wang, L. Xu, W. Xu, W. Song and R. Tan, *Sens. Actuators, B*, 2019, **298**, 126890.

139 T. Chen, O. R. Bilal, K. Shea and C. Daraio, *Proc. Natl. Acad. Sci. U. S. A.*, 2018, **115**, 5698–5702.
140 J. H. Shin, J. H. Heo, S. Jeon, J. H. Park, S. Kim and H. W. Kang, *J. Hazard. Mater.*, 2019, **365**, 494–501.
141 D. A. Walker, J. L. Hedrick and C. A. Mirkin, *Science*, 2019, **366**, 360–364.
142 J. R. Tumbleston, D. Shirvanyants, N. Ermoshkin, R. Janusziewicz, A. R. Johnson, D. Kelly, K. Chen, R. Pinschmidt, J. P. Rolland, A. Ermoshkin, E. T. Samulski and J. M. DeSimone, *Science*, 2015, **347**, 1349–1352.
143 B. E. Kelly, I. Bhattacharya, H. Heidari, M. Shusteff, C. M. Spadaccini and H. K. Taylor, *Science*, 2019, **363**, 1075–1079.
144 H. Chen, X. Wang, F. Xue, Y. Huang, K. Zhou and D. Zhang, *J. Eur. Ceram. Soc.*, 2018, **38**, 5294–5300.
145 H. Zhang, Y. Yang, B. Liu and Z. Huang, *Ceram. Int.*, 2019, **45**, 10800–10804.
146 Y. de Hazan and D. Penner, *J. Eur. Ceram. Soc.*, 2017, **37**, 5205–5212.
147 K. Terrani, B. Jolly and M. Trammell, *J. Am. Ceram. Soc.*, 2020, **103**, 1575–1581.
148 S. A. Brinckmann, N. Patra, J. Yao, T. H. Ware, C. P. Frick and R. S. Fertig, *Adv. Eng. Mater.*, 2018, **20**, 1800593.
149 S. H. Park, M. Kaur, D. Yun and W. S. Kim, *Langmuir*, 2018, **34**, 10897–10904.
150 B. Furet, P. Poullain and S. Garnier, *Addit. Manuf.*, 2019, **28**, 58–64.
151 M. Rieu, M. Camara, G. Tournier, J. P. Viricelle, C. Pijolat, N. F. de Rooij and D. Briand, *Sens. Actuators, B*, 2016, **236**, 1091–1097.
152 F. Yang, V. Tadepalli and B. J. Wiley, *ACS Biomater. Sci. Eng.*, 2017, **3**, 863–869.
153 H.-W. Kang, S. J. Lee, I. K. Ko, C. Kengla, J. J. Yoo and A. Atala, *Nat. Biotechnol.*, 2016, **34**, 312–319.
154 L. Yu, Z. Fan, Y. Shao, Z. Tian, J. Sun and Z. Liu, *Adv. Energy Mater.*, 2019, **9**, 1901839.
155 J. W. Jung, J. S. Lee and D. W. Cho, *Sci. Rep.*, 2016, **6**, 21685.
156 B. Dutta and F. H. Sam Froes, *Titanium Powder Metallurgy: Science, Technology and Applications*, Elsevier Inc., 2015, pp. 447–468.
157 C. Gosselin, R. Duballet, P. Roux, N. Gaudillière, J. Dirrenberger and P. Morel, *Mater. Des.*, 2016, **100**, 102–109.
158 C. A. García-González, J. J. Uy, M. Alnaief and I. Smirnova, *Carbohydr. Polym.*, 2012, **88**, 1378–1386.
159 W. Stöber, A. Fink and E. Bohn, *J. Colloid Interface Sci.*, 1968, **26**, 62–69.
160 H. Cai, Y. Jiang, L. Li, J. Feng and J. Feng, *J. Sol-Gel Sci. Technol.*, 2019, **91**, 44–53.
161 A. G. Howard and N. H. Khdary, *Mater. Lett.*, 2007, **61**, 1951–1954.
162 C. Jiménez-Saelices, B. Seantier, B. Cathala and Y. Grohens, *Carbohydr. Polym.*, 2017, **157**, 105–113.
163 E. Başaran, T. Alp Arıcı, A. Özcan, Ö. Gök and A. S. Özcan, *J. Sol-Gel Sci. Technol.*, 2019, **89**, 458–472.
164 C. A. García-González and I. Smirnova, *J. Supercrit. Fluids*, 2013, **79**, 152–158.
165 Y. Wang, Y. Cui, Z. Shao, W. Gao, W. Fan, T. Liu and H. Bai, *Chem. Eng. J.*, 2020, **390**, 124623.
166 Z. Wang, H. Yang, Y. Li and X. Zheng, *ACS Appl. Mater. Interfaces*, 2020, **12**, 15726–15736.
167 I. Karadagli, B. Schulz, M. Schestakow, B. Milow, T. Gries and L. Ratke, *J. Supercrit. Fluids*, 2015, **106**, 105–114.
168 J. Mroszczok, B. Schulz, K. Wilsch, G. Frenzer, S. Kasper and G. Seide, *Mater. Today Proc.*, 2017, **4**, S244–S248.
169 B. Schulz, T. Meinert, D. Bierbüsse, M. Busen, N. Körtzinger, M. Stankowski and G. Seide, *Chem. Ing. Tech.*, 2016, **88**, 1501–1507.
170 J. Zhou and Y. Lo Hsieh, *Nano Energy*, 2020, **68**, 104305.
171 T. Xue, H. Yang, B. Shen, F. Li, M. Su, X. Hu, W. Liu and Y. Song, *J. Mater. Chem. C*, 2019, **7**, 6317–6322.
172 B. Huo, D. Jiang, X. Cao, H. Liang, Z. Liu, C. Li and J. Liu, *Carbon*, 2019, **142**, 13–19.
173 V. D. Phadtare, V. G. Parale, T. Kim, K. Y. Lee, S. Pathak and H. H. Park, *J. Alloys Compd.*, 2020, **823**, 153847.
174 L. Liu, Z. Cai, S. Lin and X. Hu, *ACS Appl. Nano Mater.*, 2018, **1**, 4910–4917.
175 J. Li, Y. Zhang, K. Ma, X. De Pan, C. X. Li, G. J. Yang and C. J. Li, *J. Therm. Spray Technol.*, 2018, **27**, 471–482.
176 V. C. F. Li, A. Mulyadi, C. K. Dunn, Y. Deng and H. J. Qi, *ACS Sustainable Chem. Eng.*, 2018, **6**, 2011–2022.
177 N. Teo, P. Joo, E. J. Amis and S. C. Jana, *ACS Appl. Polym. Mater.*, 2019, **1**, 1749–1756.
178 Y. Lin, F. Liu, G. Casano, R. Bhavsar, I. A. Kinloch and B. Derby, *Adv. Mater.*, 2016, **28**, 7993–8000.
179 S. Zhao, G. Siqueira, S. Drdova, D. Norris, C. Ubert, A. Bonnin, S. Galmarini, M. Ganobjak, Z. Pan, S. Brunner, G. Nyström, J. Wang, M. M. Koebel and W. J. Malfait, *Nature*, 2020, **584**, 387–392.
180 Y. Ge, T. Zhang, B. Zhou, H. Wang, Z. Zhang, J. Shen and A. Du, *J. Mater. Res.*, 2018, **33**, 2052–2061.
181 V. C. F. Li, C. K. Dunn, Z. Zhang, Y. Deng and H. J. Qi, *Sci. Rep.*, 2017, **7**, 8018.
182 F. Lübkemann, J. F. Miethe, F. Steinbach, P. Rusch, A. Schlosser, D. Zámbó, T. Heinemeyer, D. Natke, D. Zok, D. Dorfs and N. C. Bigall, *Small*, 2019, **15**, 1902186.
183 P. He, X. Tang, L. Chen, P. Xie, L. He, H. Zhou, D. Zhang and T. Fan, *Adv. Funct. Mater.*, 2018, **28**, 1801121.
184 B. A. García-Torres, A. Aguilar-Elguezabal, M. Román-Aguirre and L. Álvarez-Contreras, *Mater. Chem. Phys.*, 2016, **172**, 32–38.
185 F. Meng, Z. Dehouche, A. Nutasarin and G. R. Fern, *Int. J. Energy Res.*, 2018, **42**, 3915–3927.
186 X. Tang, H. Zhou, Z. Cai, D. Cheng, P. He, P. Xie, D. Zhang and T. Fan, *ACS Nano*, 2018, **12**, 3502–3511.
187 L. Wang, S. Chen, T. Shu and X. Hu, *ChemSusChem*, 2020, **13**, 1330–1353.
188 H. Maleki, L. Durães, C. A. García-González, P. del Gaudio, A. Portugal and M. Mahmoudi, *Adv. Colloid Interface Sci.*, 2016, **236**, 1–27.
189 S. M. S. Murshed and P. Estellé, *Renewable Sustainable Energy Rev.*, 2017, **76**, 1134–1152.
190 R. P. Chhabra, *Rheology of Complex Fluids*, Springer New York, 2010, pp. 3–34.

191 M. Zeng and Y. Zhang, *J. Mater. Chem. A*, 2019, **7**, 23301–23336.
192 M. R. Somalu, A. Muchtar, W. R. W. Daud and N. P. Brandon, *Renewable Sustainable Energy Rev.*, 2017, **75**, 426–439.
193 H. W. Lin, C. P. Chang, W. H. Hwu and M. Der Ger, *J. Mater. Process. Technol.*, 2008, **197**, 284–291.
194 R. Durairaj, A. Seman and N. N. Ekere, in ESTC 2006 - 1st Electronics Systemintegration Technology Conference, Institute of Electrical and Electronics Engineers Inc., 2006, pp. 347–353.
195 M. Wei, F. Zhang, W. Wang, P. Alexandridis, C. Zhou and G. Wu, *J. Power Sources*, 2017, **354**, 134–147.
196 B. Derby, *Annu. Rev. Mater. Res.*, 2010, **40**, 395–414.
197 B. Derby, N. Reis, K. A. M. Seerden, P. S. Grant and J. R. G. Evans, *Materials Research Society Symposium - Proceedings*, 2000, vol. 625, pp. 195–201.
198 F. Torrisi, T. Hasan, W. Wu, Z. Sun, A. Lombardo, T. S. Kulmala, G. W. Hsieh, S. Jung, F. Bonaccorso, P. J. Paul, D. Chu and A. C. Ferrari, *ACS Nano*, 2012, **6**, 2992–3006.
199 G. Hu, L. Yang, Z. Yang, Y. Wang, X. Jin, J. Dai, Q. Wu, S. Liu, X. Zhu, X. Wang, T. C. Wu, R. C. T. Howe, T. Albrow-Owen, L. W. T. Ng, Q. Yang, L. G. Occhipinti, R. I. Woodward, E. J. R. Kelleher, Z. Sun, X. Huang, M. Zhang, C. D. Bain and T. Hasan, *Sci. Adv.*, 2020, **6**, eaba5029.
200 G. Hu, T. Albrow-Owen, X. Jin, A. Ali, Y. Hu, R. C. T. Howe, K. Shehzad, Z. Yang, X. Zhu, R. I. Woodward, T. C. Wu, H. Jussila, J. Bin Wu, P. Peng, P. H. Tan, Z. Sun, E. J. R. Kelleher, M. Zhang, Y. Xu and T. Hasan, *Nat. Commun.*, 2017, **8**, 278.
201 J. Dai, O. Ogbeide, N. Macadam, Q. Sun, W. Yu, Y. Li, B. L. Su, T. Hasan, X. Huang and W. Huang, *Chem. Soc. Rev.*, 2020, **49**, 1756–1789.
202 J. Rumble, *CRC handbook of chemistry and physics*, CRC Press, 100th edn, 2019.
203 S. Naficy, R. Jalili, S. H. Aboutalebi, R. A. Gorkin, K. Konstantinov, P. C. Innis, G. M. Spinks, P. Poulin and G. G. Wallace, *Mater. Horiz.*, 2014, **1**, 326–331.
204 L. W. T. Ng, X. Zhu, G. Hu, N. Macadam, D. Um, T. Wu, F. Le Moal, C. Jones and T. Hasan, *Adv. Funct. Mater.*, 2019, **29**, 1807933.
205 S. Saeed, R. M. Al-Sobaihi, M. F. Bertino, L. S. White and K. M. Saoud, *J. Mater. Chem. A*, 2015, **3**, 17606–17611.
206 I. Cooperstein, E. Shukrun, O. Press, A. Kamyshny and S. Magdassi, *ACS Appl. Mater. Interfaces*, 2018, **10**, 18879–18885.
207 H. Maleki, S. Montes, N. Hayati-Roodbari, F. Putz and N. Huesing, *ACS Appl. Mater. Interfaces*, 2018, **10**, 22718–22730.
208 K. M. Saoud, S. Saeed, M. F. Bertino and L. S. White, *J. Porous Mater.*, 2018, **25**, 511–520.
209 C. López-Iglesias, A. M. Casielles, A. Altay, R. Bettini, C. Alvarez-Lorenzo and C. A. García-González, *Chem. Eng. J.*, 2019, **357**, 559–566.
210 F. P. W. Melchels, J. Feijen and D. W. Grijpma, *Biomaterials*, 2010, **31**, 6121–6130.
211 J. Koo, J. W. Kim, M. Kim, S. Yoon and J. H. Shim, *Int. J. Precis. Eng. Manuf. - Green Technol.*, 2020, DOI: 10.1007/s40684-020-00189-4.
212 I. Põldsalu, M. Harjo, T. Tamm, M. Uibu, A. L. Peikolainen and R. Kiefer, *Sens. Actuators, B*, 2017, **250**, 44–51.
213 I. Põldsalu, U. Johanson, T. Tamm, A. Punning, F. Greco, A. L. Peikolainen, R. Kiefer and A. Aabloo, *Synth. Met.*, 2018, **246**, 122–127.
214 J. S. Gebauer, V. Mackert, S. Ognjanović and M. Winterer, *J. Colloid Interface Sci.*, 2018, **526**, 400–409.
215 F. Kotz, K. Arnold, W. Bauer, D. Schild, N. Keller, K. Sachsenheimer, T. M. Nargang, C. Richter, D. Helmer and B. E. Rapp, *Nature*, 2017, **544**, 337–339.
216 Y. Li, T. Gao, Z. Yang, C. Chen, W. Luo, J. Song, E. Hitz, C. Jia, Y. Zhou, B. Liu, B. Yang and L. Hu, *Adv. Mater.*, 2017, **29**, 1700981.
217 S. Liu, X. Shi, X. Li, Y. Sun, J. Zhu, Q. Pei, J. Liang and Y. Chen, *Nanoscale*, 2018, **10**, 20096–20107.
218 D. Cao, Y. Xing, K. Tantratian, X. Wang, Y. Ma, A. Mukhopadhyay, Z. Cheng, Q. Zhang, Y. Jiao, L. Chen and H. Zhu, *Adv. Mater.*, 2019, **31**, 1807313.
219 L. Li, Y. Zhu and J. Yang, *Mater. Lett.*, 2018, **210**, 136–138.
220 D. Kam, M. Chasnitsky, C. Nowogrodski, I. Braslavsky, T. Abitbol, S. Magdassi and O. Shoseyov, *Colloids Interfaces*, 2019, **3**, 46.
221 S. Sultan and A. P. Mathew, *Nanoscale*, 2018, **10**, 4421–4431.
222 J. Virtanen, M. Janka and S. Tuukkanen, *IFMBE Proc. 65*, 2017, **65**, 1029–1032.
223 Q. Cheng, Y. Liu, J. Lyu, Q. Lu, X. Zhang and W. Song, *J. Mater. Chem. A*, 2020, **8**, 14243–14253.
224 H. Zhu, W. Luo, P. N. Ciesielski, Z. Fang, J. Y. Zhu, G. Henriksson, M. E. Himmel and L. Hu, *Chem. Rev.*, 2016, **116**, 9305–9374.
225 E. Espinosa, D. Filgueira, A. Rodríguez and G. Chinga-Carrasco, *Bioengineering*, 2019, **6**, 65.
226 H. Françon, Z. Wang, A. Marais, K. Mystek, A. Piper, H. Granberg, A. Malti, P. Gatenholm, P. A. Larsson and L. Wågberg, *Adv. Funct. Mater.*, 2020, **30**, 1909383.
227 K. M. O. Håkansson, I. C. Henriksson, C. de la Peña Vázquez, V. Kuzmenko, K. Markstedt, P. Enoksson and P. Gatenholm, *Adv. Mater. Technol.*, 2016, **1**, 1600096.
228 C. Qian, L. Li, M. Gao, H. Yang, Z. Cai, B. Chen, Z. Xiang, Z. Zhang and Y. Song, *Nano Energy*, 2019, **63**, 103885.
229 A. J. Hess, A. J. Funk, Q. Liu, J. A. De La Cruz, G. H. Sheetah, B. Fleury and I. I. Smalyukh, *ACS Omega*, 2019, **4**, 20558–20563.
230 R. Ajdary, S. Huan, N. Zanjanizadeh Ezazi, W. Xiang, R. Grande, H. A. Santos and O. J. Rojas, *Biomacromolecules*, 2019, **20**, 2770–2778.
231 V. G. Rocha, E. García-Tuñón, C. Botas, F. Markoulidis, E. Feilden, E. D'Elia, N. Ni, M. Shaffer and E. Saiz, *ACS Appl. Mater. Interfaces*, 2017, **9**, 37136–37145.
232 K. Huang, J. Yang, S. Dong, Q. Feng, X. Zhang, Y. Ding and J. Hu, *Carbon*, 2018, **130**, 1–10.

233 S. Ling, W. Kang, S. Tao and C. Zhang, *Nano Mater. Sci.*, 2019, **1**, 142–148.
234 Z. Qi, J. Ye, W. Chen, J. Biener, E. B. Duoss, C. M. Spadaccini, M. A. Worsley and C. Zhu, *Adv. Mater. Technol.*, 2018, **3**, 1800053.
235 B. An, Y. Ma, W. Li, M. Su, F. Li and Y. Song, *Chem. Commun.*, 2016, **52**, 10948–10951.
236 F. Guo, X. Zheng, C. Liang, Y. Jiang, Z. Xu, Z. Jiao, Y. Liu, H. T. Wang, H. Sun, L. Ma, W. Gao, A. Greiner, S. Agarwal and C. Gao, *ACS Nano*, 2019, **13**, 5549–5558.
237 B. Yao, S. Chandrasekaran, H. Zhang, A. Ma, J. Kang, L. Zhang, X. Lu, F. Qian, C. Zhu, E. B. Duoss, C. M. Spadaccini, M. A. Worsley and Y. Li, *Adv. Mater.*, 2020, **32**, 1906652.
238 Y. Yu, Z. Wang, Z. Hou, W. Ta, W. Wang, X. Zhao, Q. Li, Y. Zhao, Q. Zhang and Z. Quan, *ACS Appl. Energy Mater.*, 2019, **2**, 3869–3877.
239 G. De La Osa, D. Pérez-Coll, P. Miranzo, M. I. Osendi and M. Belmonte, *Chem. Mater.*, 2016, **28**, 6321–6328.
240 G. Shi, S. E. Lowe, A. J. T. Teo, T. K. Dinh, S. H. Tan, J. Qin, Y. Zhang, Y. L. Zhong and H. Zhao, *Appl. Mater. Today*, 2019, **16**, 482–492.
241 C. Ma, R. Wang, H. Tetik, S. Gao, M. Wu, Z. Tang, D. Lin, D. Ding and W. Wu, *Nano Energy*, 2019, **66**, 104124.
242 E. Brown, P. Yan, H. Tekik, A. Elangovan, J. Wang, D. Lin and J. Li, *Mater. Des.*, 2019, **170**, 107689.
243 Q. Zhang, F. Zhang, X. Xu, C. Zhou and D. Lin, *ACS Nano*, 2018, **12**, 1096–1106.
244 R. M. Hensleigh, H. Cui, J. S. Oakdale, J. C. Ye, P. G. Campbell, E. B. Duoss, C. M. Spadaccini, X. Zheng and M. A. Worsley, *Mater. Horiz.*, 2018, **5**, 1035–1041.
245 Z. Wang, X. Liu, X. Shen, N. M. Han, Y. Wu, Q. Zheng, J. Jia, N. Wang and J. K. Kim, *Adv. Funct. Mater.*, 2018, **28**, 1707043.
246 Y. Chen, M. Guo, L. He, W. Yang, L. Xu, J. Meng, X. Tian, X. Ma, Q. Yu, K. Yang, X. Hong and L. Mai, *J. Mater.*, 2019, **5**, 303–312.
247 V. Middelkoop, T. Slater, M. Florea, F. Neaţu, S. Danaci, V. Onyenkeadi, K. Boonen, B. Saha, I. A. Baragau and S. Kellici, *J. Clean. Prod.*, 2019, **214**, 606–614.
248 Z. Wang, Q. Zhang, S. Long, Y. Luo, P. Yu, Z. Tan, J. Bai, B. Qu, Y. Yang, J. Shi, H. Zhou, Z. Y. Xiao, W. Hong and H. Bai, *ACS Appl. Mater. Interfaces*, 2018, **10**, 10437–10444.
249 X. Tang, C. Zhu, D. Cheng, H. Zhou, X. Liu, P. Xie, Q. Zhao, D. Zhang and T. Fan, *Adv. Funct. Mater.*, 2018, **28**, 1805057.
250 J. Wang, D. Liu, Q. Li, C. Chen, Z. Chen, P. Song, J. Hao, Y. Li, S. Fakhrhoseini, M. Naebe, X. Wang and W. Lei, *ACS Nano*, 2019, **13**, 7860–7870.
251 M. A. Worsley, S. J. Shin, M. D. Merrill, J. Lenhardt, A. J. Nelson, L. Y. Woo, A. E. Gash, T. F. Baumann and C. A. Orme, *ACS Nano*, 2015, **9**, 4698–4705.
252 H. Long, L. Chan, A. Harley-Trochimczyk, L. E. Luna, Z. Tang, T. Shi, A. Zettl, C. Carraro, M. A. Worsley and R. Maboudian, *Adv. Mater. Interfaces*, 2017, **4**, 1700217.
253 W. Yao, R. Mao, W. Gao, W. Chen, Z. Xu and C. Gao, *Carbon*, 2020, **158**, 418–425.
254 X. Feng, J. Zhao, D. Sun, L. Shanmugam, J. K. Kim and J. Yang, *J. Mater. Chem. A*, 2019, **7**, 4400–4407.
255 H. Bian, J. Wei, Y. Zhou, J. Liu, Z. Shao, B. Wang and Z. Li, *Propellants, Explos., Pyrotech.*, 2019, **44**, 1613–1620.
256 J. Ma, P. Wang, L. Dong, Y. Ruan and H. Lu, *J. Colloid Interface Sci.*, 2019, **534**, 12–19.
257 L. Dong, Z. Chen, X. Zhao, J. Ma, S. Lin, M. Li, Y. Bao, L. Chu, K. Leng, H. Lu and K. P. Loh, *Nat. Commun.*, 2018, **9**, 76.
258 F. Guo, Y. Jiang, Z. Xu, Y. Xiao, B. Fang, Y. Liu, W. Gao, P. Zhao, H. Wang and C. Gao, *Nat. Commun.*, 2018, **9**, 881.
259 L. Liu, Y. Huang, F. Li, Y. Ma, W. Li, M. Su, X. Qian, W. Ren, K. Tang and Y. Song, *Chem. Commun.*, 2018, **54**, 4810–4813.
260 J. Zhao, Y. Zhang, X. Zhao, R. Wang, J. Xie, C. Yang, J. Wang, Q. Zhang, L. Li, C. Lu and Y. Yao, *Adv. Funct. Mater.*, 2019, **29**, 1900809.
261 K. Fu, Y. Wang, C. Yan, Y. Yao, Y. Chen, J. Dai, S. Lacey, Y. Wang, J. Wan, T. Li, Z. Wang, Y. Xu and L. Hu, *Adv. Mater.*, 2016, **28**, 2587–2594.
262 T. Liu, C. Zhu, T. Kou, M. A. Worsley, F. Qian, C. Condes, E. B. Duoss, C. M. Spadaccini and Y. Li, *ChemNanoMat*, 2016, **2**, 635–641.
263 X. Yun, B. Lu, Z. Xiong, B. Jia, B. Tang, H. Mao, T. Zhang and X. Wang, *RSC Adv.*, 2019, **9**, 29384–29395.
264 J. Ding, K. Shen, Z. Du, B. Li and S. Yang, *ACS Appl. Mater. Interfaces*, 2017, **9**, 41871–41877.
265 F. Brunetti, A. Operamolla, S. Castro-Hermosa, G. Lucarelli, V. Manca, G. M. Farinola and T. M. Brown, *Adv. Funct. Mater.*, 2019, **29**, 1806798.
266 L. S. White, T. Selden, M. F. Bertino, C. Cartin, J. Angello, M. Schwan, B. Milow and L. Ratke, *Ind. Eng. Chem. Res.*, 2018, **57**, 1197–1206.
267 F. Bonaccorso, A. Lombardo, T. Hasan, Z. Sun, L. Colombo and A. C. Ferrari, *Mater. Today*, 2012, **15**, 564–589.
268 Y. Hernandez, V. Nicolosi, M. Lotya, F. M. Blighe, Z. Sun, S. De, I. T. McGovern, B. Holland, M. Byrne, Y. K. Gun'ko, J. J. Boland, P. Niraj, G. Duesberg, S. Krishnamurthy, R. Goodhue, J. Hutchison, V. Scardaci, A. C. Ferrari and J. N. Coleman, *Nat. Nanotechnol.*, 2008, **3**, 563–568.
269 J. N. Coleman, M. Lotya, A. O'Neill, S. D. Bergin, P. J. King, U. Khan, K. Young, A. Gaucher, S. De, R. J. Smith, I. V. Shvets, S. K. Arora, G. Stanton, H. Y. Kim, K. Lee, G. T. Kim, G. S. Duesberg, T. Hallam, J. J. Boland, J. J. Wang, J. F. Donegan, J. C. Grunlan, G. Moriarty, A. Shmeliov, R. J. Nicholls, J. M. Perkins, E. M. Grieveson, K. Theuwissen, D. W. McComb, P. D. Nellist and V. Nicolosi, *Science*, 2011, **331**, 568–571.
270 P. Wei, H. Leng, Q. Chen, R. C. Advincula and E. B. Pentzer, *ACS Appl. Polym. Mater.*, 2019, **1**, 885–892.
271 J. L. Gurav, I. K. Jung, H. H. Park, E. S. Kang and D. Y. Nadargi, *J. Nanomater.*, 2010, 409310.
272 N. Hüsing and U. Schubert, *Angew. Chem., Int. Ed.*, 1998, **37**, 22–45.
273 W. Liao, H. B. Zhao, Z. Liu, S. Xu and Y. Z. Wang, *Composites, Part B*, 2019, **173**, 107036.

274 L. Ren, S. Cui, F. Cao and Q. Guo, *Angew. Chem., Int. Ed.*, 2014, **53**, 10147–10149.
275 J. J. Moyano, A. Gómez-Gómez, D. Pérez-Coll, M. Belmonte, P. Miranzo and M. I. Osendi, *Carbon*, 2019, **151**, 94–102.
276 C. L. Yaws, H.-C. Yang and X. Pan, *Chem. Eng.*, 1991, **98**, 140–149.
277 G. Körösi and E. S. Kováts, *J. Chem. Eng. Data*, 1981, **26**, 323–332.
278 G. W. Kauffman and P. C. Jurs, *J. Chem. Inf. Comput. Sci.*, 2001, **41**, 408–418.
279 D. R. Lide, *CRC Handbook of Chemistry and Physics*, 85th Edn, CRC Press, 2004.
280 R. Sui and P. Charpentier, *Chem. Rev.*, 2012, **112**, 3057–3082.
281 D. W. Matson and R. D. Smith, *J. Am. Ceram. Soc.*, 1989, **72**, 871–881.
282 A. H. N. Mousa, *J. Chem. Thermodyn.*, 1977, **9**, 1063–1065.
283 L. M. Radzhabova, G. V. Stepanov and I. M. Abdulagatov, *Fluid Phase Equilib.*, 2011, **309**, 128–144.
284 Y. Jiang, J. Feng and J. Feng, *J. Sol-Gel Sci. Technol.*, 2017, **83**, 64–71.
285 D. B. Mahadik, Y. K. Lee, C. S. Park, H. Y. Chung, M. H. Hong, H. N. R. Jung, W. Han and H. H. Park, *Solid State Sci.*, 2015, **50**, 1–8.
286 C. K. Chua and M. Pumera, *Chem. Soc. Rev.*, 2014, **43**, 291–312.
287 P. C. Thapliyal and K. Singh, *J. Mater.*, 2014, 127049.
288 X. Wei, S. Wan and S. Gao, *Nano Energy*, 2016, **28**, 206–215.
289 X. Zheng, G. Shen, C. Wang, Y. Li, D. Dunphy, T. Hasan, C. J. Brinker and B. L. Su, *Nat. Commun.*, 2017, **8**, 14921.
290 L. Wu, Y. Li, Z. Fu and B.-L. Su, *Natl. Sci. Rev.*, 2020, **7**, 1667–1701.
291 L. Fan, Y. Zhang, Z. Guo, B. Sun, D. Tian, Y. Feng, N. Zhang and K. Sun, *Chem. – Eur. J.*, 2020, **26**, 9314–9318.
292 Q. Zheng, A. Kvit, Z. Cai, Z. Ma and S. Gong, *J. Mater. Chem. A*, 2017, **5**, 12528–12541.
293 D. Ghosh, J. Lim, R. Narayan and S. O. Kim, *ACS Appl. Mater. Interfaces*, 2016, **8**, 22253–22260.
294 C. Wan, Y. Jiao, W. Bao, H. Gao, Y. Wu and J. Li, *J. Mater. Chem. A*, 2019, **7**, 9556–9564.
295 Z. Pan, M. Liu, J. Yang, Y. Qiu, W. Li, Y. Xu, X. Zhang and Y. Zhang, *Adv. Funct. Mater.*, 2017, **27**, 1701122.
296 W. Sun, G. Gao, Y. Du, K. Zhang and G. Wu, *J. Mater. Chem. A*, 2018, **6**, 9938–9947.
297 H. Zhang, A. Xie, C. Wang, H. Wang, Y. Shen and X. Tian, *ChemPhysChem*, 2014, **15**, 366–373.
298 Y. Xu, Z. Lin, X. Huang, Y. Liu, Y. Huang and X. Duan, *ACS Nano*, 2013, **7**, 4042–4049.
299 L. Liu, Y. Yan, Z. Cai, S. Lin and X. Hu, *Adv. Mater. Interfaces*, 2018, **5**, 1701548.
300 D. Lin, Y. Liu and Y. Cui, *Nat. Nanotechnol.*, 2017, **12**, 194–206.
301 D. Tie, S. Huang, J. Wang, J. Ma, J. Zhang and Y. Zhao, *Energy Storage Mater.*, 2019, **21**, 22–40.
302 P. Simon, Y. Gogotsi and B. Dunn, *Science*, 2014, **343**, 1210–1211.
303 G. Nagaraju, S. Chandra Sekhar, L. Krishna Bharat and J. S. Yu, *ACS Nano*, 2017, **11**, 10860–10874.
304 R. Liu, L. Ma, G. Niu, X. Li, E. Li, Y. Bai and G. Yuan, *Adv. Funct. Mater.*, 2017, **27**, 1701635.
305 Y. Zhao, H. Ma, S. Huang, X. Zhang, M. Xia, Y. Tang and Z. F. Ma, *ACS Appl. Mater. Interfaces*, 2016, **8**, 22997–23066.
306 Z. Gao, C. Chen, J. Chang, L. Chen, P. Wang, D. Wu, F. Xu and K. Jiang, *Chem. Eng. J.*, 2018, **343**, 572–582.
307 Y. Chen, B. Xu, J. Wen, J. Gong, T. Hua, C.-W. Kan and J. Deng, *Small*, 2018, **14**, 1704373.
308 N. Chen, C. Han, R. Shi, L. Xu, H. Li, Y. Liu, J. Li and B. Li, *Electrochim. Acta*, 2018, **283**, 36–44.
309 H. Sun, L. Mei, J. Liang, Z. Zhao, C. Lee, H. Fei, M. Ding, J. Lau, M. Li, C. Wang, X. Xu, G. Hao, B. Papandrea, I. Shakir, B. Dunn, Y. Huang and X. Duan, *Science*, 2017, **356**, 599–604.
310 S. Choi, S. I. Han, D. Kim, T. Hyeon and D. H. Kim, *Chem. Soc. Rev.*, 2019, **48**, 1566–1595.
311 J. Huang, J. Zeng, B. Liang, J. Wu, T. Li, Q. Li, F. Feng, Q. Feng, M. J. Rood and Z. Yan, *ACS Appl. Mater. Interfaces*, 2020, **12**, 16822–16830.
312 C. Yang, W. Liu, N. Liu, J. Su, L. Li, L. Xiong, F. Long, Z. Zou and Y. Gao, *ACS Appl. Mater. Interfaces*, 2019, **11**, 33165–33172.
313 X. Hou, R. Zhang and D. Fang, *Ceram. Int.*, 2020, **46**, 2122–2127.
314 T. R. Ray, J. Choi, A. J. Bandodkar, S. Krishnan, P. Gutruf, L. Tian, R. Ghaffari and J. A. Rogers, *Chem. Rev.*, 2019, **119**, 5461–5533.
315 K. Kruusamäe, A. Punning, A. Aabloo and K. Asaka, *Actuators*, 2015, **4**, 17–38.
316 D. Chen and Q. Pei, *Chem. Rev.*, 2017, **117**, 11239–11268.
317 Q. Zheng, B. Shi, Z. Li and Z. L. Wang, *Adv. Sci.*, 2017, **4**, 1700029.
318 F. Yi, H. Ren, J. Shan, X. Sun, D. Wei and Z. Liu, *Chem. Soc. Rev.*, 2018, **47**, 3152–3188.
319 J. Nie, X. Chen and Z. L. Wang, *Adv. Funct. Mater.*, 2019, **29**, 1806351.
320 Z. Meng, R. M. Stolz, L. Mendecki and K. A. Mirica, *Chem. Rev.*, 2019, **119**, 478–598.
321 T.-C. Wu, J. Dai, G. Hu, W.-B. Yu, O. Ogbeide, A. De Luca, X. Huang, B.-L. Su, Y. Li, F. Udrea and T. Hasan, *Sens. Actuators, B*, 2020, **321**, 128446.
322 T. C. Wu, A. De Luca, Q. Zhong, X. Zhu, O. Ogbeide, D. S. Um, G. Hu, T. Albrow-Owen, F. Udrea and T. Hasan, *npj 2D Mater. Appl.*, 2019, **3**, 42.
323 G. Gan, X. Li, S. Fan, L. Wang, M. Qin, Z. Yin and G. Chen, *Eur. J. Inorg. Chem.*, 2019, 3126–3141.
324 J. E. Amonette and J. Matyáš, *Microporous Mesoporous Mater.*, 2017, **250**, 100–119.
325 C. Parra-Cabrera, C. Achille, S. Kuhn and R. Ameloot, *Chem. Soc. Rev.*, 2018, **47**, 209–230.
326 W. J. Yang, A. C. Y. Yuen, A. Li, B. Lin, T. B. Y. Chen, W. Yang, H. D. Lu and G. H. Yeoh, *Cellulose*, 2019, **26**, 6449–6476.
327 J. Ge, H. Y. Zhao, H. W. Zhu, J. Huang, L. A. Shi and S. H. Yu, *Adv. Mater.*, 2016, **28**, 10459–10490.

328 Y. Yang, X. Li, X. Zheng, Z. Chen, Q. Zhou and Y. Chen, *Adv. Mater.*, 2018, **30**, 1704912.
329 C. A. García-González, T. Budtova, L. Durães, C. Erkey, P. Del Gaudio, P. Gurikov, M. Koebel, F. Liebner, M. Neagu and I. Smirnova, *Molecules*, 2019, **24**, 1815.
330 J. Ge, M. Li, Q. Zhang, C. Z. Yang, P. H. Wooley, X. Chen and S. Y. Yang, *Int. J. Polym. Sci.*, 2013, 402859.
331 S. Asha, A. N. Ananth, S. P. Jose and M. A. J. Rajan, *Appl. Nanosci.*, 2018, **8**, 395–405.
332 A. Muñoz-Ruíz, D. M. Escobar-García, M. Quintana, A. Pozos-Guillén and H. Flores, *J. Nanomater.*, 2019, 2875375.
333 R. Ghafari, M. Jonoobi, L. M. Amirabad, K. Oksman and A. R. Taheri, *Int. J. Biol. Macromol.*, 2019, **136**, 796–803.
334 S. Dong, Y. N. Zhang, J. Wan, R. Cui, X. Yu, G. Zhao and K. Lin, *J. Mater. Chem. B*, 2020, **8**, 368–379.
335 M. Mohammadian, T. S. Jafarzadeh Kashi, M. Erfan and F. P. Soorbaghi, *J. Drug Delivery Sci. Technol.*, 2018, **44**, 205–212.
336 K. C. W. Wu, Y. Yamauchi, C. Y. Hong, Y. H. Yang, Y. H. Liang, T. Funatsu and M. Tsunoda, *Chem. Commun.*, 2011, **47**, 5232–5234.
337 S. Wei, Y. C. Ching and C. H. Chuah, *Carbohydr. Polym.*, 2020, **231**, 115744.
338 A. Veronovski, G. Tkalec, Z. Knez and Z. Novak, *Carbohydr. Polym.*, 2014, **113**, 272–278.
339 D. A. S. Agostinho, A. I. Paninho, T. Cordeiro, A. V. M. Nunes, I. M. Fonseca, C. Pereira, A. Matias and M. G. Ventura, *Mater. Chem. Phys.*, 2020, **253**, 123290.
340 T. Athamneh, A. Amin, E. Benke, R. Ambrus, C. S. Leopold, P. Gurikov and I. Smirnova, *J. Supercrit. Fluids*, 2019, **150**, 49–55.
341 I. De Marco, R. Iannone, S. Miranda and S. Riemma, *Int. J. Life Cycle Assess.*, 2018, **23**, 1228–1239.
342 X. Chen, X. Xu, W. Li, B. Sun, J. Yan, C. Chen, J. Liu, J. Qian and D. Sun, *ACS Appl. Bio Mater.*, 2018, **1**, 42–50.
343 Z. Ulker and C. Erkey, *J. Controlled Release*, 2014, **177**, 51–63.
344 C. A. García-González, M. Alnaief and I. Smirnova, *Carbohydr. Polym.*, 2011, **86**, 1425–1438.
345 T. Silvetti, L. Merlini, M. Brasca and Y. M. Galante, *Appl. Microbiol. Biotechnol.*, 2018, **102**, 2683–2692.
346 W. Mueannoom, A. Srisongphan, K. M. G. Taylor, S. Hauschild and S. Gaisford, *Eur. J. Pharm. Biopharm.*, 2012, **80**, 149–155.
347 G. Sharma, W. Mueannoom, A. B. M. Buanz, K. M. G. Taylor and S. Gaisford, *Int. J. Pharm.*, 2013, **447**, 165–170.
348 C. S. Ponseca, P. Chábera, J. Uhlig, P. Persson and V. Sundström, *Chem. Rev.*, 2017, **117**, 10940–11024.
349 J. Deng, Y. Su, D. Liu, P. Yang, B. Liu and C. Liu, *Chem. Rev.*, 2019, **119**, 9221–9259.
350 C. S. Hu, H. J. Li, J. Y. Wang, A. Haleem, X. C. Li, M. Siddiq and W. D. He, *ACS Appl. Energy Mater.*, 2019, **2**, 7554–7563.
351 P. Mu, Z. Zhang, W. Bai, J. He, H. Sun, Z. Zhu, W. Liang and A. Li, *Adv. Energy Mater.*, 2019, **9**, 1802158.
352 P. Mu, W. Bai, Z. Zhang, J. He, H. Sun, Z. Zhu, W. Liang and A. Li, *J. Mater. Chem. A*, 2018, **6**, 18183–18190.
353 Y. Fu, G. Wang, T. Mei, J. Li, J. Wang and X. Wang, *ACS Sustainable Chem. Eng.*, 2017, **5**, 4665–4671.
354 L. Tang, C. Jia, Y. Xue, L. Li, A. Wang, G. Xu, N. Liu and M. Wu, *Appl. Catal., B*, 2017, **219**, 241–248.
355 Y. Hou, Z. Wen, S. Cui, X. Feng and J. Chen, *Nano Lett.*, 2016, **16**, 2268–2277.
356 X. D. Gao, X. M. Li, X. Y. Gan, Y. Q. Wu, R. K. Zheng, C. L. Wang, Z. Y. Gu and P. He, *J. Mater. Chem.*, 2012, **22**, 18930–18938.
357 L. Zhao, B. Bhatia, S. Yang, E. Strobach, L. A. Weinstein, T. A. Cooper, G. Chen and E. N. Wang, *ACS Nano*, 2019, **13**, 7508–7516.
358 P. Tao, G. Ni, C. Song, W. Shang, J. Wu, J. Zhu, G. Chen and T. Deng, *Nat. Energy*, 2018, **3**, 1031–1041.
359 L.-H. Chen, M.-H. Sun, Z. Wang, W. Yang, Z. Xie and B.-L. Su, *Chem. Rev.*, 2020, **120**, 11194–11294.
360 J. F. Xing, M. L. Zheng and X. M. Duan, *Chem. Soc. Rev.*, 2015, **44**, 5031–5039.
361 T. A. Schaedler, A. J. Jacobsen, A. Torrents, A. E. Sorensen, J. Lian, J. R. Greer, L. Valdevit, W. B. Carter, Q. Ge, J. A. Jackson, S. O. Kucheyev, N. X. Fang and C. M. Spadaccini, *Science*, 2011, **334**, 1373–1377.
362 M. A. Skylar-Scott, J. Mueller, C. W. Visser and J. A. Lewis, *Nature*, 2019, **575**, 330–335.

